AD-A011 773

STUDIES OF ATMOSPHERIC PROCESSES

Edward R. Fisher, et al

Wayne State University

Prepared for:

Air Force Cambridge Research Laboratories
Advanced Research Projects Agency

November 1974

DISTRIBUTED BY:

NTIS

National Technical Information Service
U. S. DEPARTMENT OF COMMERCE

196058

AFCRL-TR-74-0584

ADA011773

STUDIES OF ATMOSPHERIC PROCESSES

Edward R. Fisher
Paul B. Foreman
Barbara B. Krieger
Ralph H. Kummler
A. Bryan Lees
Richard Mariott
Pieter K. Rol
Geoffrey Smith

Research Institute for Engineering Sciences
Wayne State University
Detroit, Michigan 48202

November 1974
Final Report for Period 12 July, 1971 - 30 June, 1974

Approved for public release; distribution unlimited.

Sponsored by:

Defense Advanced Research Projects Agency
ARPA Order No. 1856

Monitored by:

AIR FORCE CAMBRIDGE RESEARCH LABORATORIES
AIR FORCE SYSTEMS COMMAND
UNITED STATES AIR FORCE
HANSCOM AFB, MASSACHUSETTS 01731

DDC
RECEIVED
JUN 23 1975
A

Reproduced by
NATIONAL TECHNICAL
INFORMATION SERVICE
US Department of Commerce
Springfield, VA. 22151

Unclassified

SECURITY CLASSIFICATION OF THIS PAGE (When Data Entered)

REPORT DOCUMENTATION PAGE		READ INSTRUCTIONS BEFORE COMPLETING FORM
1. REPORT NUMBER AFCRL-TR-74-0584	2. GOVT ACCESSION NO.	3. RECIPIENT'S CATALOG NUMBER AD-A011 773
4. TITLE (and Subtitle) STUDIES OF ATMOSPHERIC PROCESSES		5. TYPE OF REPORT & PERIOD COVERED Scientific - Final Report 7-12-71 - 6-30-74
		6. PERFORMING ORG. REPORT NUMBER RIES - 74
7. AUTHOR(s) E.R.Fisher, B.Foreman, B.Krieger, R.H.Kummler, A.B.Lees, P.K.Rol, G.Smith		8. CONTRACT OR GRANT NUMBER(s) F-19628-72-C-0007
9. PERFORMING ORGANIZATION NAME AND ADDRESS Research Institute for Engineering Sciences College of Engineering WSU, Detroit, Mich. 48202		10. PROGRAM ELEMENT, PROJECT, TASK AREA & WORK UNIT NUMBERS 1856-N/A - N/A
11. CONTROLLING OFFICE NAME AND ADDRESS Air Force Cambridge Research Laboratories Hanscom AFB, Massachusetts 01731 Contract Monitor: Alva T. Stair, Jr./OPR-1		12. REPORT DATE November 1974 13. NUMBER OF PAGES 144
14. MONITORING AGENCY NAME & ADDRESS(if different from Controlling Office)		15. SECURITY CLASS. (of this report) Unclassified 15a. DECLASSIFICATION/DOWNGRADING SCHEDULE

16. DISTRIBUTION STATEMENT (of this Report)

Approved for Public Release; distribution unlimited.

17. DISTRIBUTION STATEMENT (of the abstract entered in Block 20, if different from Report)

18. SUPPLEMENTARY NOTES

This research was sponsored by Defense Advanced Research Projects Agency.
ARPA Order No. 1856

19. KEY WORDS (Continue on reverse side if necessary and identify by block number)

Plume Chemistry
Chemiluminescent Reactions
Relaxation in Combustion Products
Beam Measurements of O Atom Scattering

20. ABSTRACT (Continue on reverse side if necessary and identify by block number)

This report summarizes experimental and analytical studies on chemistry and energy transfer processes important to rocket exhaust components in the upper atmosphere. The report is divided into four parts. The first part covers the experimental studies on chemiluminescence observed in the infrared from reactions in the H-C-N system. The second part presents a compilation of artificial infrared spectra generated to aid in

PRICES SUBJECT TO CHANGE

the experimental interpretation of Part I. Part II presents the results of detailed relaxation calculations in an expanding flow of combustion affluents. This calculation, simulating a core flow field, shows substantial vibrational freezing particularly in the diatomic species present. The last part presents detailed measurement of the scattering of O atoms from various plume related species. The intermolecular potential for these systems is also determined.

AFCRL-TR-74-0584

STUDIES OF ATMOSPHERIC PROCESSES

Edward R. Fisher
Paul B. Foreman
Barbara B. Krieger
Ralph H. Kummler
A. Bryan Lees
Richard Mariott
Pieter K. Rol
Geoffrey Smith

Research Institute for Engineering Sciences
Wayne State University
Detroit, Michigan 48202

November 1974

Final Report for Period 12 July, 1971 - 30 June, 1974

Approved for public release; distribution unlimited.

Sponsored by:

Defense Advanced Research Projects Agency
ARPA Order No. 1856

Monitored by:

AIR FORCE CAMBRIDGE RESEARCH LABORATORIES
AIR FORCE SYSTEMS COMMAND
UNITED STATES AIR FORCE
HANSCOM AFB, MASSACHUSETTS 01731

Qualified requestors may obtain additional copies from the Defense Documentation Center. All others should apply to the National Technical Information Service.

TABLE OF CONTENTS

PART I: Experimental Observations of Chemiluminesence from H-N-C Systems

R.H.Kummler, E.R.Fisher, G.Smith, B.Krieger

TABLE OF CONTENTS

INTRODUCTION

As previously discussed by Kummler, Fisher, and Boynton (1973), hydrazine and substituted amines form an important class of fuels. When the products of these fuels interact with a low pressure environment containing oxygen atoms, measurable radiation from the ultraviolet through the infrared spectral regions occurs. This radiation occurs both indirectly by energy transfer to infrared active products of the substituted amine combustion (CO_2, H_2O, CO, etc.) and directly by strongly exothermic chemiluminescent reactions initiated by O atom attack. Most of the energy released by such reactions is expected to form vibrationally excited reaction products and is therefore observable as infrared radiation. Minor radiation in terms of available energy, but not in terms of observable signals, is expected to be observable in the visible and vacuum ultraviolet spectral regions. Either wavelength region provides qualitative diagnostic information regarding the mechanism of reaction, but the value of the diagnostic depends upon our quantitative knowledge and understanding of the radiation mechanism.

Predictions of the radiation associated with chemiluminescent processes requires knowledge of the concentration of reactive species, rate constants for the important reactions, and the fraction of the energy liberated by the reaction which ends up in a given internal mode. Although little is known directly

about unreacted fuel concentrations in environments of interest, there is some evidence that levels of a few percent may exist in an excess of atomic oxygen.

This report summarizes the experiments conducted in the Environmental Kinetics Laboratory of Wayne State University which demonstrate the chemiluminescent processes occurring in these systems. The systems studied include:

$$O + N_2H_4 \rightarrow H_2O + HNNH$$

$$O + NH_3 \rightarrow NH_2 + OH$$

$$O + NR_3 \text{ (where R is a hydrocarbon radical)} \rightarrow \text{products}$$

$$H + NO_2 \rightarrow NO + OH \quad .$$

As illustrated in Figure 1 (Kummler, et al, 1973) all of these reactions should be prominent in the lean fuel-oxygen atom systems. As indicated in Table I, a preliminary model has been formed and has been tested in simplified form (Kummler, et al, 1973) with reasonable assumptions regarding the energy distributions. In this work we attempt to support those assumptions by experimental work on individual systems in the context of Figure 1 and Table I.

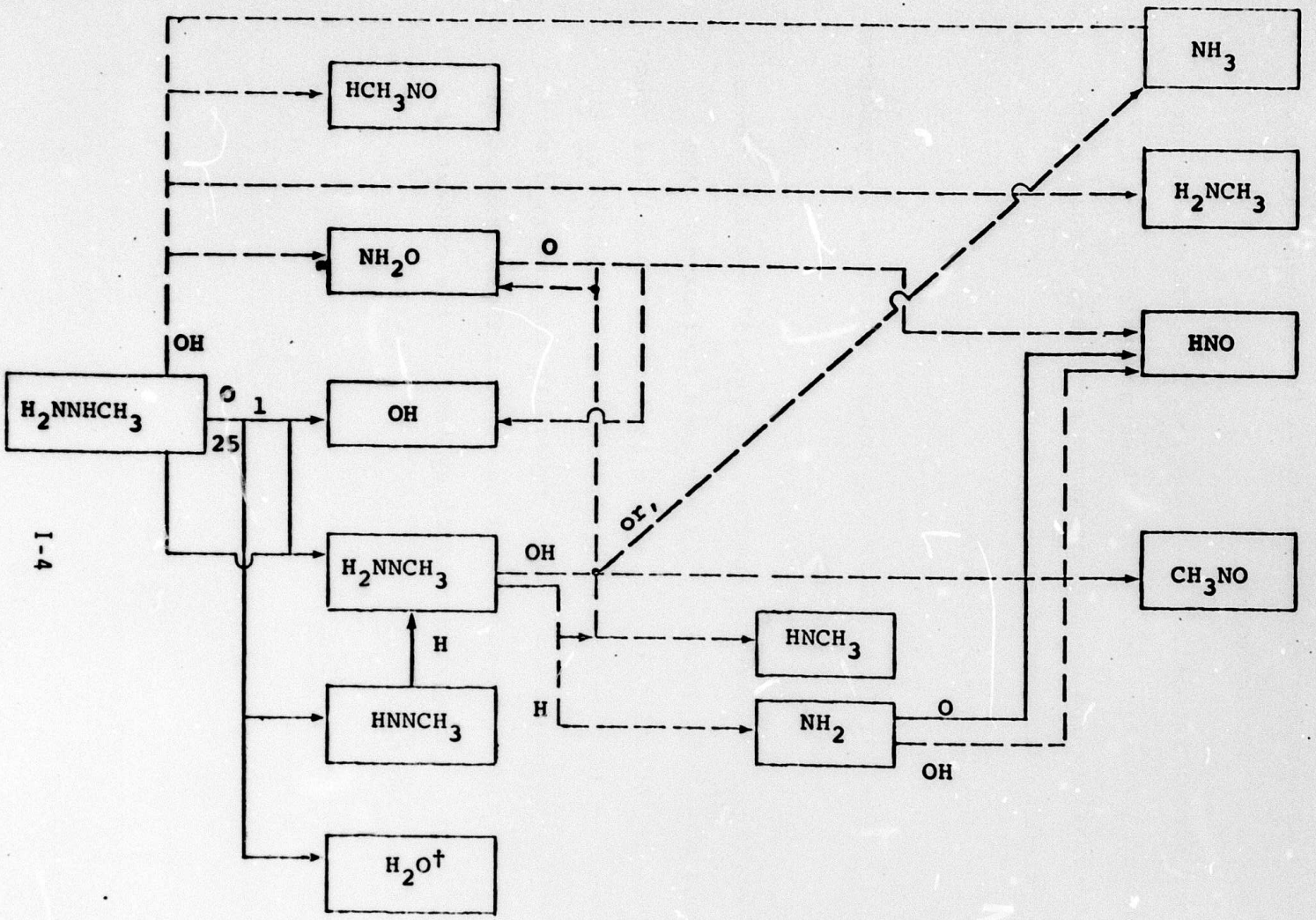

FIGURE 1. Simplified O atom oxidation mechanism for MMH (UDMH and N_2H_4 are similar) illustrating the stable species which can form in this system as intermediates. The dotted lines represent reactions which are probable, but which have not yet been experimentally observed.

TABLE I

RECOMMENDED RATE CONSTANTS FOR

$O + H_2NNR'R''$ SYSTEM

Reaction	Rate Constant, cc/sec	ΔH^R_{298}	Reference
$O + H_2NN(CH_3)_2 \rightarrow HN_2(CH_3)_2 + OH$	1×10^{-12}		Analogy with N_2H_4
$O + H_2NNHCH_3 \rightarrow HNNCH_3 + H_2O$	2×10^{-11}	-102.5	Foner and Hudson (1970) and analogy with N_2H_4
$O + N_2H_4 \rightarrow N_2H_2 + H_2O$	1.8×10^{-11}	-90	Gehring, et al (1969)
$OH + N_2H_4 \rightarrow NH_3 + NH_2O$	2×10^{-11}		Estimate. Product identification by Gehring, et al (1970).
$H + N_2H_4 \rightarrow N_2H_3 + H_2$	$2.2 \times 10^{-11}\ e^{-1260/T}$		Gehring, et al (1971)
$H + N_2H_3 \rightarrow 2NH_2$	2.7×10^{-12}		Gehring, et al (1971)
$H + N_2H_2 \rightarrow N_2H_3$	10^{-10}		Estimated [Bahn (1968)].
$O + NH_3 \rightarrow NH_2 + OH$	$2.5 \times 10^{-12}\ e^{-3000/T}$	2.7	Albers, et al (1969)
$OH + NH_3 \rightarrow NH_2 + H_2O$	$6.6 \times 10^{-14}\ T^{0.68}\ e^{-560/T}$	-14	Kondratiev (1972)
$O + NH_2 \rightarrow HNO + H$	10^{-11}	-15.7	Albers, et al (1969)
$OH + HNO \rightarrow H_2O + NO$	3×10^{-11}	-69.3	Sawyer and Glassman (1967)

EXPERIMENTAL APPARATUS AND PROCEDURES

The experimental system, illustrated in Figure 2, has been described previously in related publications (Krieger, Malki and Kummler, 1972; and Kummler, et al, 1973). All experiments were performed on that discharge flow tube system. Flow rates up to 80 m/sec could be obtained. Detection systems include a quarter meter Jarrell Ash (M) monochrometer with gratings blazed at 3000 A, 6000 A, 2.1μ, and 5μ. An RCA C31025C photomultiplier was used to view spectra from 2000 A to 9000 A, a Santa Barbara ITO Pbs detector from 1 - 3μ, a LN_2 Au-Ge detector from 3 - 6μ, and a Santa Barbara Au-Ge liquid He cooled detector was used from 6 - 25μ (P). A Raytheon PGM 10 x 2 pulsed diathermy unit provided a pulsed discharge at 30 - 10000 Hz for infrared detection with a PAR HR-8 phase sensitive lock in amplifier. Visible detection employed a Keithley 602 electrometer (E). Honeywell Electronic 194 dual channel recorders (R) were used. Pressure in the reactor was monitored using an MKS baratron 77H capacitance manometer with a 10 torr head. O_2, H_2, or N_2 were discharged using the 2450 MHz diathermy and either Evensen or Broida cavities. An Extranuclear 3/4" quadruple mass spectrometer was available to the system. A Brad Thompson 774 electron beam welder was used for electron excitation studies. Oxygen atoms were monitored by NO_2 titration. Absolute actinometry was obtained from 4000 A to 3μ using the NO + O glow. Gas flows were

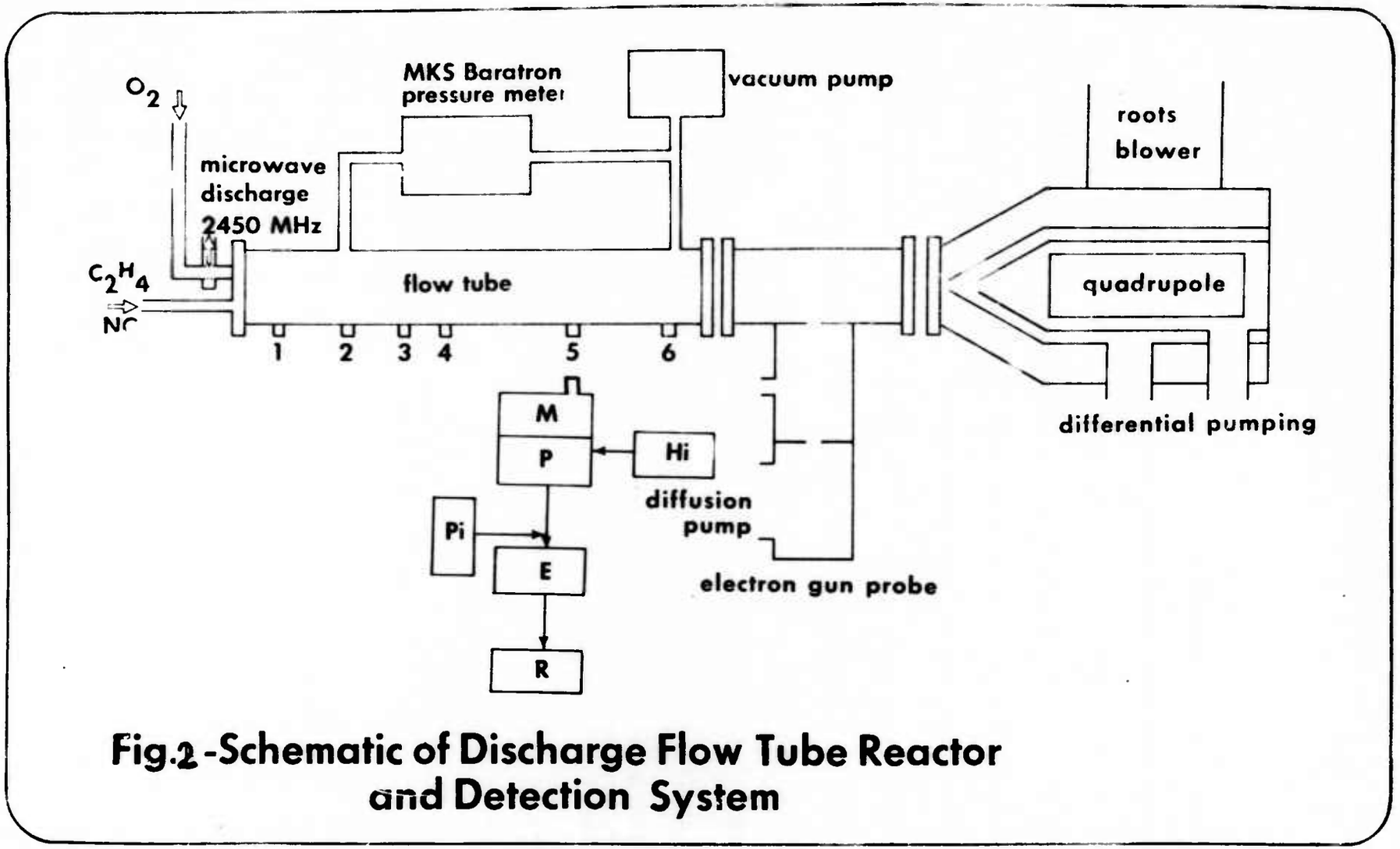

Fig.2 -Schematic of Discharge Flow Tube Reactor and Detection System

monitored by rotometers and calibrated capillaries using a Baratron pressure transducer to monitor the upstream pressure. H atoms were monitored using the H + NO glow compared to the O + NO glow. The stable gas concentration was monitored by observing the partial pressure of the gas in the absence of oxygen atoms (or any reactive gas).

The radiation observed is analyzed in several ways. First, a synthetic spectrum is prepared by a computer model for comparison with experimental spectra (see Part II). Second, a computer model of the reaction kinetics (e.g., Krieger and Kummler, 1973) is used to analyze the dominant processes in the contact time and concentration regimes of experimental interest. Third, the computer model is employed to predict regimes in which elementary reactions can be isolated and studied in isolation or in small groups.

RESULTS: SPECIFIC SYSTEMS

A. $H + NO_2$

The reaction $H + NO_2 \rightarrow OH^{\ddagger} + NO$ was chosen as a prototype reaction to study because it is the classic OH generation mechanism for flow tube work and therefore must be quantified before other OH reactions can be studied. It was previously (Kummler, 1969) shown that $OH^{\ddagger}$ is the likely product of that reaction on the basis of kinetics. However, the quantum yield of $OH^{\ddagger}$ as determined from absorption measurements by Del Greco and Kaufman (1962) was found to be low. The study conducted in this report was aimed at re-examining the quantum yield via infrared emission studies.

The procedure followed in this experiment consisted of calibrating an ambient PbS detector, chopper, filter and PAR/HR8 lock-in amplification system using the infrared data of Stair and Kennealy (1967), Kaufman (1974), and Vanpee (1971), for the photon yield of the reaction

$$NO + O \rightarrow NO_2 + h\nu \quad .$$

This reaction provides an actinometric standard at 2.7μ for our system once the NO concentration is measured via an MKS Baratron and the O atom concentration is found by NO_2 titration. The H atom concentration is estimated using the reaction of

$$H + NO \rightarrow HNO^{*} \rightarrow HNO + h\nu \quad .$$

The observed spectrum from H + NO is illustrated in Figure 3 for the visible region of the spectrum.

The low resolution infrared region of the spectrum for $H + NO_2$ is illustrated in Figure 4 and has been discussed in previous work by Kummler, et al, (1973). In this latter work, a flow velocity of 80 m/sec is employed in order to minimize the contact time (about 1 m sec) following the introduction of NO_2 to the discharged H_2 stream. Since the rate constant for $H + NO_2$ at room temperature is 4.9×10^{-11} cc/sec, and the rate constant for $OH + OH \rightarrow H_2O + O$ is 2.5×10^{-12} cc/sec, we have suggested that the emission at this short contact time with low NO_2 concentrations (4 - 5μ) is primarily $OH^{\ddagger}$. Thus, in Figure 4 we see the 0-1 and 1-2 transitions near 2.7μ and the 0-2 transition near 1.5μ. These are the only transitions possible because of the energetics of the $H + NO_2$ reaction ($\Delta H_{298} = -28.43$ kcal, $\Delta v \leq 2$ for OH). Using the NO + O glow to calibrate the relative intensities of the 1.5 to 2.7μ radiation, we obtain an intensity ratio of 0.445 compared to 0.44±0.03 obtained by Murphy (1971). Without knowledge of the detailed $OH^{\ddagger}$ destruction reaction rates in this reaction system, we cannot precisely determine the quantum yield of $OH^{\ddagger}$, but based on ground state chemistry we have concluded that Kaufman's estimate appears reasonable, i.e. the quantum yield is much less than 0.10. The purpose of this work is to re-examine this question using higher resolution spectroscopy and a detailed examination of the system kinetics.

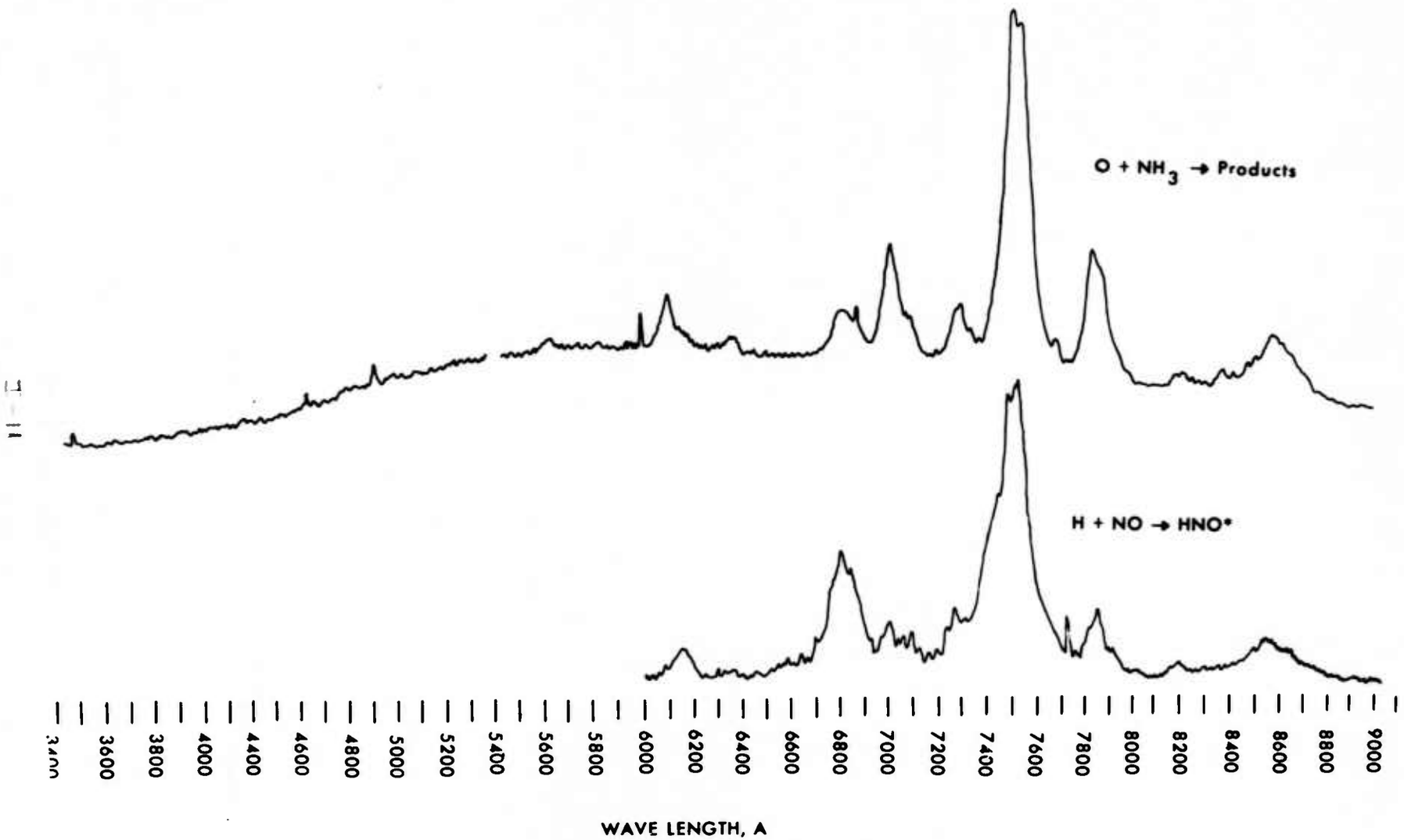

Figure 3: Near Infrared Spectrum of H + NO compared to the O + NH_3 Infrared Emission Spectrum. O + NH_3: 530 μ O_2, 7.5 μ O 15 μ NH_3, 500 μ slits, 2 msec to first window; H + NO: 750 μ Ar, 150 μ H_2, 70 μ NO, 500 μ slits.

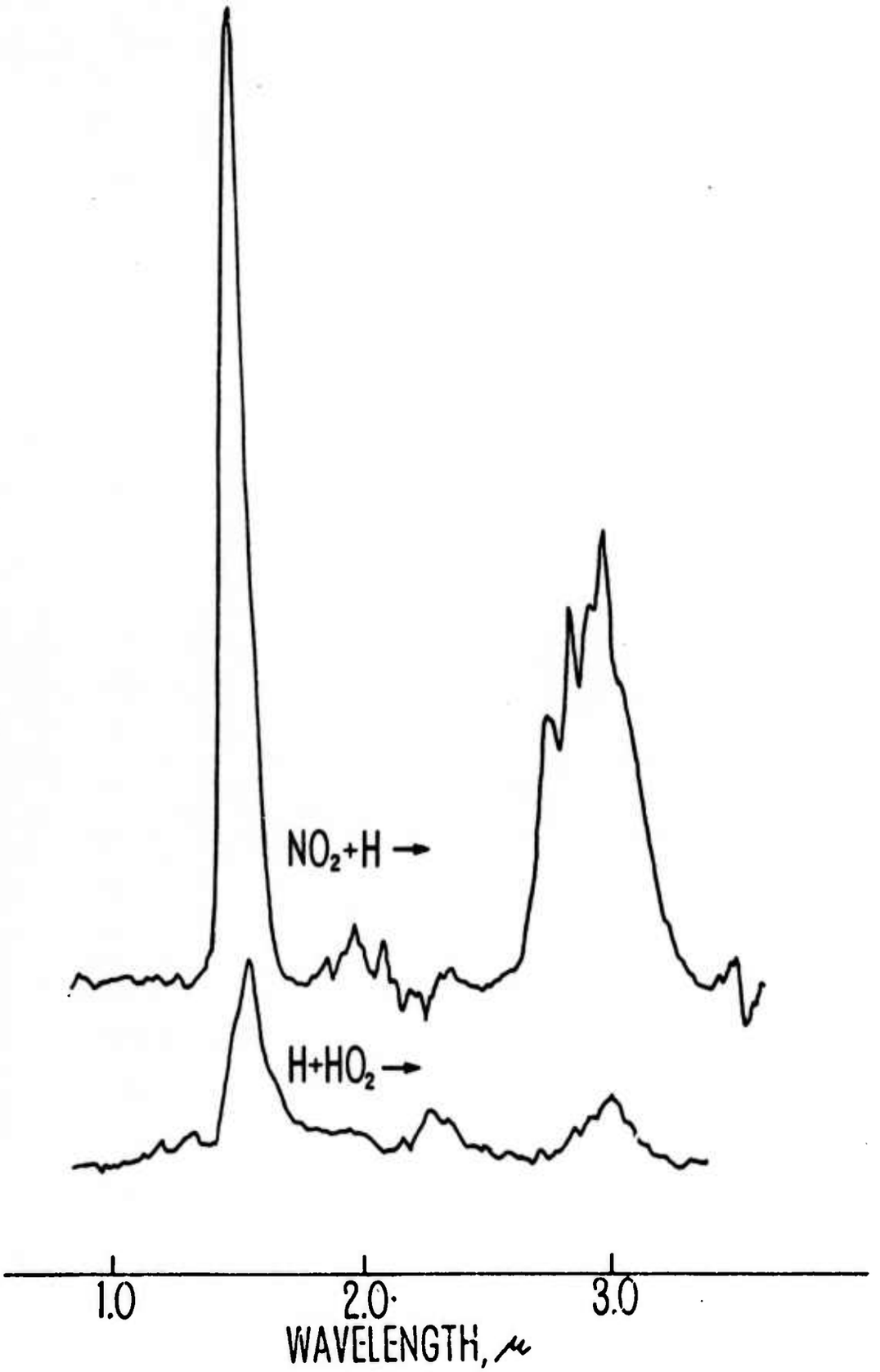

Figure 4: The low resolution spectrum of H + NO_2 compared to H + HO_2. 3200 μ O_2, 222 μ H_2, 774 μ He, 5 μ NO_2, 2 msec. time to observation, 2000 μ slits.

Our initial hypotheses for the $H + NO_2$ system were formulated on the basis of low resolution spectra illustrated in Figure 5. Based on the work of Kadaj (1973), it appeared that $O + C_2H_4$ gave vibrationally excited OH which radiated at 2.7μ via

$$CHO + O \rightarrow CO + OH^{\ddagger}$$

and at 1.5μ in the overtone. The reaction of CHO + O is exothermic by 79 kcal and can therefore produce hot bands in both the fundamental as well as the overtone. Hot band detection in the fundamental cannot be carried out with great sensitivity because the PbS detector loses sensitivity beyond 3μ. The reaction of $H + NO_2$ was presumed to yield OH fundamental and overtone radiation in the primary step, although the hot bands are not probable since this reaction is only exothermic by 26.4 kcal, resulting in a maximum excitation of v = 2 in the product OH. No bands at 2.3μ such as those present in the $O + C_2H_4$ spectrum are found which is consistent with the conclusion that the 2.3μ band from $O + C_2H_4$ was CO overtone radiation. As shown in Figure 5, the $O + N_2H_4$ spectrum appears to be significantly different and on the basis of the expected kinetics, it is probable that the 2.7μ radiation is due to H_2O ($\nu_1 + \nu_3$). The presence of a 1.9μ band is also consistent with the presence of water emission in the $O + N_2H_4$ reaction (vida infra).

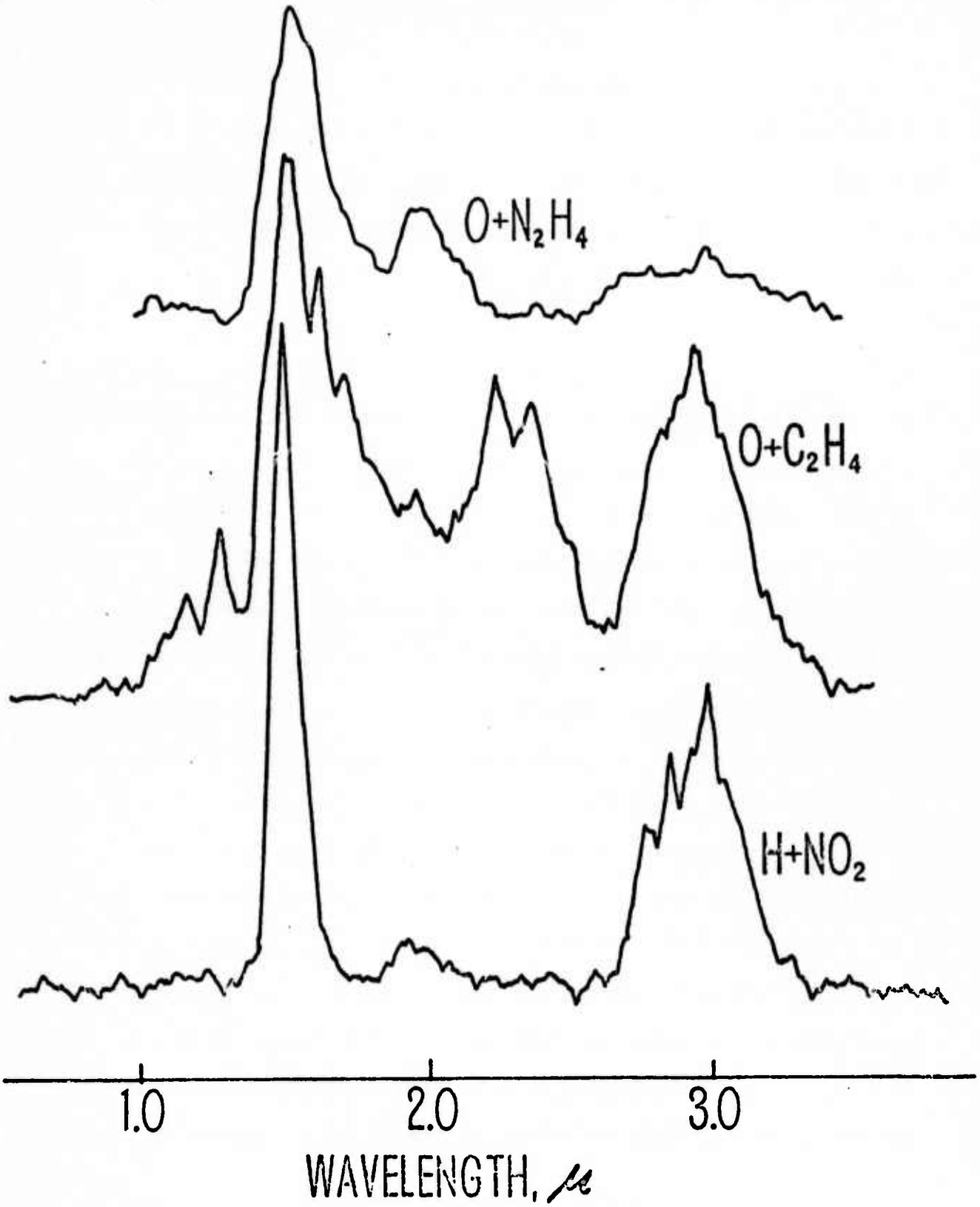

FIGURE 5. A comparison of low resolution spectra originating from $O + N_2H_4$, $O + C_2H_4$, and $H + NO_2$ under comparable conditions.

With these previous results in mind, we have re-examined the $H + NO_2$ system. In Figure 6, we have illustrated a higher resolution ($\lambda/\Delta\lambda \doteq 300$) spectrum resulting from that chemiluminescent reaction. Similar resolution spectra have been taken of $O + C_2H_4$ and no structure such as that found in Figure 6 has appeared. We must therefore conclude that the emission in the $O + C_2H_4$ system is not, as we had previously concluded, emitted from the same molecule albeit with higher excitation, as that occurring in the $H + NO_2$ system. Murphy (1974) has taken high resolution interferometric observations of the $H + NO_2$ system and concluded that both NO and OH, but not H_2O emission is present in the chemiluminescent spectrum. Our observations are consistent with $OH^{\ddagger}$ being the major emission source in the 2.7μ region for $H + NO_2$. From the structure observed in this $OH^{\ddagger}$ spectra, we believe that $OH^{\ddagger}$ is not the emitting species in the $O + C_2H_4$ system at 2.7μ.

To assist in drawing these conclusions from our spectra, synthetic spectra of NO and OH were drawn via the Calcomp plotter (see Part II). These are shown in Figures 7 and 8. Precise agreement with the experimental spectra is lacking for several possible reasons. First, there is an uncertainty of $\Delta\lambda = 0.002\mu$ in the wavelength position of the experimental spectra due to gearing of the monochrometer and recorder drive trains. Second, the chemiluminescent reaction of $H + NO_2$ does not necessarily produce a Boltzmann distribution of vibrational levels; an assumption inherent in the models illustrated in Figures 7 and 8.

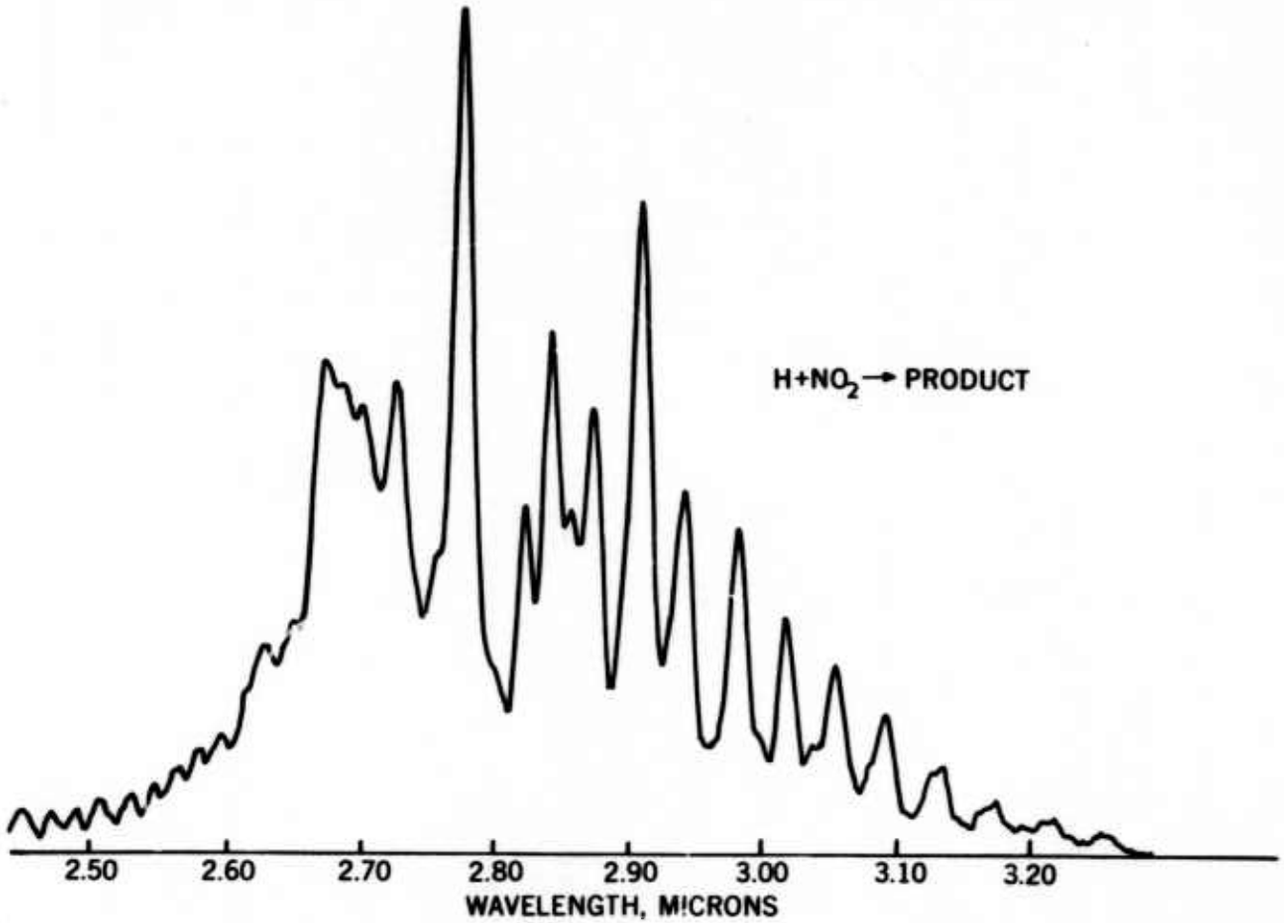

Figure 6: Moderate resolution spectrum of chemiluminescence from H + NO_2: 4 NO_2, 7-10 H, 69 H_2, 1026 He+Ar, 500 entrance and 1000 exit slits, observation time about 1.5 msec.

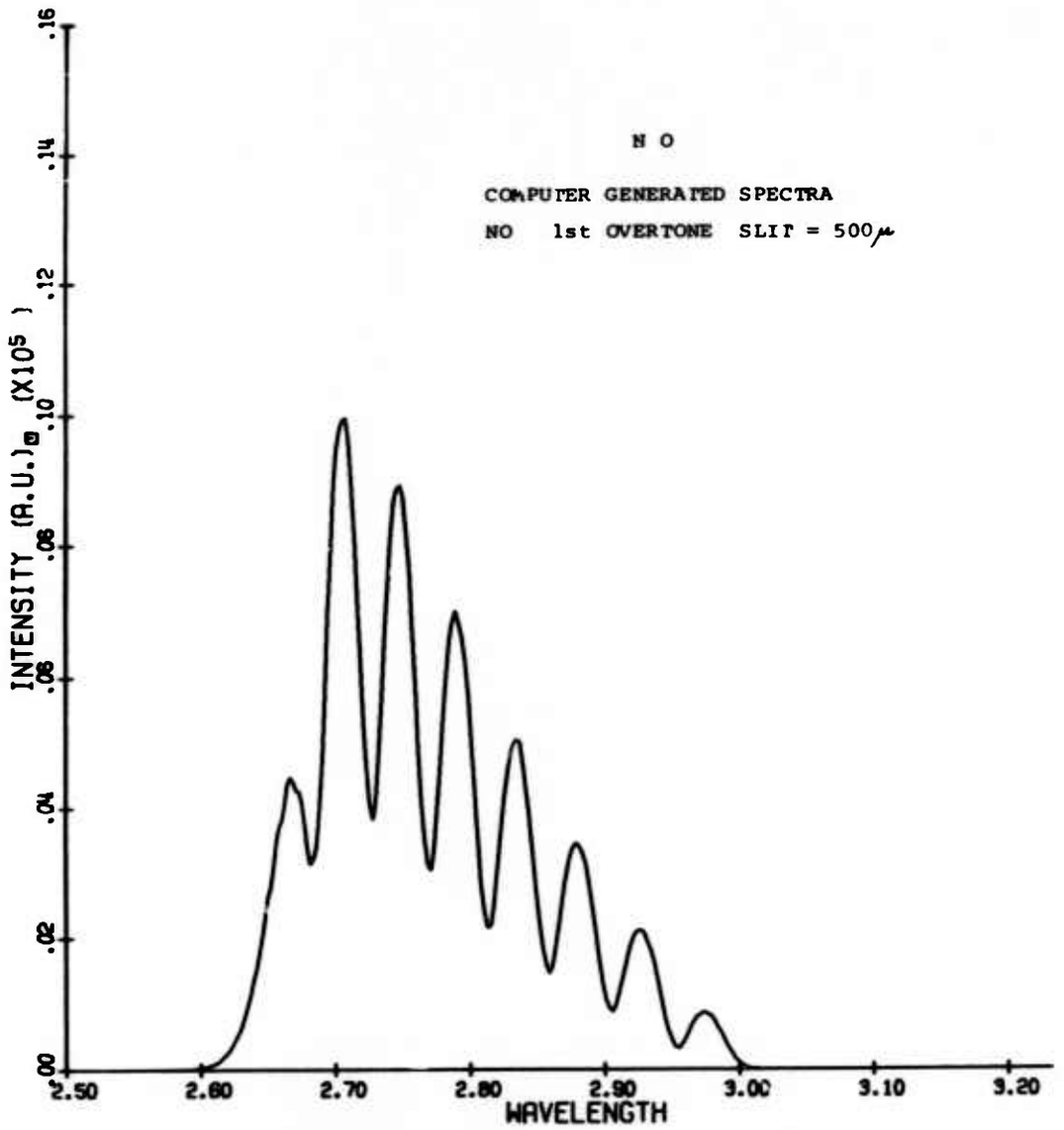

Figure 7: Artificial First Overtone Spectrum of NO.

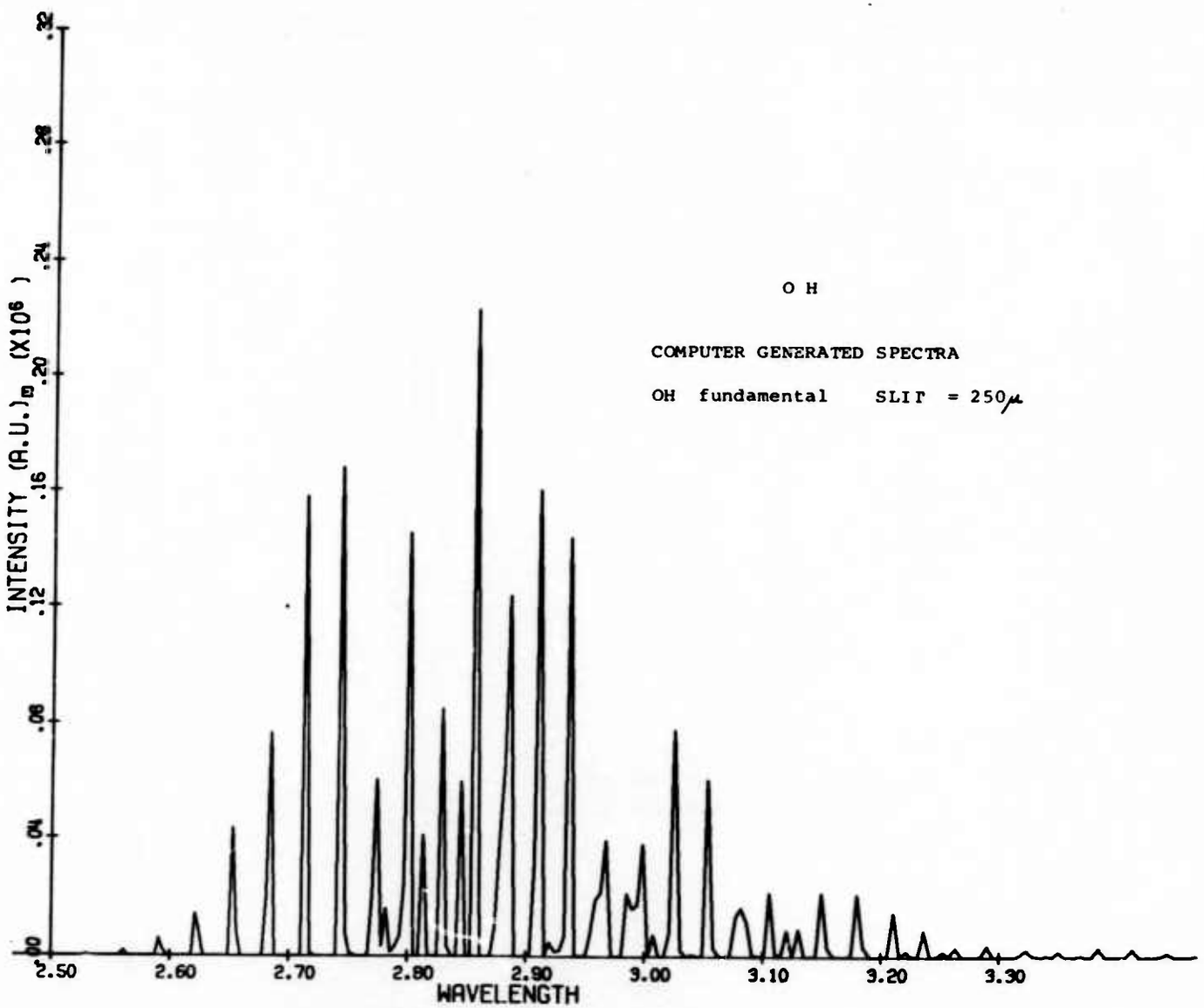

Figure 8: Artificial Fundamental Spectrum of OH using Spectroscopic Parameters from Herzberg.

For this latter reason, we obtained the high resolution OH spectrum from the $H + 0_3$ reaction from Murphy (1971). Since our measurements were made with a relatively low resolution monochromator (i.e. 1000μ), we integrated Murphy's line by line measurements over a 1000μ slit formation to give the low resolution spectrum shown in Figure 9. The prominent Q-branch transitions of Murphy's integrated measurements agree well with the prominent features shown in Figure 6. Due to the low exothermicity of the $H + NO_2$ reaction as compared to the $H + 0_3$ reaction, the peak distribution is different between the two reactions. However, the agreement between the Q-branch features leads us to conclude that $OH^{\neq}$ is the major radiator at 2.7μ from $H + NO_2$. The contribution of the NO overtone to the 2.7μ emission is, at present, unresolved since only preliminary measurements have been made in the 5-6.5μ region and these are complicated by the possible presence of H_20.

Figure 9: Low resolution artificial spectrum of OH from the Measurements of Murphy(1971).

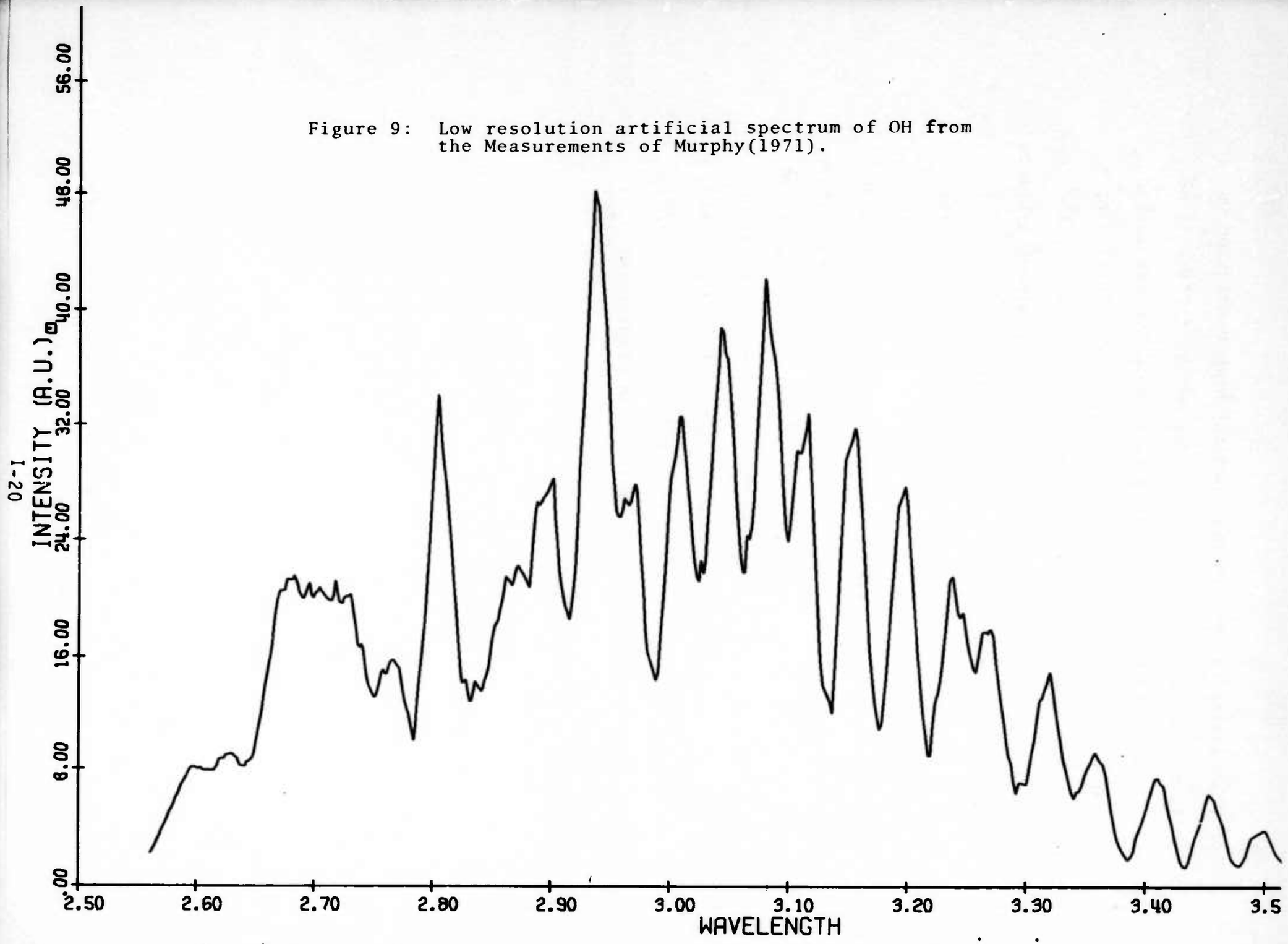

B. $O + N_2H_4$

$N_2H_4 \cdot H_2O$ was heated under vacuo and introduced downstream of the O discharge. A low resolution profile of the resulting $O + N_2H_4$ was given in Figure 5. A higher resolution spectrum is given in Figure 10. Where the NO overtone emission predominates, according to the NO synthetic spectrum illustrated in Figure 7, no emission is found in the $O + N_2H_4$ spectrum. On the other hand, a new band between 2.5 and 2.6μ appears in $O + N_2H_4$. This peak caused the broader appearance of the $O + N_2H_4$ band shape relative to $O + C_2H_4$ and $H + NO_2$ in the comparison of Figure 5. However, the prominent peaks at 2.76 and 2.9μ and the regularly spaced peaks between 2.9 and 3.2μ do closely resemble $H + NO_2$ although the intensity fall off with increasing wavelength is much less than for $H + NO_2$. In fact, the intensity is undoubtedly increasing near 3.2μ because the spectral response of the PbS tube and the efficiency of the monochrometer (2.1μ grating blaze) are both falling off rapidly in that spectral region.

The reaction

$$O + N_2H_4 \rightarrow N_2H_2 + H_2O$$

is 89.24 kcal exothermic. The reaction

$$O + N_2H_4 \rightarrow N_2H_3 + OH$$

is only 36.12 kcal exothermic and is reported by Foner and Hudson

$O+N_2H_4 \rightarrow H_2O+N_2H_2$

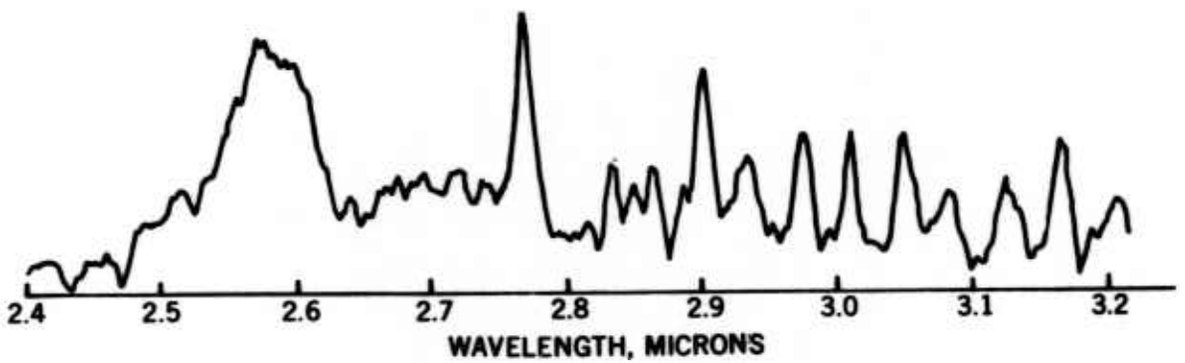

Figure 10: Infrared spectrum for O + N_2H_4 reaction. 7μO, 83$\mu$$O_2$, 663$\mu$He, 245$\mu$Ar, ~5$\mu$$N_2H_4$, 500$\mu$ entrance and 1000μ exit slits.

(1970) to be only 1/25th as fast as the H_2O formation reaction. Thus, the branch producing OH has a rate constant of about 10^{-12} cc/sec and is only as exothermic as $H + NO_2$ which is twenty times as fast. Thus, it is difficult to explain the apparent similarity in wavelength and band spacing of $O + N_2H_4$ and $H + NO_2$ between 2.9 and 3.2μ. In this case the intensity changes appear to be more significant than the wavelength positions. The fact that emission is observed out to 2.5μ strongly suggests that H_2O is a major contributor to the 2.7μ emission as shown in Figure 10. Kinetic modeling of this reaction system has not yet been completed to further verify these conclusions.

C. $O + NR_3$

In order to evaluate the effect of substitution on amines, oxidation by O atoms, a series of experiments using tertiary amines were run. Trimethyl, triethyl, and tripropyl amines were introduced by heating the liquids at reduced pressure and bubbling argon through the heated liquid. Because of the greatly varying vapor pressures of these compounds it was difficult to control the partial pressures to preset values. Nonetheless, from the observed spectra several conclusions can be drawn. In the near ultraviolet and visible spectral region, as shown in Figure 11, the most prominent peak is the $OH(A \rightarrow X)$ electronic emission at 3064 A (and the second order at 6128 A). Also observed are the $CH(A \rightarrow X)$ at 4312 A and an enhancement of the 7600 A region which also appears in the background from the discharged O_2. Comparing this to our $O + NH_3$ spectrum the likely radiator is $HNO^{\ddagger}$. It is evident from a comparison of these tertiary amine + O spectra with O + HC spectra taken from previous work (Krieger and Kummler, 1973) in Figure 12 . .at the hydrocarbon fragments play a dominant role in the chemiluminescent process.

In the infrared spectra illustrated in Figure 13 we also find that our spectra for tertiary amines resemble those for hydrocarbon + O illustrated in Figure 5. This fact is particularly apparent by reference to the 2.5 - 2.6μ region where the substituted amines show little emission in contrast to hydrazine but in agreement with $O + C_2H_4$. No infrared signature for $O + NH_3$ is observed in the 2.7μ region.

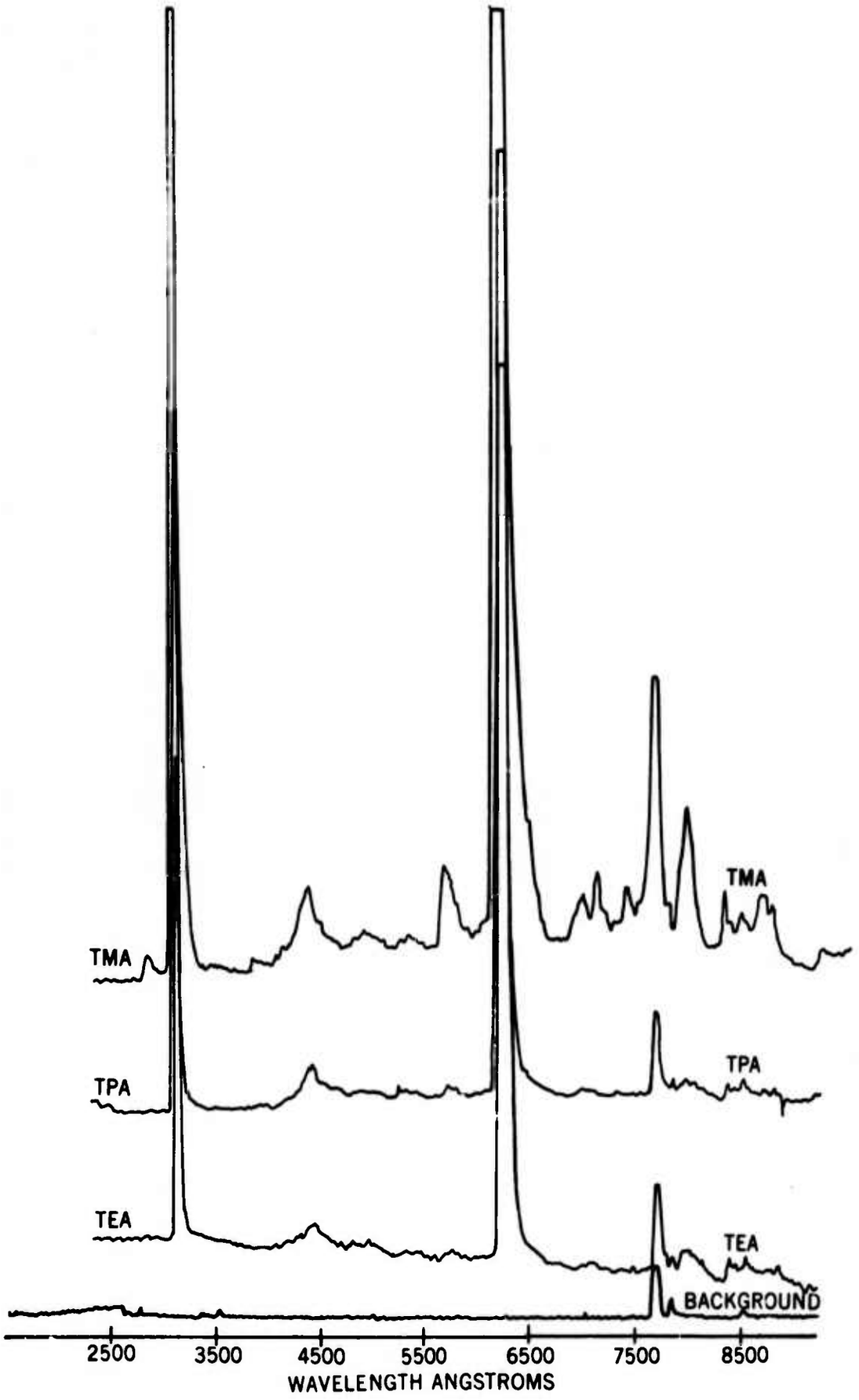

Figure 11: Comparative visible chemiluminescence from the attack of O atoms on several substituted amines. The prominant feature at 3100 A is OH*, the second order of which is at 6200 A.

Figure 12: A comparison of the emission spectra for O atom attack on C_2H_2, C_6H_6 and C_2H_4. The prominant lines in the background at 5875, 7775 and 8446 are He lines scattered from the discharge. $O_2(^1\Sigma)$ is also detected in the background at 7620 A.

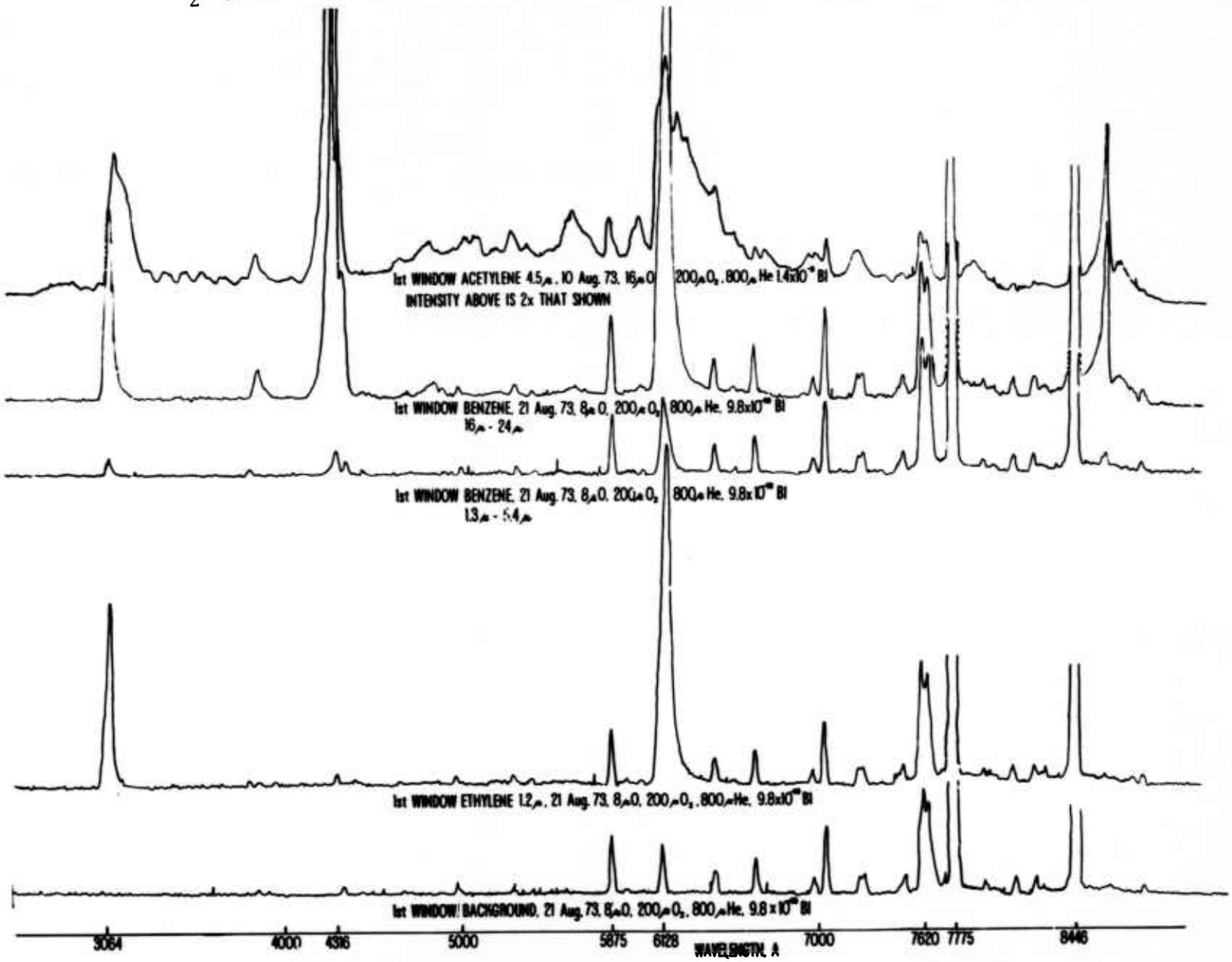

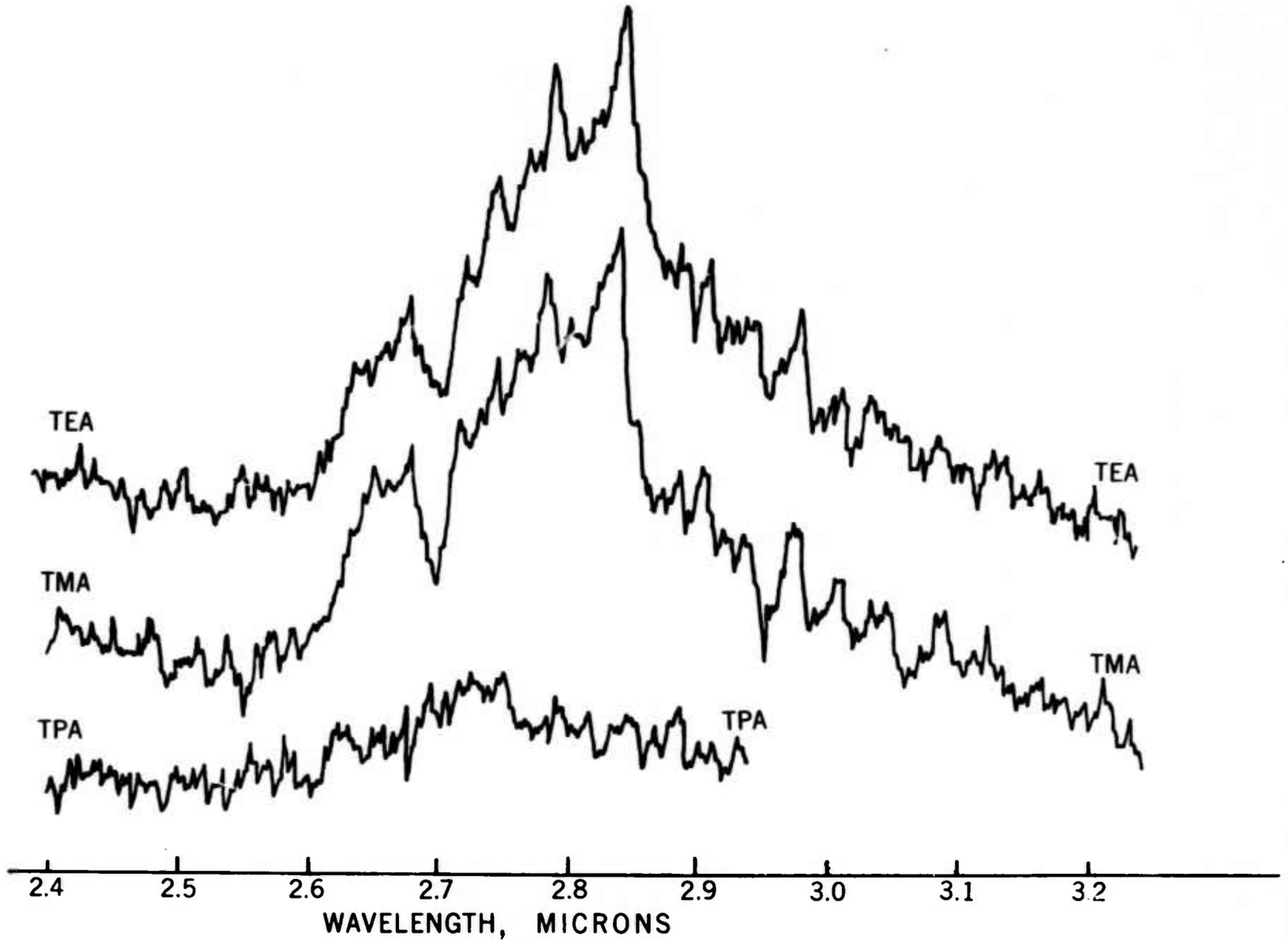

Figure 13: Comparative infrared spectrum for the O atom attack on several substituted amines.

LITERATURE CITED

Albers, E., K. Hoyermann, H. Wagner, and J. Wolfrum, Twelfth Symp (Int.) on Combustion, The Combustion Institute, Pittsburgh, Pa., 313 (1969).

Bahn, G., Pyrodynamics 5, (1967).

Foner, S.N. and R. L. Hudson, J. Chem. Phys. 53, 4377 (1970).

Gehring, M., K. Hoyermann, H. Wagner, and J. Wolfrum, Ber. Bunsenges. Physik. Chem. 73, 956 (1969).

Gehring, M., K. Hoyermann, H. Wagner, and J. Wolfrum, Z. Naturforsch. 25A, 675 (1970).

Gehring, M., K. Hoyermann, H. Wagner, and J. Wolfrum, Ber. Bunsenges. Physik. Chem. 75, 1287 (1971).

Kadaj, R., Master's Thesis, Wayne State University, Dept. of Chemical Engineering (1973).

Kondratiev, V. N., Rate Constants of Gas Phase Reactions, Reference Book, translated by L. Holtschlag, R. Fristrom (ed.), NSRDS Publication COM-72-10014, Jan. (1972).

Krieger, B., M. Malki and R. Kummler, Environmental Science and Tech. 6, 742 (1972).

Krieger, B. and R. Kummler, Paper 42B, presented at the 74th Nat'l meeting of AIChE, New Orleans, Louisianna (1973).

Kummler, R., E. Fisher and F. Boynton, "Substituted Hydrazine Chemistry and Chemiluminescence in High Altitude Plumes," AFCRL-TR-73-0727; PD-73-041, Scientific Report No. 4 on Contract F19628-72-C-0006, August (1973).

Kummler, R., E. Fisher, E. Jamshidi, M. Malki, B. Krieger, R. Kadaj, and D. Lalas, "Analytical Laboratory Studies on Upper Atmospheric Energy Transfer Processes," AFCRL-TR-73-0605, August (1973).

Murphy, R., private communication, (1974).

Sawyer, R. and I. Glassman, Eleventh Symp (Int.) on Combustion, The Combustion Institute, Pittsburge, Pa., 861 (1967).

PART II: Artificial Spectra of Diatomics of Plume Interest

William B. Ruley* and Edward R. Fisher

* Senior in Chemical Engineering

Introduction

In order to interpret the extensive infrared measurements described in the previous section, an analytical model was developed to predict the non-equilibrium band spectra associated with several diatomic molecules of interest. This section describes this analytical model and the computer code used to generate artificial infrared spectra*. The code uses anharmonic energy parameters and line strengths as obtained from Herzberg[1]. The vibrational distributions for the diatomic species can be assumed as either Boltzmann or input in any form desired. The rotational distributions are assumed to be Boltzmann which is consistent with the experiments above.

The program performs a line-by-line calculation for a predetermined number of hot bands, then integrates the compiled intensity versus wavelength values over an arbitrary slit function. Figure 1 shows a block diagram of the program. Input data to the MAIN routine includes the number of vibrational levels to be considered,N; the maximum vibrational level included,IVMAX; the initial vibrational level,IV; the Δv transition to be considered, IVP; a Q-branch key,LAMBDA; the vibrational and rotational constants,WE1,XE1,YE1,BE and AE; an appropriate set of

*preliminary code written by R. Marriott.

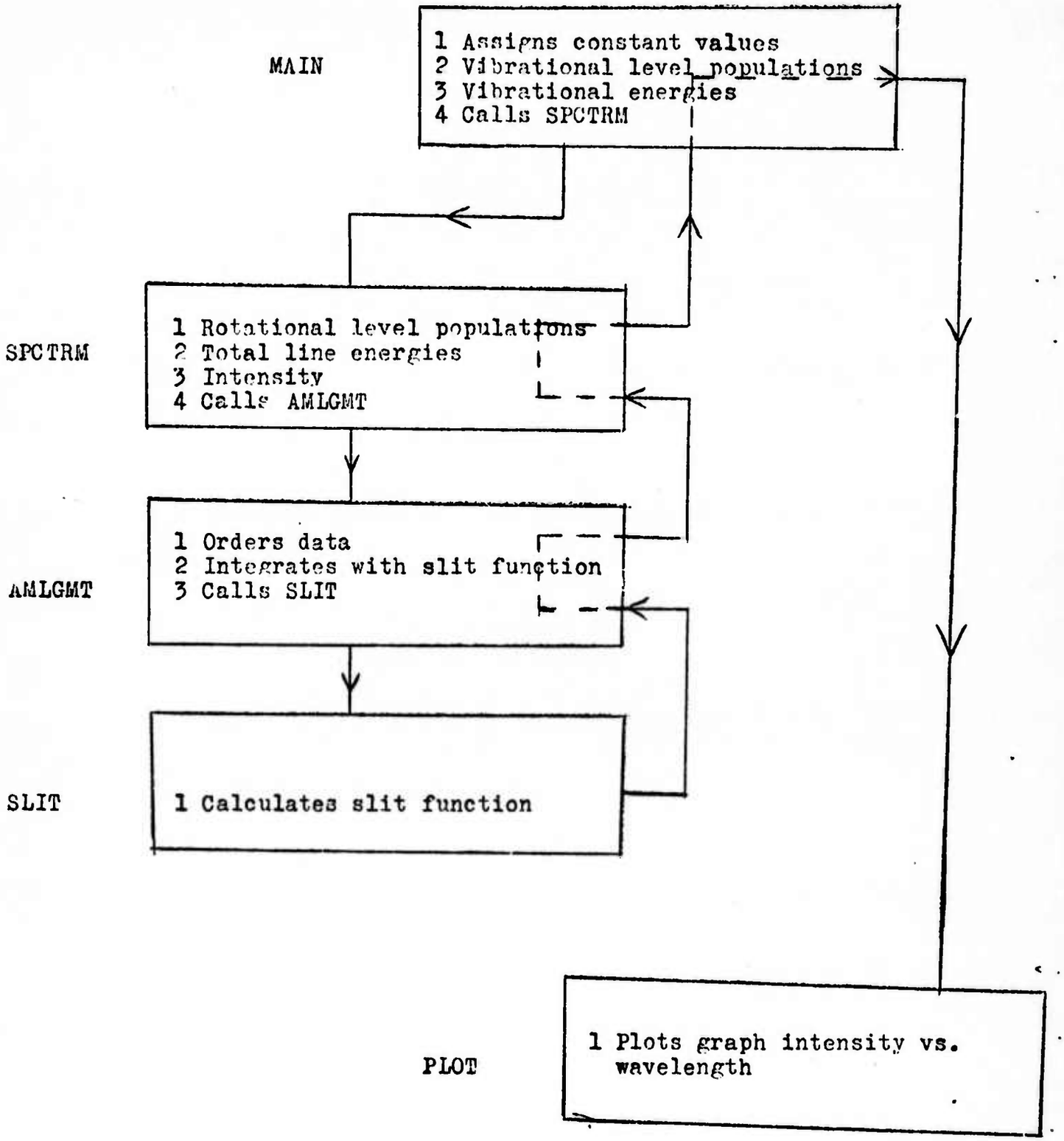

Figure 1: Block Diagram of the Spectra Code

Einstein A-Coefficients,A(I); the rotational and vibrational temperatures,TE and TV; the slit width, S; and a parameter,DE, used in controlling the movement of the slit function across the line-by-line spectra. The MAIN routine calculates the vibrational energies and population distributions then calls subroutine SPCTRM. The maximum J value required for the calculation is calculated in SPCTRM followed by the line energies for the P,R, and Q branches. The emission intensities for each of the permitted transitions are then calculated using the appropriate A-coefficients. Subroutine AMLGMT is then called to order the line energies in order of decreasing wavelength. The corresponding line intensities are then integrated over a triangular or Gaussian slit function in energy increments of DE. The spectral resolution of the calculation is governed by the input slit function width at half heighth,S. Subroutine PLOT then takes the assembled intensity versus wavelength data and generates a computer plot of the artificial spectra.

A compilation of non-equilibrium spectra generated by the code is given in the following Figures. Verification of the computer generated spectra for the case of CO has been done and shows very good agreement with experimental measurements.

Comparison of the Artificial Spectra
with Experimental Infrared Spectra
of CO Overtone.

CO 1ST OVERTONE

TR= 400 TV=4000

SLIT=250

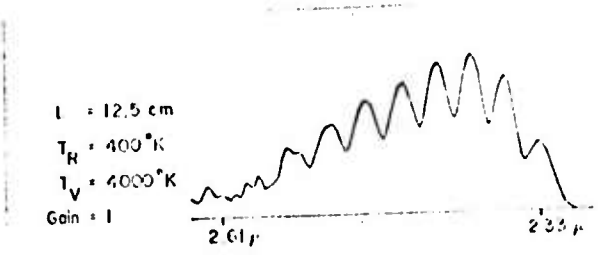

INTENSITY (A.U.)$_{\Omega}$ (X10^6)

.00 .05 .10 .15 .20 .25 .30 .35 .40

2.20 2.28 2.36 2.44 2.52 2.60 2.68 2.76

WAVELENGTH

Effect of the DE value of the Artificial Spectra of CO for stated conditions.

CO FUNDAMENTAL

TR= 300 TV=3000

SLIT=500

DE=0.5

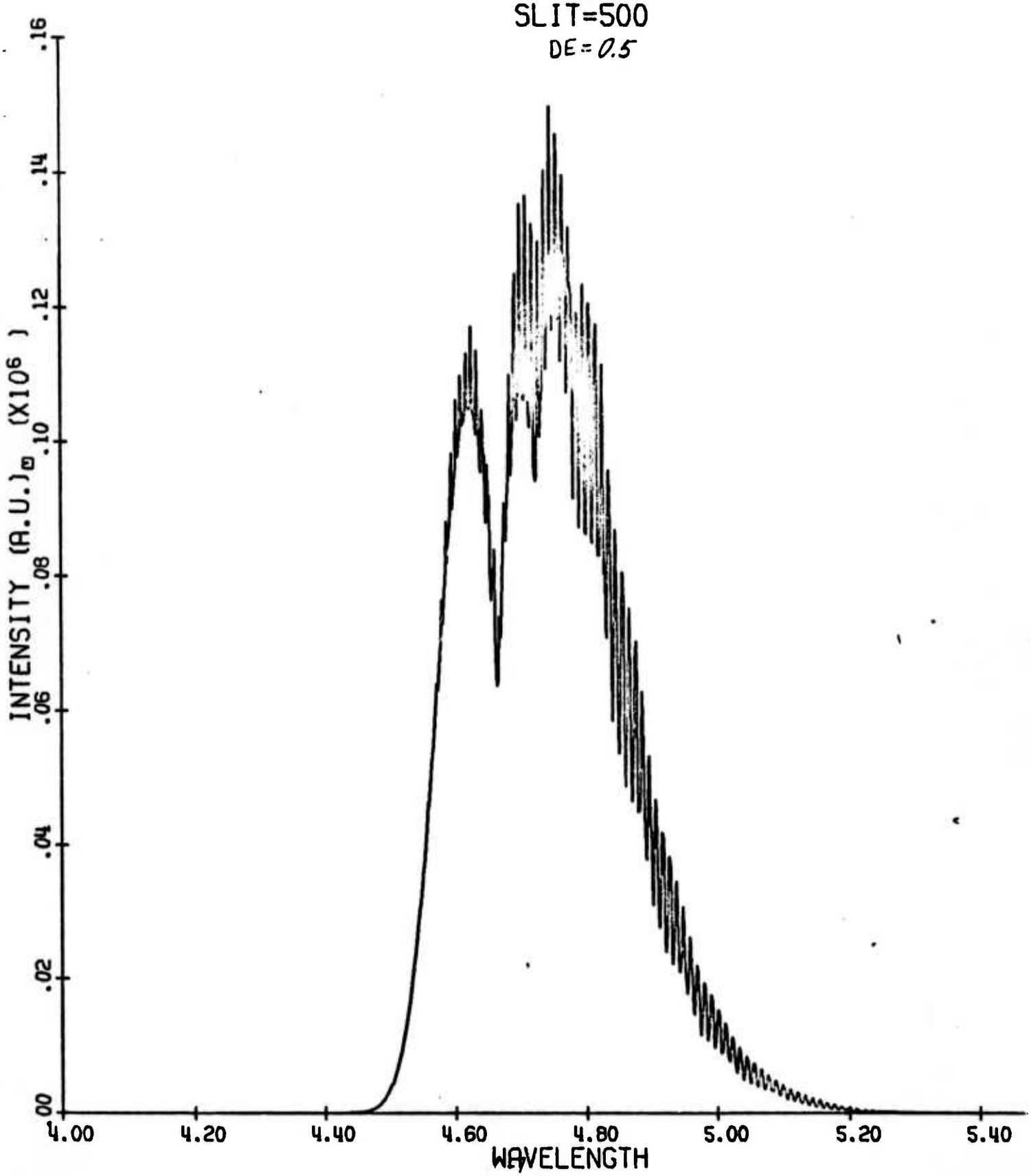

CO FUNDAMENTAL

TR= 300 TV=3000

SLIT=250

DE = 2.0

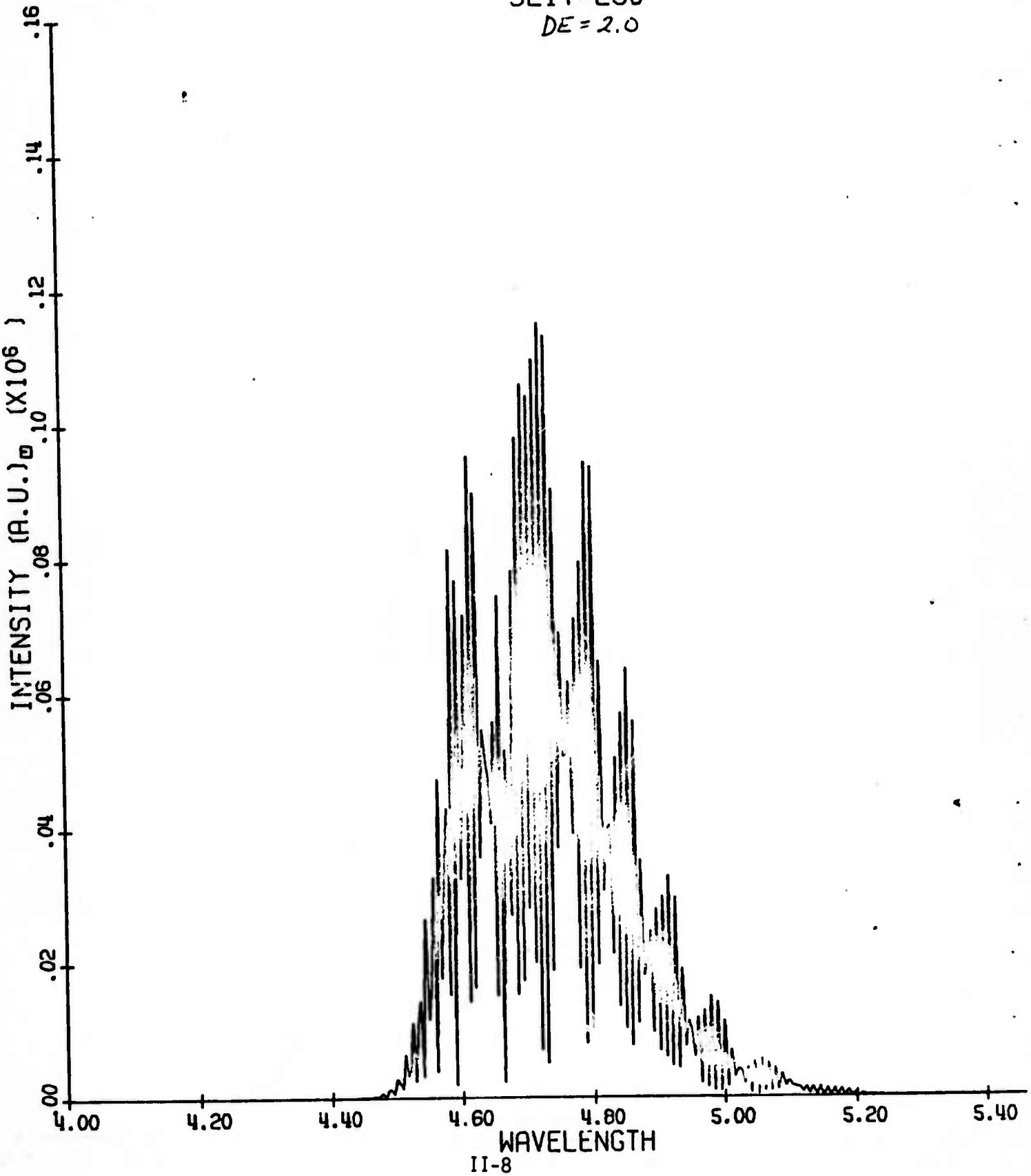

Appendix of Artificial Infrared Spectra for Several Diatomics of Interest

CO FUNDAMENTAL

TR= 300 TV=3000

SLIT=250

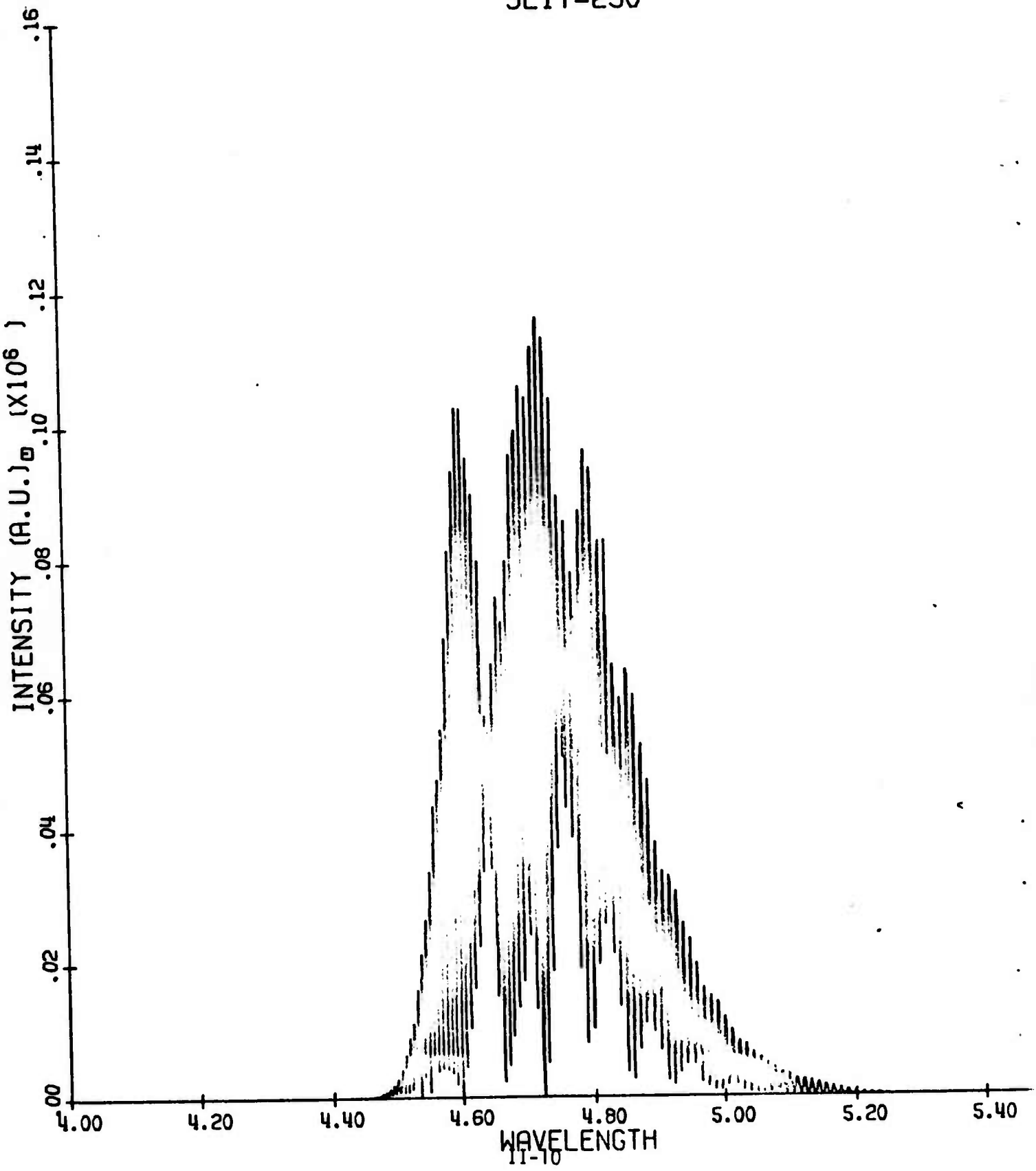

CO FUNDAMENTAL

TR= 300 TV=1000

SLIT=250

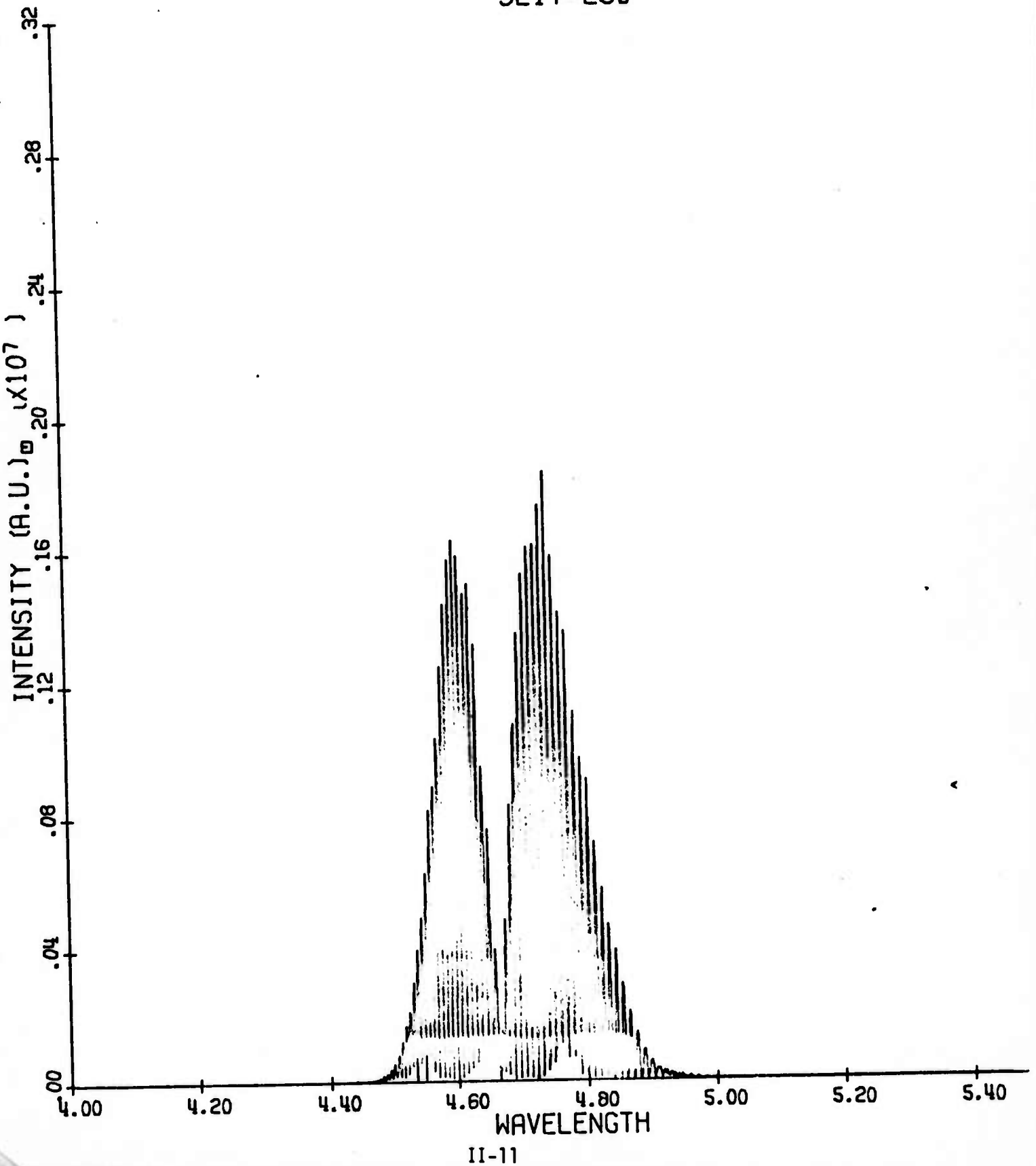

CO FUNDAMENTAL

TR= 300 TV= 300

SLIT=250

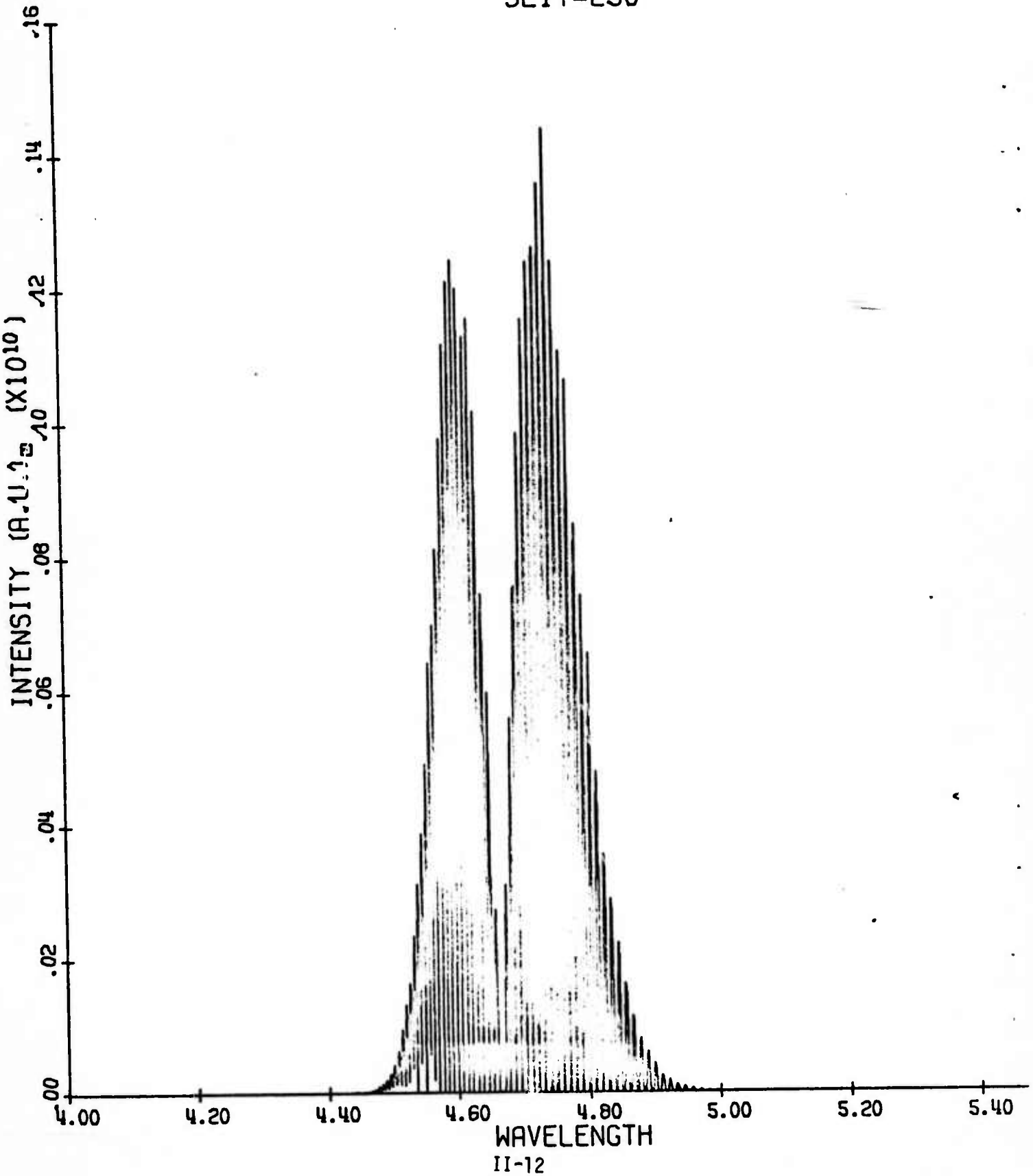

CO 1ST OVERTONE

TR= 300 TV= 300

SLIT=250

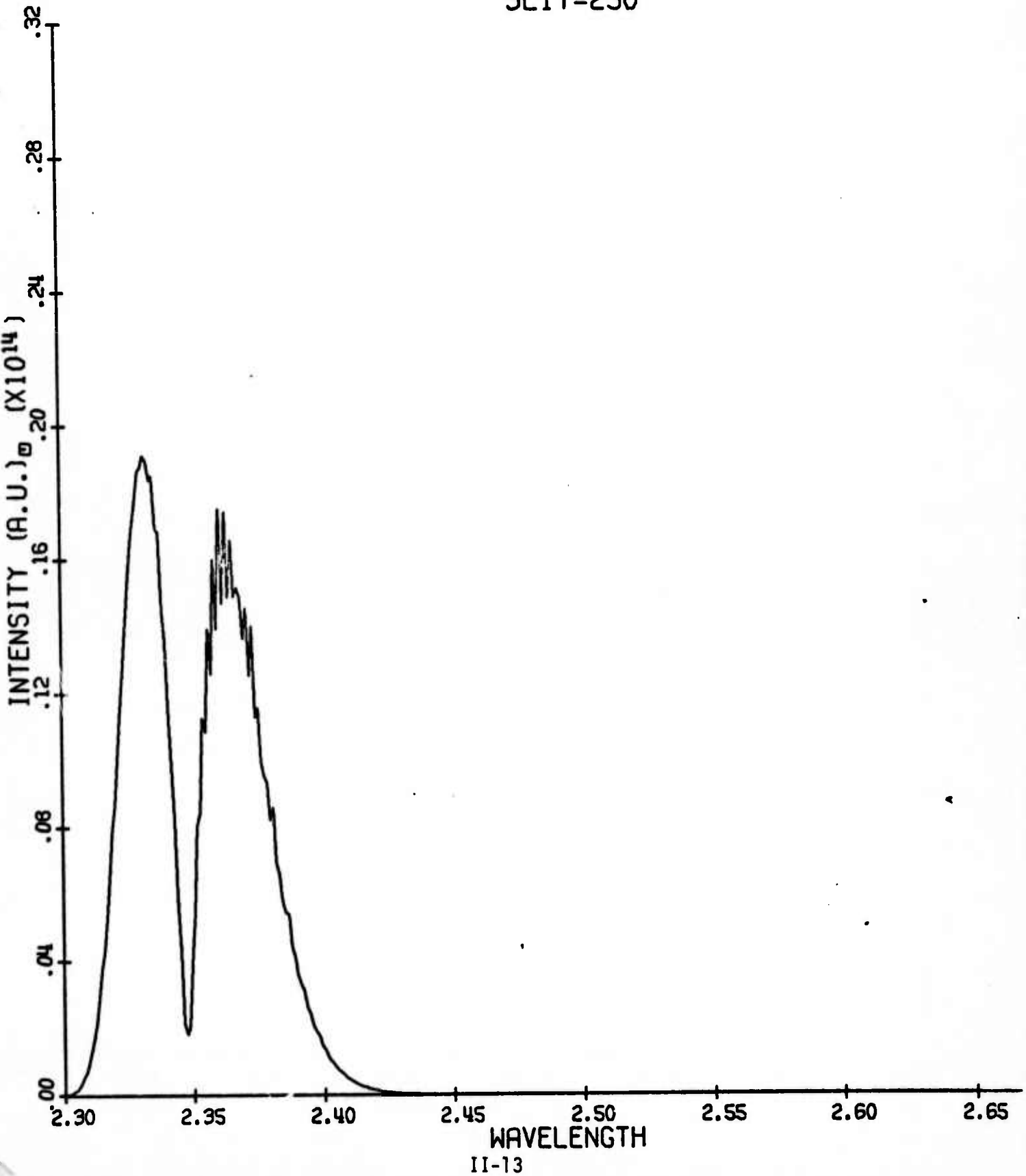

CO FUNDAMENTAL

TR= 500 TV= 500

SLIT=250

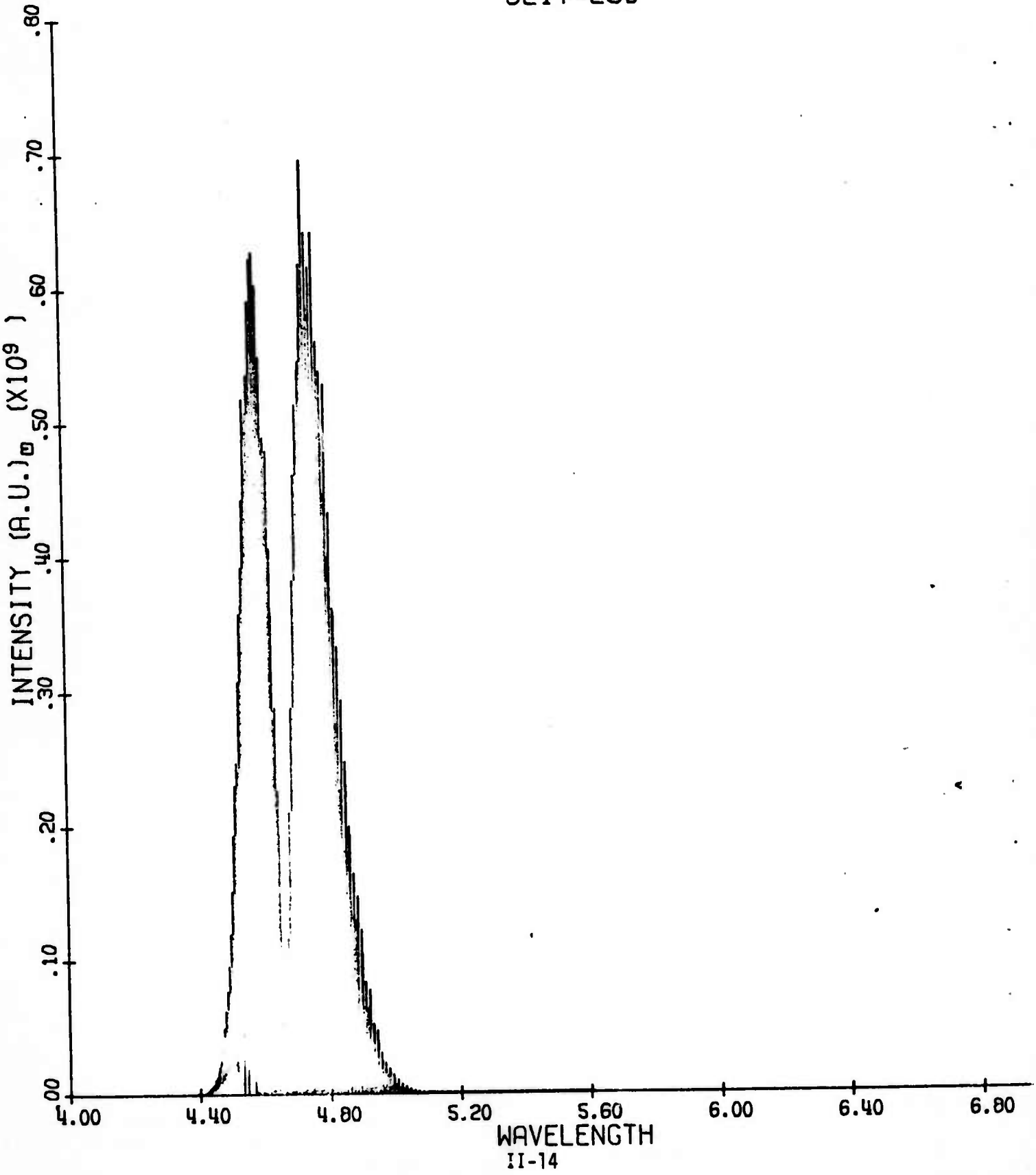

CO FUNDAMENTAL

TR= 500 TV=3000

SLIT=250

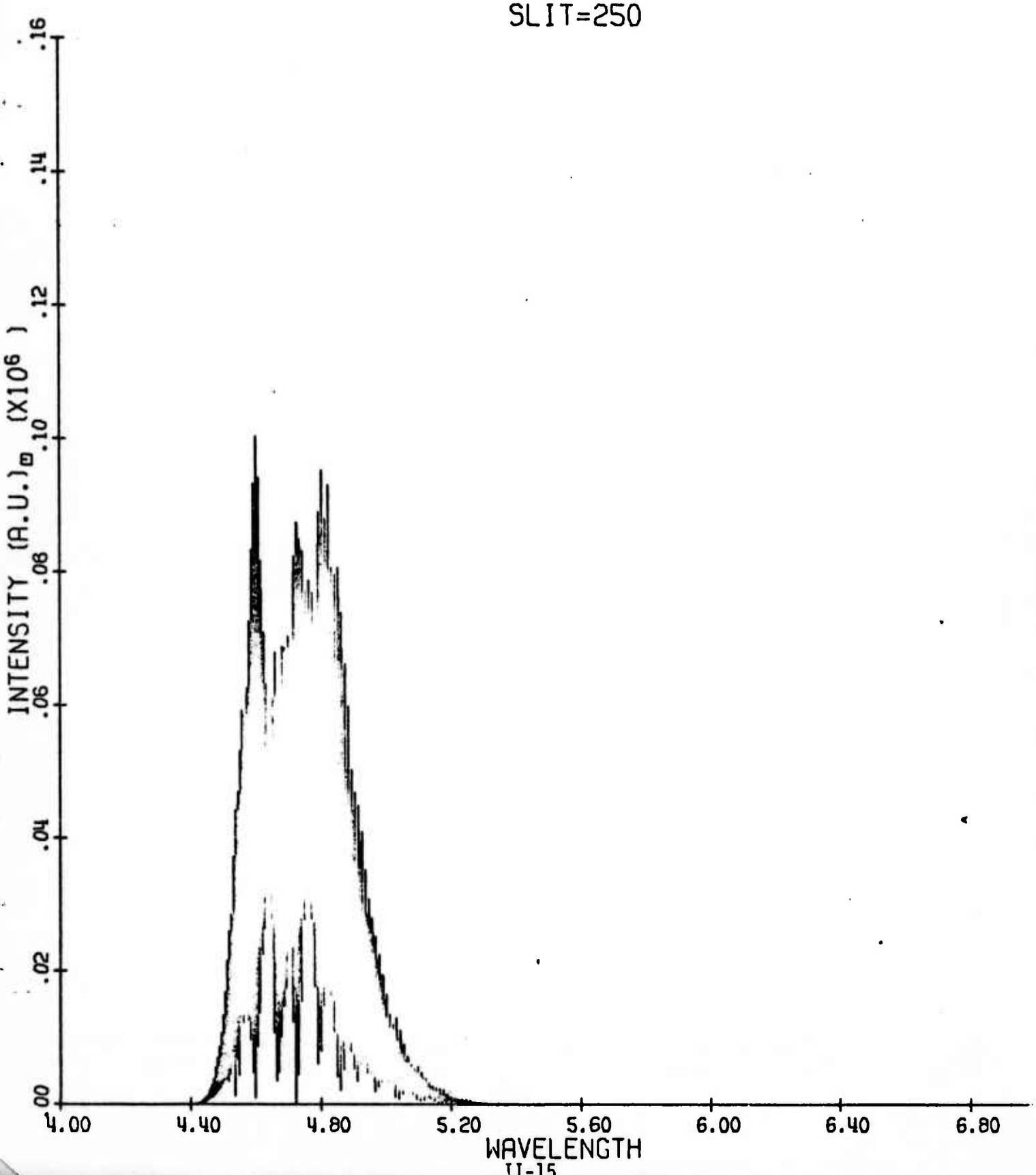

CO FUNDAMENTAL

TR= 500 TV=1000

SLIT=250

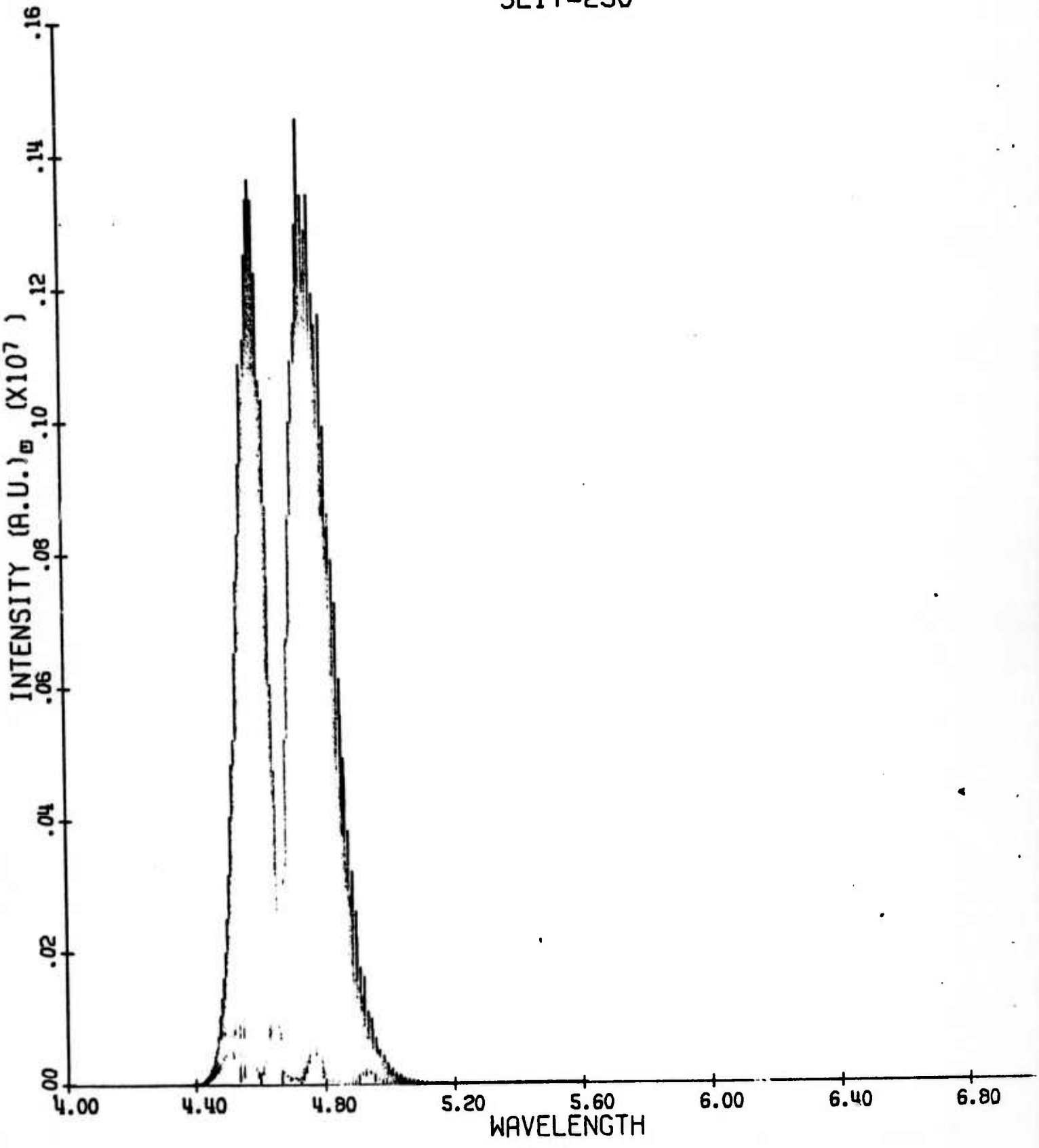

NO 1ST OVERTONE

TR= 300 TV= 300

SLIT=250

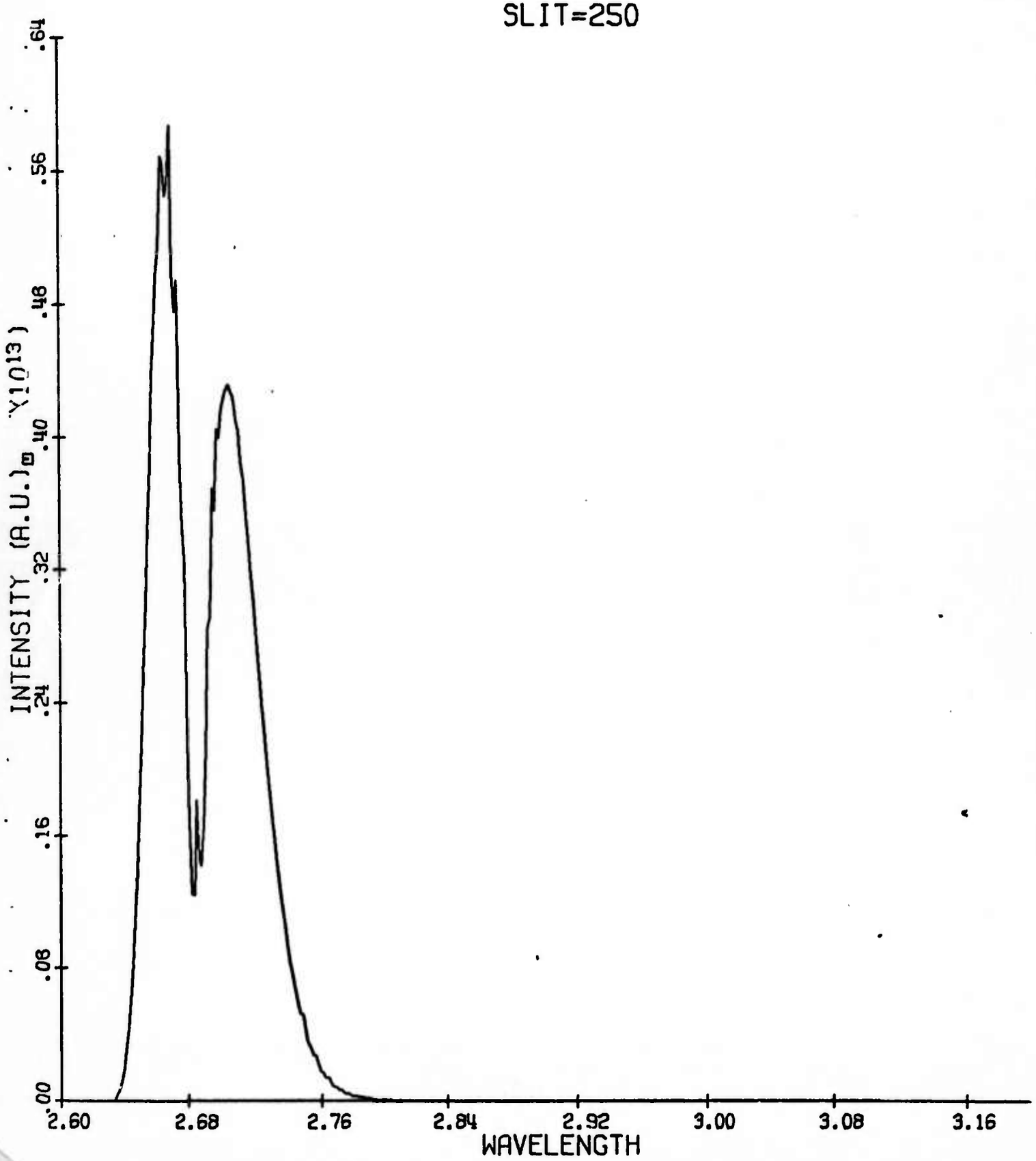

NO 1ST OVERTONE

TR= 300 TV=3000

SLIT=250

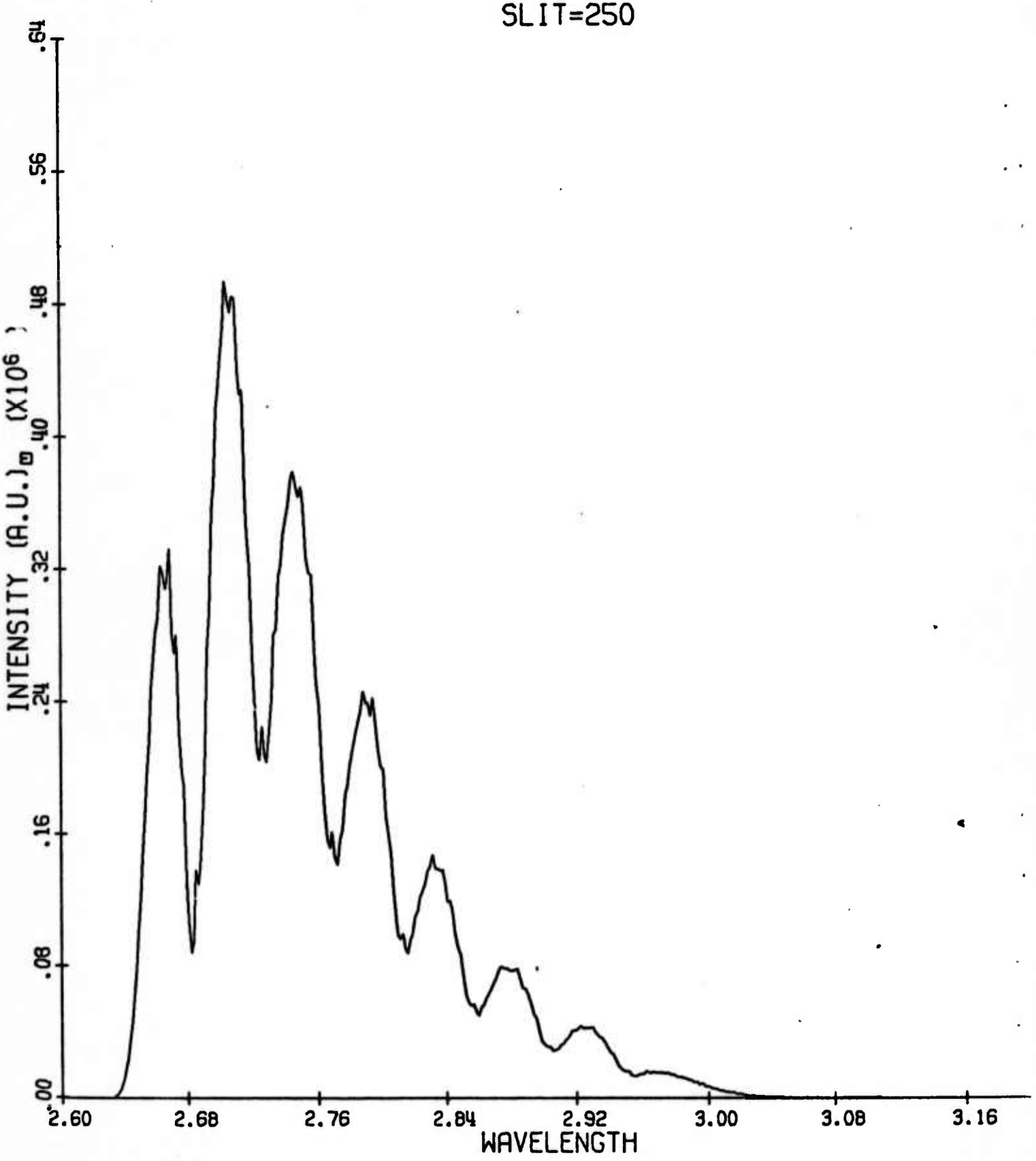

NO 1ST OVERTONE

TR= 500 TV=1000

SLIT=250

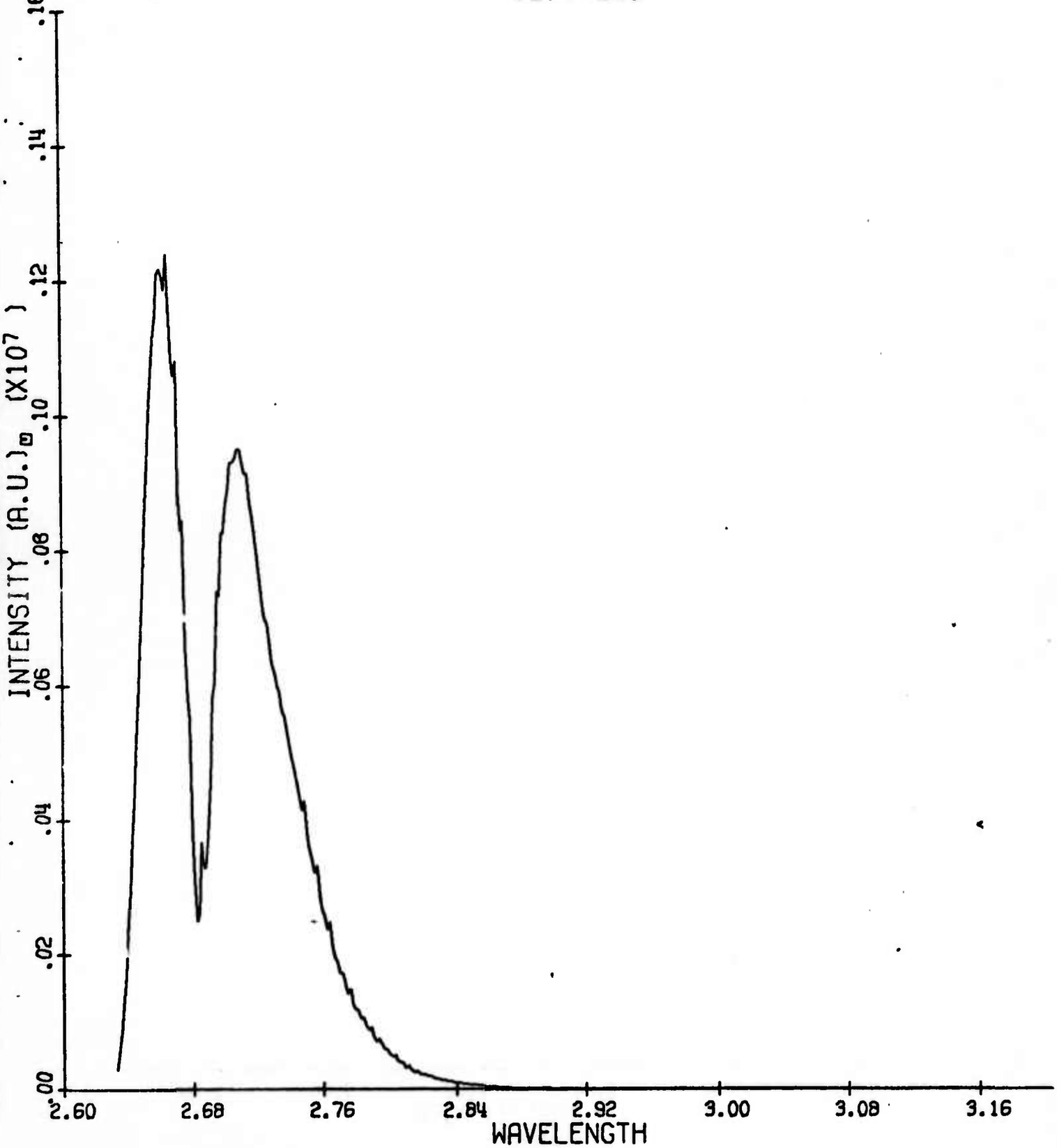

NO 1ST OVERTONE

TR= 300 TV=1000

SLIT=250

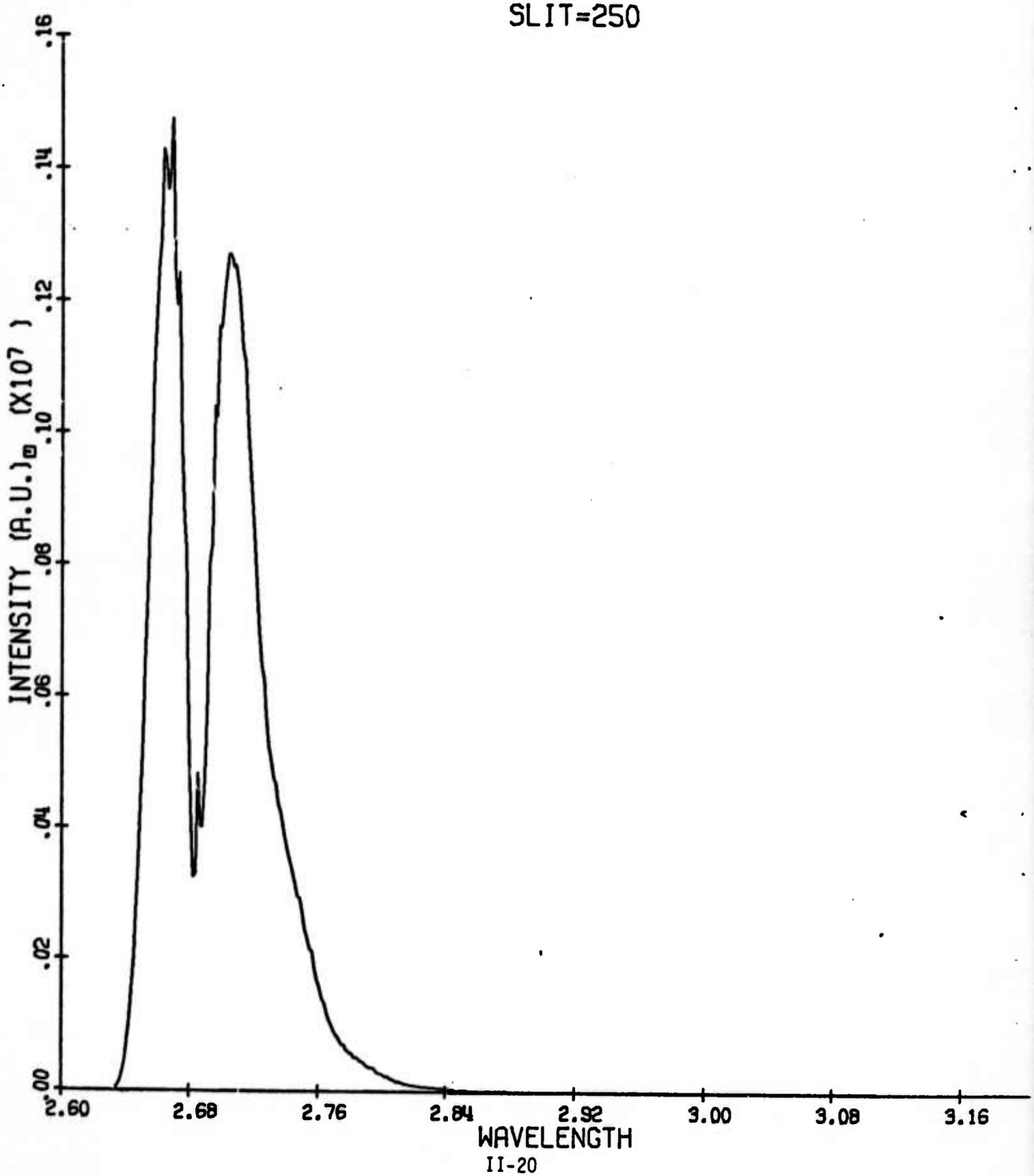

OH FUNDAMENTAL

TR= 300 TV=3000

SLIT=250

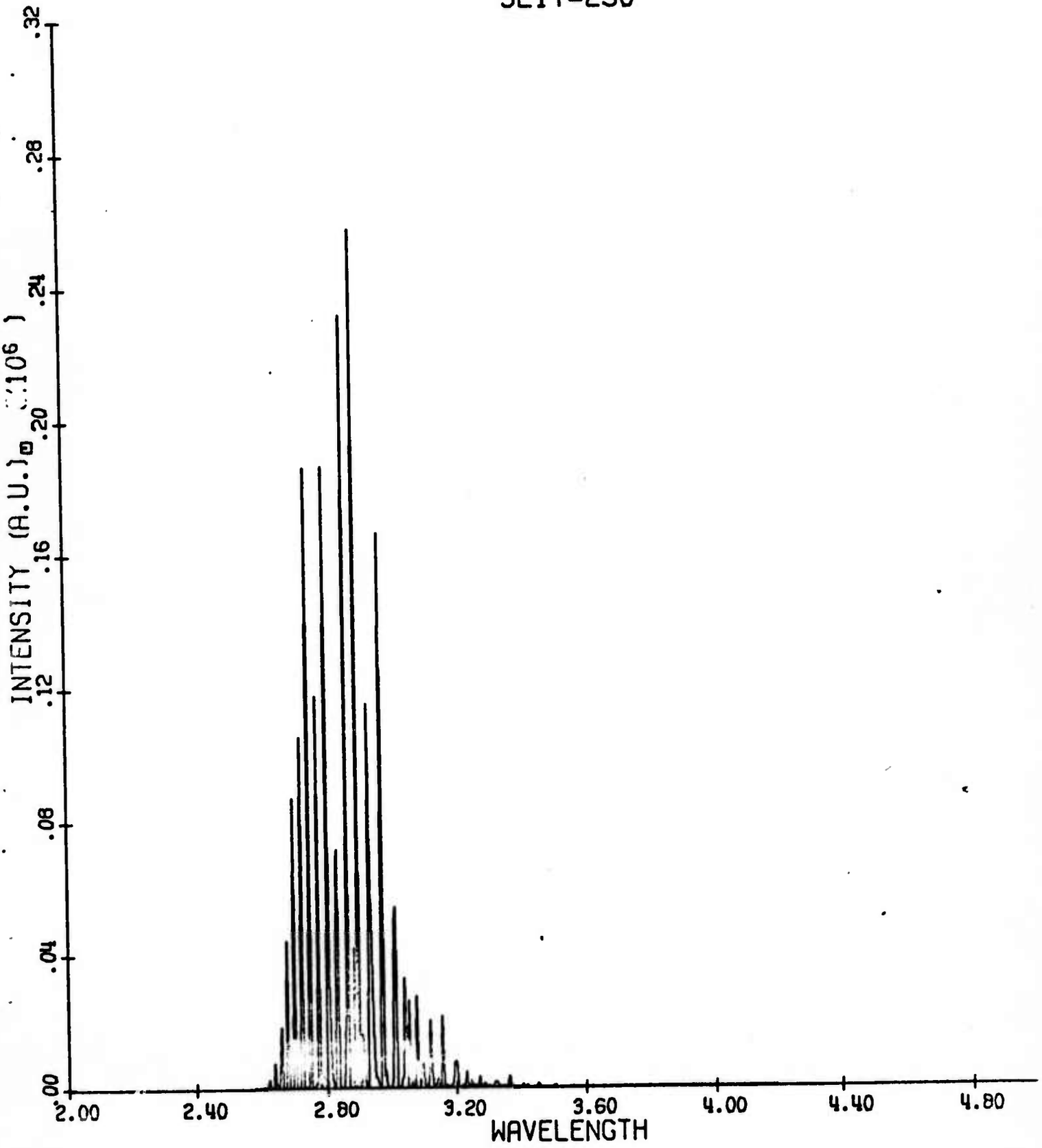

OH FUNDAMENTAL

TR= 300 TV=1000

SLIT=250

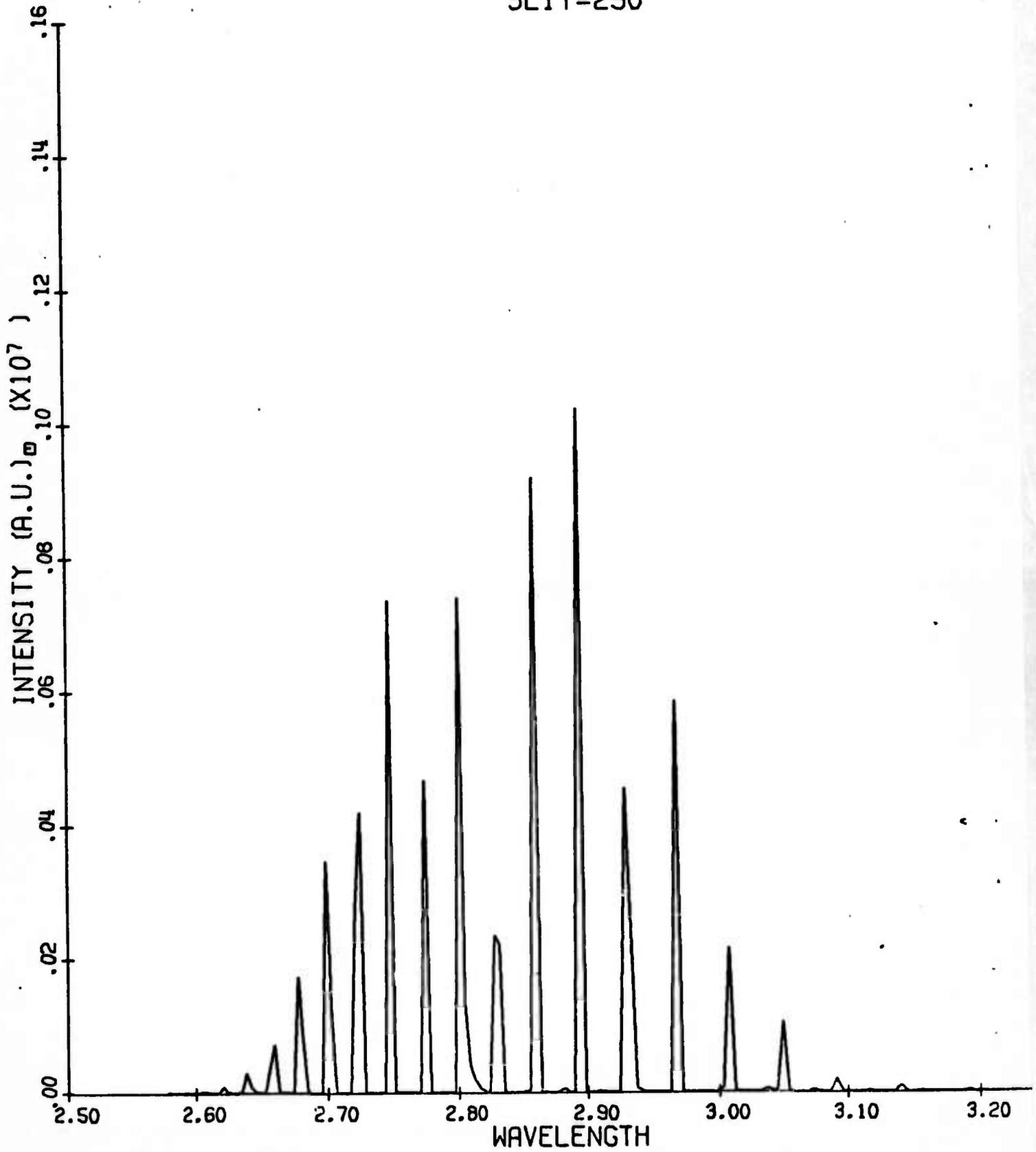

OH FUNDAMENTAL

TR= 300 TV= 300

SLIT=250

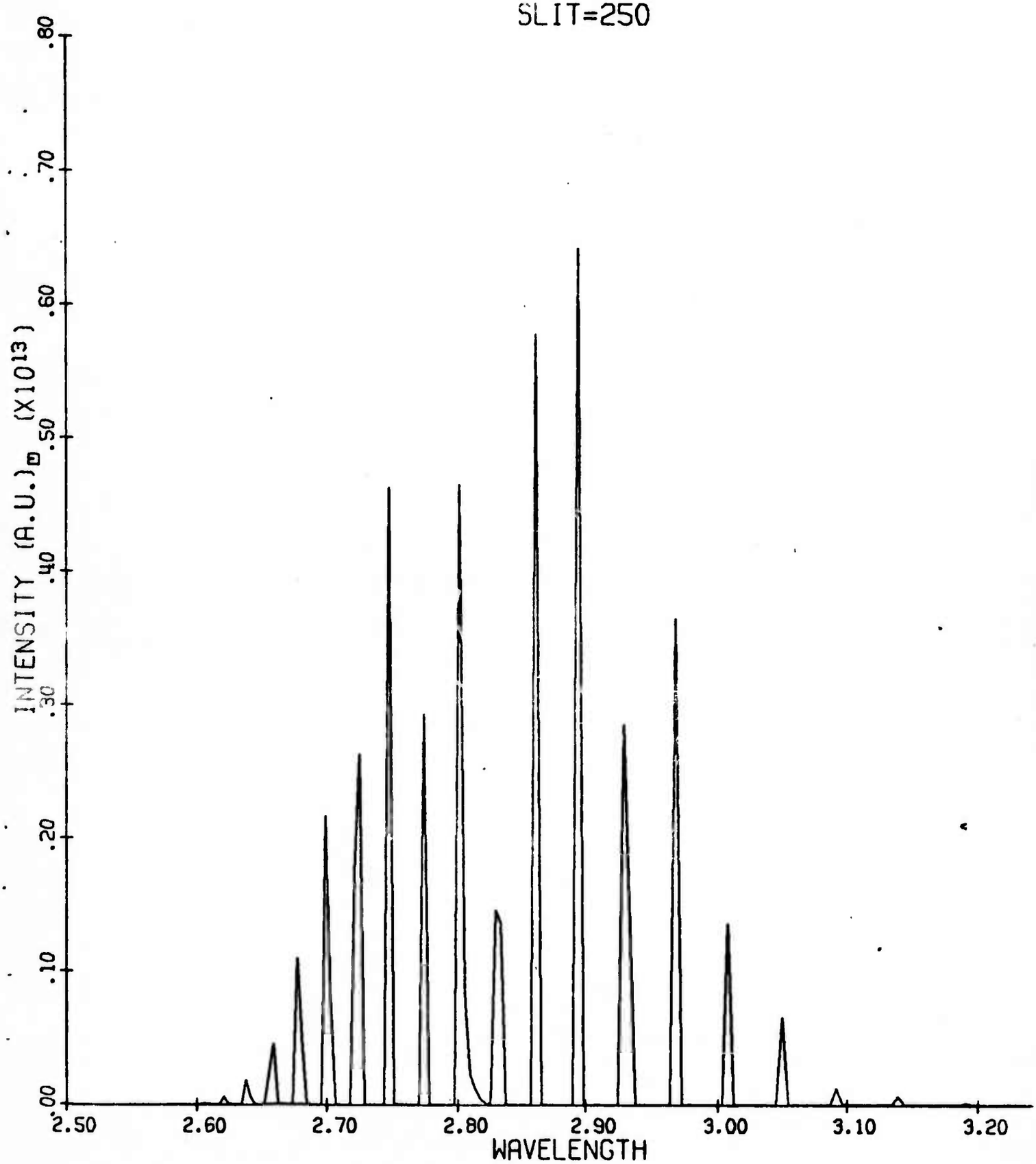

APPENDIX A

A copy of the program that generates the infrared data is contained in Appendix A.

```
      DIMENSION PN(50),TR(50,50),RE(50,50),FEL(5000),FSL(5000)
      DIMENSION FELP(5000),FSLP(5000)
      DIMENSION A(20),EN(10),TI1(20),TI2(20),SLI(8)
      KF=0
      READ(5,11) (TI1(I),I=1,4)
      READ(5,11) (TI2(I),I=1,4)
      READ(5,11) (SLI(I),I=1,2)
   11 FORMAT(6A4)
    5 READ(5,6,END=125) N,IVMAX,IV,IVP,LAMBDA
      WRITE(8,6) N,IVMAX,IV,IVP,LAMBDA
    6 FORMAT(10I4)
      READ(5,13) WE1,XE1,YE1,BE,AE
      WRITE(8,13) WE1,XE1,YE1,BE,AE
      READ(5,13) (A(I),I=1,N)
      WRITE(8,13) (A(I),I=1,N)
      READ(5,13) TE,TV,DE,S
      WRITE(8,13) TE,TV,DE,S
   13 FORMAT(8F10.4)
      CM=1.26E+14
      ILOOP=IVMAX+IVP
      ZER1=0.5*WE1-0.25*XE1+0.125*YE1
      DO 20 J=1,10
      DO 20 K=1,10
      TR(J,K)=0.
   20 RE(J,K)=0.
      EN(1)=0
      DO 40 J=1,ILOOP
      R=J-.5
   40 EN(J)=WE1*R-XE1*R**2+YE1*R**3-ZER1
      DO 50 J=1,IVMAX
      JJ=J+IVP
   50 RE(J,JJ)=EN(JJ)-EN(J)
      Q=0.
      DO 60 J=1,ILOOP
   60 Q=EXP(-EN(J)*1.43886/TV)+Q
C     SUM=-ILOOP
C     DO 70 J=1,ILOOP
C  70 SUM=SUM+J
      DO 80 J=1,ILOOP
C  80 PN(J)=CM/ILOOP
C   80 PN(J)=CM/SUM*J-CM/SUM
C     PN(J)=-CM/SUM*J+CM/SUM*ILOOP
      PN(J)=CM*EXP(-EN(J)*1.43886/TV)/Q
      PN(1)=CM/Q
C     WRITE(10,15) J,PN(J)
   15 FORMAT(I1,E10.3)
   80 CONTINUE
C     DATA A/0.,0.,0.,0.,1.,4.55,12.4,28.4,50.,104./
C     DATA A/0.,0.,0.,1.0,3.77,8.94,16.8,28.3,42.7,57.8/
```

```
C       DATA A/0.,0.,1.00,2.8,5.2,8.1,11.1,14.1,16.6,18.6/
C       DATA A/0.,1.0,1.36,1.26,.878,.39,.0474,.0753/
C       DATA A/0.,0.,1.0,3.0,5.96,9.89,14.74,20.48,27.03,34.36/
C       DATA A/0.,1.0,1.93,2.78,3.53,4.21,4.81,5.35,5.74,6.23/
        RAD=1.0
        DO 100 J=1,IVMAX
        TR(J,J+IVP)=A(J+IVP)*RAD
  100   CONTINUE
        CALL SPCTRM(TE,LAMBDA,IVMAX,IV,IVP,DE,PN,TR,RE,KF,FSL,FEL,BE,AE,S)
        GO TO 5
  125   CONTINUE
        WRITE(6,1) KF
    1   FORMAT('KF=',I4)
        WRITE(6,150) (FEL(I),FSL(I),I=1,KF)
  150   FORMAT(/,1P2E10.3)
        DO 10 I=1,KF
        II=KF+1-I
        FELP(I)=1.E+04/FEL(II)
   10   FSLP(I)=FSL(II)
C       WRITE(7,150) (FELP(I),FSLP(I),I=1,KF)
C       CALL GRAPH(FELP,FSLP,KF)
        CALL PLOT(FELP,FSLP,KF,TI1,TI2,SLI)
        STOP
        END
        SUBROUTINE SPCTRM(TE,LAMBDA,IVMAX,IV,IVP,DE,PN,TR,RE,KF,FSL,FEL,BE,AE,S
        DIMENSION SL(5000),EL(5000),WSL(500),WEL(500),PN(50),NT(100)
        DIMENSION BSL(10,5000),BEL(10,5000),TR(50,50),RE(50,50)
        DIMENSION FSL(5000),FEL(5000)
        AO=1.44/TE
        DO 100 I=IV,IVMAX
        DO 107 IS=1,1000
        SL(IS)=0.0
  107   EL(IS)=0.0
        KENT=0
        IVP1=IVP+I
        BV=BE-AE*(I-0.5)
        BVP=BE-AE*(IVP1-0.5)
        JD=-3
        A=AO*BV
        EJ1=EXP(-A)
        EJ2=EJ1*EJ1
        AQR=1.0
        QR=1.0
        JC=0
        JMAX=0
  101   JMAX=JMAX+1
        JC=JC+1
        JC2=JC+1
        DO 102 IJ=1,JC
  102   AQR=AQR*EJ1
        AQR1=AQR*JC2
    5   FORMAT(' AQR1=',1PE10.3,'JMAX=',I5)
        QR=QR+AQR1
        IF(AQR1/QR-1.E-3)103,103,101
  103   EBL=RE(I,IVP1)
        CB=PN(IVP1)*TR(I,IVP1)/QR*1.9863E-23
C       WRITE(6,2000) JMAX,EBL,CB,PN(IVP1),TR(I,IVP1)
 2000   FORMAT(' JMAX=',I4,' EBL=',E10.3,' CB=',E10.3
     1,' PN=',E10.3,' TR=',E10.3)
        DO 104 JP=1,2
```

```
      JD=JD+2
      EJ=1.0
      EFJ=1.0/EJ2
      WRITE(6,120)
  120 FORMAT(//,' WEL',8X,'WSL')
      DO 105 J=1,JMAX
      EFJ=EFJ*EJ2
      JD1=J+JD
      WEL(J)=EBL+BVP*J*(J-1)-BV*(JD1-1)*JD1
      EJ=EJ*EFJ
      JDEM=J+JD1-1
      IF(JDEM) 11,12,11
   12 SJ=0
      GO TO 13
   11 SJ=(JDEM+LAMBDA)*(JDEM-LAMBDA)
      SJ=SJ/JDEM
   13 WSL(J)=CB*WEL(J)*SJ*EJ
      WRITE(6,2005)WEL(J),WSL(J)
 2005 FORMAT(1P2E10.3)
  105 CONTINUE
      CALL AMLGMT(0.0,JMAX,WSL,WEL,SL,EL,KENT,S)
C     WRITE(7,2010) KENT
 2010 FORMAT(' KENT=',I4)
  104 CONTINUE
      IF(LAMBDA) 113,112,113
  113 EJ=1.0
      WRITE(6,120)
      EFJ=1.0/EJ2
      DO 114 J=1,JMAX
      EFJ=EFJ*EJ2
      WEL(J)=EBL+BVP*J*(J-1)-BV*J*(J-1)+(BV-BVP)*LAMBDA**2
      EJ=EJ*EFJ
      SJ=(2*J+1)*LAMBDA*LAMBDA
      SJ=SJ/(J*(J+1))
      WSL(J)=CB*WEL(J)*SJ*EJ
      WRITE(6,2005)WEL(J),WSL(J)
  114 CONTINUE
      CALL AMLGMT(0.0,JMAX,WSL,WEL,SL,EL,KENT,S)
C     WRITE(7,2010) KENT
  112 NT(I)=KENT
      DO 106 KS=1,KENT
      RSL(I,KS)=SL(KS)
      REL(I,KS)=EL(KS)
  106 CONTINUE
      WRITE(6,1)
    1 FORMAT(//,' REL',8X,'RSL')
      WRITE(6,2015) (REL(I,IJ),RSL(I,IJ),IJ=1,KENT)
 2015 FORMAT(1P2E10.3)
      CALL AMLGMT(DE,KENT,SL,EL,FSL,FEL,KF,S)
C     WRITE(6,2)
    2 FORMAT(//,' FEL',8X,'FSL')
      WRITE(6,2015) (FEL(J),FSL(J),J=1,KF)
C     WRITE(7,2020) KF
 2020 FORMAT(' KF=',I4)
  100 CONTINUE
      RETURN
      END
      SUBROUTINE AMLGMT(D,J,WS,WE,S,E,K,SL)
      DIMENSION WS(5000),WE(5000),TABE(5000),TABS(5000),S(5000),E(5000)
      J1=K
```

```
      IF(WE(J)-WE(1)) 100,101,101
  101 NW=1
      NM=J
      ND=1
      GO TO 102
  100 NW=J
      NM=1
      ND=-1
  102 IF(D) 103,103,104
  103 IF(K) 125,125,126
  125 DO 127 I=1,J
      S(I)=WS(NW)
      E(I)=WE(NW)
  127 NW=NW+ND
      K=J
      GO TO 1000
  126 JCOUNT=J+K
      IC=0
      NC=0
      KC=JCOUNT
  142 ETEST=WE(1)
      IE=1
      NC=NC+1
      DO 131 I=1,J
      IF(ETEST-WE(I)) 132,131,131
  132 IE=I
      ETEST=WE(I)
  131 CONTINUE
      DO 133 I=1,K
      IF(ETEST-E(I)) 144,133,133
  144 IE=-I
      ETEST=E(I)
  133 CONTINUE
      IF(IE) 105,105,106
  105 IE=-IE
      TABS(JCOUNT)=S(IE)
      TABE(JCOUNT)=E(IE)
      E(IE)=-E(IE)
      GO TO 107
  106 TABS(JCOUNT)=WS(IE)
      TABE(JCOUNT)=WE(IE)
      WE(IE)=-WE(IE)
  107 IF(JCOUNT-KC) 108,109,109
  108 IF(TABE(JCOUNT)-TABE(JCOUNT+1)) 109,141,109
  141 JC1=JCOUNT+1
      TABS(JC1)=TABS(JCOUNT+1)+TABS(JCOUNT)
      IC=IC-1
      GO TO 110
  109 JCOUNT=JCOUNT-1
  110 IF(KC-NC) 142,143,142
  143 K=KC+IC
      DO 145 I=1,K
      E(I)=TABE(I-IC)
  145 S(I)=TABS(I-IC)
      DO 146 I=1,J
  146 WE(I)=-WE(I)
      GO TO 1000
  104 LE=2
      IF(K) 111,111,112
  111 RN=WE(NW)/D
```

```
            N=RN
            LE=1
            EO=N*D
            ESTORE=EO
            NSTEPS= (WE(NM)-WE(NW))/D+1
            J1=NSTEPS
            EMAX=EO+NSTEPS*D
            GO TO 114
      112   IF(WE(NW)-EO)115,113,113
      115   N=N-1
            EO=EO-D
            NSTEPS=NSTEPS+1
            ESTORE=EO
            GO TO 112
      113   IF(WE(NM)-EMAX)114,114,116
      116   NSTEPS=NSTEPS+1
            EMAX=EMAX+D
            GO TO 113
      114   DO 117 IE=1,NSTEPS
            TABE(IE)=ESTORE
            TABS(IE)=0.0
            TAS=TABS(IE)
            CALL SLIT(WE,WS,TAS,ESTORE,J,SL)
            TABS(IE)=TAS
            GO TO(119,120),LE
      120   DO 135 JE=1,J1
            IF(E(JE)-ESTORE)135,137,135
      137   TABS(IE)=TABS(IE)+S(JE)
            GO TO 119
      135   CONTINUE
      C     WRITE(6,1)ESTORE,IE
          1 FORMAT(/' ESTORE=',E15.8,'   IE=',I4)
      C     WRITE(6,2)
          2 FORMAT(' E(JE)')
      C     WRITE(6,3)(E(JE),JE=1,NSTEPS)
          3 FORMAT(1X,E15.8)
      119   ESTORE=ESTORE+D
      117   CONTINUE
            ESTORE=EO
            DO 121 IE=1,NSTEPS
            E(IE)=TABE(IE)
      121   S(IE)=TABS(IE)
            K=NSTEPS
     1000   RETURN
            END
            SUBROUTINE SLIT(TE,TS,TSUM,ESTORE,NENT,SL)
            DIMENSION TE(5000),TS(5000)
            WRITE(10,10)ESTORE
         10 FORMAT(E10.3)
            SLT=SL/1000.*13.2E-7
            DLAM=SLT*ESTORE*ESTORE
            DO 100 I=1,NENT
            SFUN=0.
            A=ABS(ESTORE-TE(I))
            IF(A.LE.DLAM) SFUN=1-A/DLAM
      C     X=(ESTORE-TE(I))*(ESTORE-TE(I))
      C     IF(ABS(X).GT.93.54) GO TO 99
      C     SFUN=EXP(-X/380)
      C     TSUM=TSUM+SFUN*TS(I)
      C     GO TO 100
```

```
      C   99 SFUN=10.0E-10
             TSUM=TSUM+SFUN*TS(I)
         100 CONTINUE
             RETURN
             END
             SUBROUTINE PLOT(FEL,FSL,KF,TI1,TI2,SLI)
             DIMENSION FEL(5000),FSL(5000),TI1(20),TI2(20),SLI(8)
             CALL PLTSIZ(1.0)
      C      XMIN=2.50
      C      DX=0.1
.5           CALL PSCALE(8.0,1.0,XMIN,DX,FEL(1),KF,1)
             CALL PSCALE(8.0,1.0,YMIN,DY,FSL(1),KF,1)
             CALL PLTOFS(XMIN,DX,YMIN,DY,1.0,1.0)
             CALL PAXIS(1.0,1.0,' WAVELENGTH ',-13,8.0,0.0,XMIN,DX,1.0)
             CALL PAXIS(1.0,1.0,'INTENSITY (A.U.)',17,8.0,90.0,YMIN,DY,1.0)
             CALL PLINF(FEL(1),FSL(1),KF,1,0,0,1)
             CL=PSYMLN(0.2,16)
             CALL PSYMB(5.0-CL/2.0,10.0,0.2,TI1(1),0.0,16)
.5           CALL PSYMB(5.0-PSYMLN(0.15,16)/2.,9.5,0.15,TI2(1),0.0,16)
             CALL PSYMB(5.0-PSYMLN(0.15,8)/2.0,9.1,0.15,SLI(1),0.0,8)
             CALL PLTEND
             RETURN
             END
 FILE
```

PART III Vibrational Relaxation in a Core Flow Field

Edward R. Fisher

Introduction

This report presents the results of vibrational relaxation in a core flow field of a rocket engine. Of particular interest is the extent of vibrational freezing in a set of combustion products undergoing rapid expansion. The relaxation model used has been presented elsewhere[1] but generally includes vibration-translation (VT) and vibration-vibration (VV) energy transfer processes coupling together H_2, N_2, CO, OH, five modes of H_2O (100,010,020,001, and 000) and eight modes of CO_2 (100,010,020,030, 001,101,021, and 000). The model, termed the "Berkeley" model after its site of development, contains reactions including O and H which are not present in this flow field and state of the art rate coefficient data.

The flow field used in this calculation is modeled after the core flow field of a TITAN II rocket engine. The eight representative streamlines were supplied by Boynton[2] and feature an LTE assumption at the nozzle exit plane and include the effects of film cooling. This latter effect produces fuel product enrichment (H_2, CO and CO_2) in the outermost streamlines as a result of the fuel rich flow used to cool the surface of the exit nozzle.

The calculation presented here uncouples the energy transfer chemistry from the flow field. This assumption is generally justified since the heat capacity of the flow gases is only weakly dependent on the extent of vibrational freezing of the diatomic species present in the flow (vida infra). The general conclusions evident from this relaxation calculation are:

a) The diatomic species tend to freeze out early in the expansion; near exit conditions (900°K) for the outermost streamlines while somewhat lower for the more dense inner streamlines.

b) In the outermost streamline, all modes tend to freeze near the nozzle exit condition,

c) The bending modes of H_2O and CO_2 tend to remain in LTE with the flow for all except the outermost streamline.

d) The presence of vibrationally frozen N_2 causes $CO_2(001)$ to be above LTE conditions due to the rapid VV coupling which in turn causes $CO_2(101)$ to be above LTE conditions.

e) Vibrationally excited H_2 is predicted throughout the core flow field but it is not yet clear what effect this will have on mixing layer chemistry.

The following sections present the details of the calculation and the substance behind the conclusions.

Flow Field

The core flow field was obtained from a calculation of Boynton[2] using the MULTITUBE program. The calculation used as initial conditions nonuniform exit plane conditions calculated by Aerospace[2] which encorporated both film cooling and nozzle contour effects. An inviscid vacuum expansion from these nonuniform exit conditions was performed on the MULTITUBE code.[3] The specific temperature and pressure histories on eight streamlines across the vacuum expansion are shown in Figures 1 and 2. Several features should be noted in these streamlines. The centerline streamline shows recompression as a result of the nozzle contour followed by a rapid expansion region. The outermost streamline shows the most rapid expansion, but, of course, represents the smallest flow mass fraction. And the variation in the exit plane temperature across the nozzle plane is clearly demonstrated. This latter effect is a result of combustion heating leading to increased

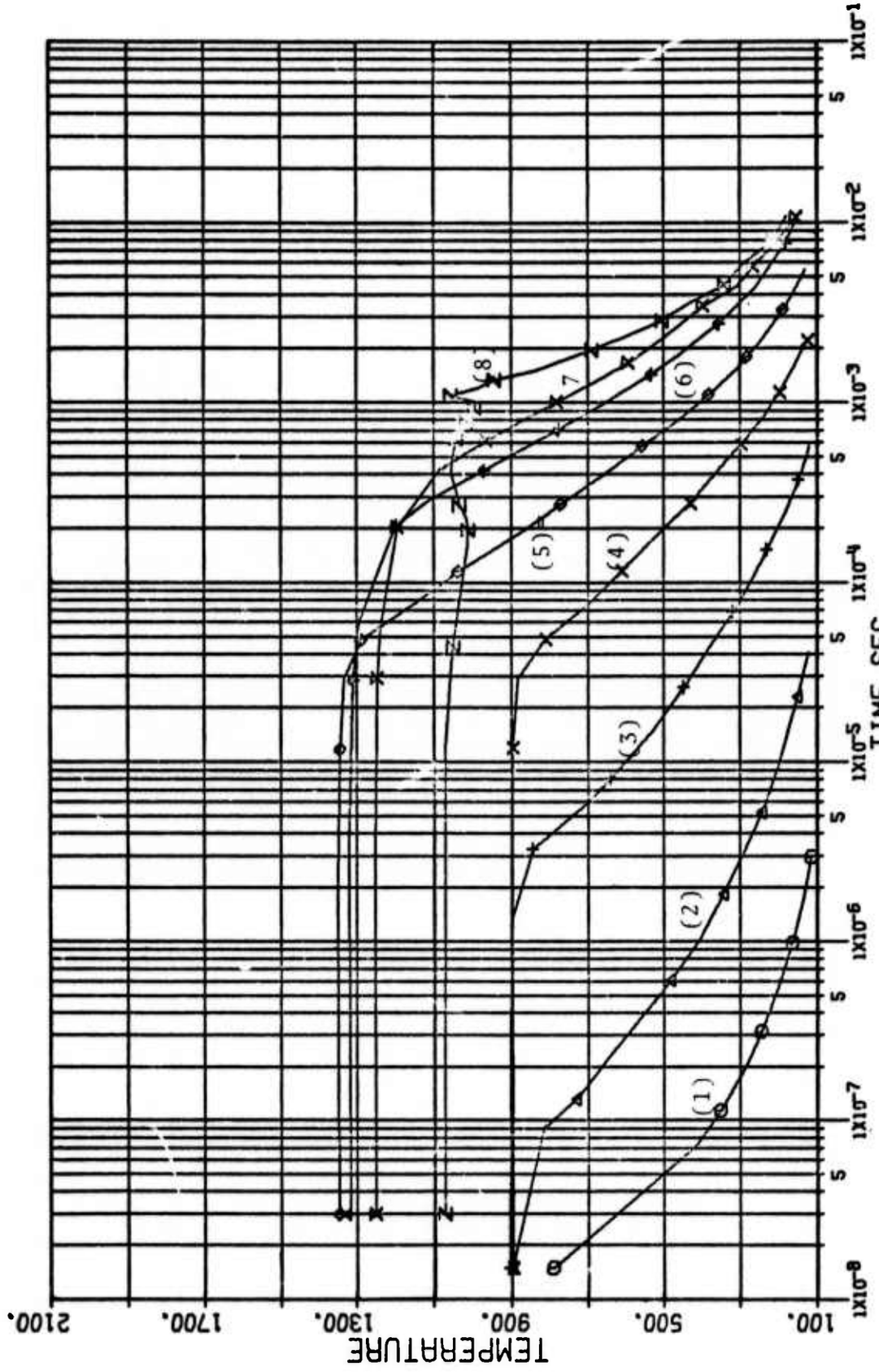

Figure 1: Temperature streamlines for the Core Flow Field.

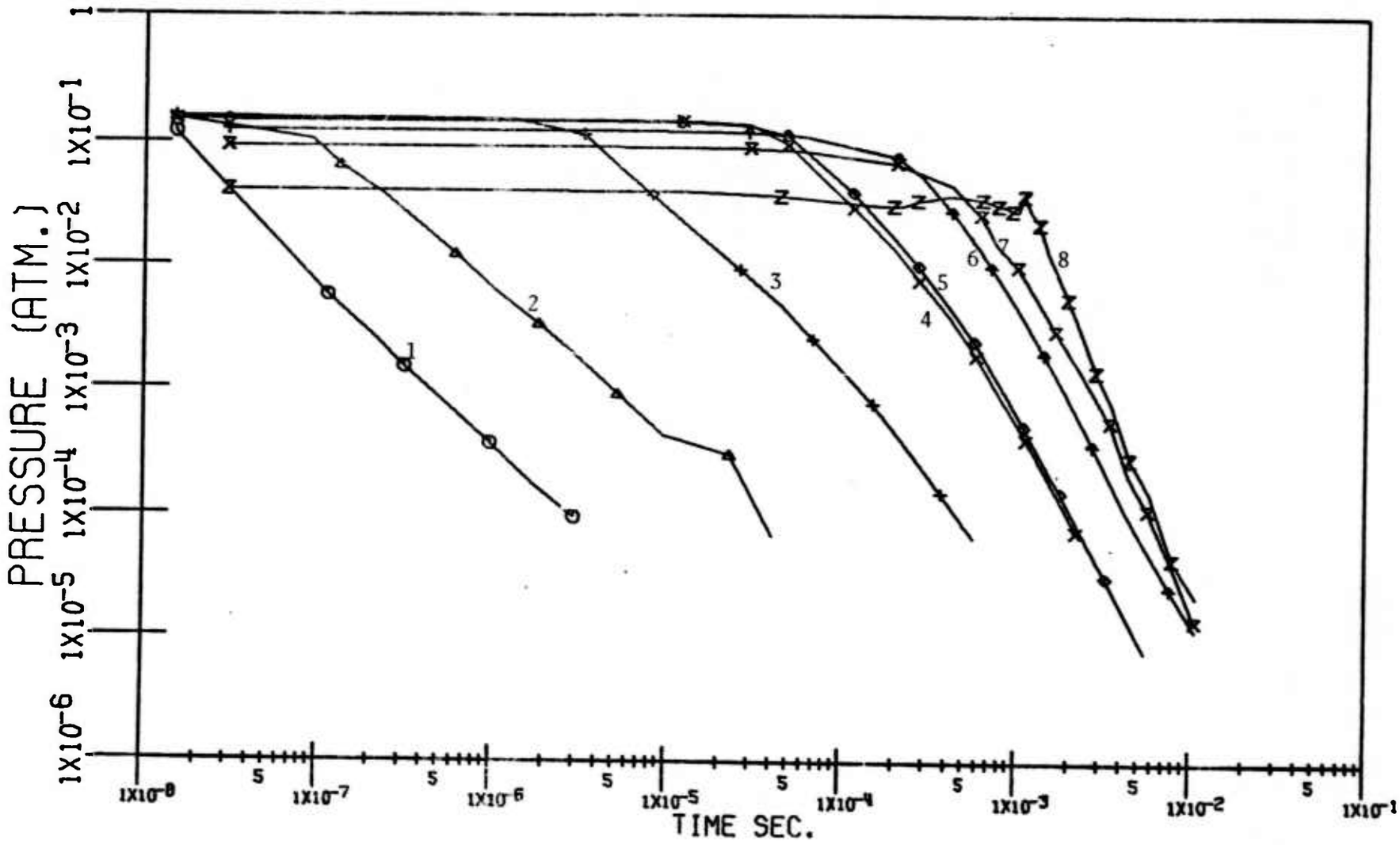

Figure 2: Pressure streamlines for the Core Flow Field.

temperatures and film coolant, e.g. uncombusted flows, near the nozzle walls.

Table I lists the exit plane concentrations used in these relaxation calculations. As expected, fuel rich species are present in higher concentrations in the outermost streamlines as a result of the film coolants. This variation in composition across the exit plane enhances the possibility of having vibrationally excited hydrogen entering the mixing layer region of the flow.

Relaxation Model

The energy transfer model used in these relaxation calculations include vibration-vibration and vibration-rotation-translation processes for the major vibrational modes of H_2, N_2, CO, H_2O and CO_2. Table II gives the vibrational levels included in the model together with the energy spacing.

The rate coefficients used in these calculations have been derived from several sources. Primarily, experimental values are used where possible but the large number of potentially important energy transfer processes necessitate that estimates be made for those processes for which no experimental values are available. Table III details the energy transfer processes included in the model together with the references regarding the rate coefficient value. Further details of the energy transfer processes and rate coefficient estimates can be found elsewhere.(1)

Several features of the relaxation model should be indicated. First, the number of vibrational levels included in the polyatomics, i.e. H_2O and CO_2, are fairly large. This is primarily a result of interest in vibrational levels of the polyatomics which give rise to 2.7μ radiation, i.e. $CO_2(021)$ $CO_2(101)$ and $H_2O(001)$. Secondly, only one vibrational level is included in

Table I

Exit Plane Mole Fractions

Species	Streamlines 1-4	Streamlines 5-8
H_2	0.04	0.22
H_2O	0.47	0.33
CO	0.03	0.10
N_2	0.36	0.32
NO	0.009	0.0001
CO_2	0.094	0.13

Table II

Vibrational Levels Included in Relaxation Model

Levels	Energy Spacing (cm^{-1})
$H_2(1)$	4159.2
$N_2(1)$	2330.7
OH(1)	3569.6
CO(1)	2143.3
$H_2O(010)$	1595.0
$H_2O(020)$	3151.4
$H_2O(100)$	3651.7
$H_2O(001)$	3755.8
$CO_2(010)$	667.3
$CO_2(020)$	1285.5
$CO_2(030)$	1932.5
$CO_2(100)$	1388.3
$CO_2(001)$	2349.3
$CO_2(021)$	3609
$CO_2(101)$	3716

TABLE III

(2) RELAXATION MODEL

Vibration-Translation Processes	Reference	Rate Constant (cc/molecule-sec)
1) $H_2(v=1) + H \rightarrow H_2 + H$	(a)	$3.2^{-11} \exp(-1400/T)$
2) $H_2(v=1) + O \rightarrow H_2 + O$	(b)	$3.0^{-13} \sqrt{T}$
3) $H_2(v=1) + H_2 \rightarrow H_2 + H_2$	(c,d)	$1.5^{-7} \exp(-139/T^{1/3})$
4) $H_2(v=1) + H_2O \rightarrow H_2 + H_2O$	(b,e)	$1.5^{-7} \exp(-139/T^{1/3})$
5) $N_2(v=1) + H \rightarrow N_2 + H$	(y)	$1.9^{-6} \exp(-164/T^{1/3})$
6) $N_2(v=1) + O \rightarrow N_2 + O$	(f,g,h)	$1.2^{-13} \exp(-23/T^{1/3})$
7) $N_2(v=1) + H_2 \rightarrow N_2 + H_2$	(i)	$3.9^{-8} \exp(-164/T^{1/3})$
8) $N_2(v=1) + H_2O \rightarrow N_2 + H_2O$	(b,e)	$3.9^{-8} \exp(-164/T^{1/3})$
9) $OH(v=1) + H \rightarrow OH + H$	(b)	3^{-11}
10) $OH(v=1) + O \rightarrow OH + O$	(b)	3^{-11}
11) $OH(v=1) + H_2 \rightarrow OH + H_2$	(b)	1^{-11}
12) $OH(v=1) + H_2O \rightarrow OH + H_2O$	(b)	3^{-12}
13) $H_2O(010) + H \rightarrow H_2O(000) + H$	(b)	1^{-11}
14) $H_2O(010) + O \rightarrow H_2O(000) + O$	(b)	1^{-11}
15) $H_2O(010) + H_2 \rightarrow H_2O(000) + H_2$	(b,j)	1^{-11}
16) $H_2O(010) + H_2O \rightarrow H_2O(000) + H_2O$	(k)	1^{-11}
17) $H_2O(001) + H \rightarrow H_2O(000) + H$	(b)	1^{-11}
18) $H_2O(001) + O \rightarrow H_2O(000) + O$	(b)	1^{-11}
19) $H_2O(001) + H_2 \rightarrow H_2O(000) + H_2$	(j)	2^{-13}
20) $H_2O(001) + H_2O \rightarrow H_2O(000) + H_2O$	(l)	1^{-12}

21)	$H_2O(001) + H \rightarrow H_2O(020) + H$	(b)	1^{-11}
22)	$H_2O(001) + O \rightarrow H_2O(020) + O$	(b)	1^{-11}
23)	$H_2O(001) + H_2 \rightarrow H_2O(020) + H_2$	(b)	1^{-11}
24)	$H_2O(001) + H_2O \rightarrow H_2O(020) + H_2O$	(b)	1^{-11}
25)	$CO(v=1) + H \rightarrow CO(v=0) + H$	(o)	$5.3^{-7} \exp(-119/T^{1/3})$
26)	$CO(v=1) + O \rightarrow CO(v=0) + O$	(p)	$1^{-8} \exp(-96/T^{1/3})$
27)	$CO(v=1) + H_2 \rightarrow CO(v=0) + H_2$	(q)	$9^{-9} \exp(-119/T^{1/3})$
28)	$CO(v=1) + H_2O \rightarrow CO(v=0) + H_2O$	(b)	$9^{-9} \exp(-119/T^{1/3})$
29)	$CO_2(010) + H \rightarrow CO_2(000) + H$	(b)	$3.8^{-12} \exp(-7/T^{1/3})$
30)	$CO_2(010) + O \rightarrow CO_2(000) + O$	(p)	$2.3^{-9} \exp(-77/T^{1/3})$
31)	$CO_2(010) + H_2 \rightarrow CO_2(000) + H_2$	(r)	$7.6^{-12} \exp(-7/T^{1/3})$
32)	$CO_2(010) + H_2O \rightarrow CO_2(000) + H_2O$	(s)	1^{-11}
33)	$CO_2(010) + CO_2 \rightarrow CO_2(000) + CO_2$	(r)	$4.6^{-10} \exp(-77/T^{1/3})$
34)	$CO_2(001) + H \rightarrow CO_2(000) + H$	(t)	$6.7^{-8} \exp(-208/T^{1/3})$
35)	$CO_2(001) + O \rightarrow CO_2(000) + O$	(t)	$1^{-8} \exp(-96/T^{1/3})$
36)	$CO_2(001) + H_2 \rightarrow CO_2(000) + H_2$	(t)	$9^{-9} \exp(-119/T^{1/3})$
37)	$CO_2(001) + H_2O \rightarrow CO_2(000) + H_2O$	(t)	$9^{-9} \exp(-119/T^{1/3})$
38)	$CO_2(001) + H \rightarrow CO_2(030) + H$	(b)	$2.13^{17} T^{-6.34} \exp(-3013/T - 378.7/T^{1/3} + 1416/T^{2/3})$
39)	$CO_2(001) + O \rightarrow CO_2(030) + O$	(u)	$4.6^{24} T^{-5.89} \exp(-4223/T - 672.7/T^{1/3} + 2683/T^{2/3})$
40)	$CO_2(001) + H_2 \rightarrow CO_2(030) + H_2$	(v)	$4.27^{17} T^{-6.34} \exp(-3013/T - 378.7/T^{1/3} + 1416/T^{2/3})$

41) $CO_2(001) + H_2O \rightarrow CO_2(030) + H_2O$ (v) $4.71^{-40} T^{4.54} \exp(2081/T + 454/T^{1/3} - 1729/T^{2/3})$

42) $CO_2(001) + CO_2 \rightarrow CO_2(030) + CO_2$ (v) $9.16^{23} T^{-5.89} \exp(-4223/T - 672.7/T^{1/3} + 2683/T^{2/3})$

43) $CO_2(001) + CO \rightarrow CO_2(030) + CO$ (v) $6.87^{23} T^{-5.89} \exp(-4223/T - 672.7/T^{1/3} + 2683/T^{2/3})$

44) $CO_2(001) + N_2 \rightarrow CO_2(030) + N_2$ (v) $6.87^{23} T^{-5.89} \exp(-4223/T - 672.7/T^{1/3} + 2683/T^{2/3})$

Vibration-Vibration Processes

45) $H_2(v=1) + H_2O(000) \rightarrow H_2(v=0) + H_2O(001)$ (m) $2.5^{-14} T^{5/6} \exp(-30.1/T^{1/3})$

46) $H_2(v=1) + OH(v=0) \rightarrow H_2(v=0) + OH(v=1)$ (b) 1^{-12}

47) $N_2(v=1) + H_2O(010) \rightarrow N_2(v=0) + H_2O(001)$ (b) 3^{-13}

48) $N_2(v=1) + H_2O(000) \rightarrow N_2(v=0) + H_2O(010)$ (n) $9.4^{-11} \exp(-64/T^{1/3})$

49) $H_2O(010) + H_2O(010) \rightarrow H_2O(020) + H_2O(000)$ (b) $1^{-12} \sqrt{T}$

50) $CO_2(001) + H_2O(000) \rightarrow CO_2(010) + H_2O(010)$ (b) 1^{-13}

51) $N_2(v=1) + CO_2(000) \rightarrow N_2(v=0) + CO_2(001)$ (r) Take the largest value $\begin{cases} 1.71^{-6}\exp(-175.3/T^{1/3}) \\ 6.07^{-14}\exp(15.3/T^{1/3}) \end{cases}$

52) $N_2(v=1) + CO(v=0) \rightarrow N_2(v=0) + CO(v=1)$ (v) Take the largest value $\begin{cases} 1.78^{-6}\exp(-210/T^{1/3}) \\ 6.98^{-13}\exp(-25.6/T^{1/3}) \end{cases}$

53) $CO_2(001) + CO(v=0) \rightarrow CO_2(000) + CO(v=1)$ (b) $1.56^{-11}\exp(-30.1/T^{1/3})$

54) $CO_2(101) + H_2O(000) \rightarrow CO_2(000) + H_2O(001)$ (b) $2^{-13}\sqrt{T}$

55) $CO_2(021) + H_2O(000) \rightarrow CO_2(000) + H_2O(001)$ (b) $2^{-13}\sqrt{T}$

56) $CO_2(101) + CO_2(000) \rightarrow CO_2(100) + CO_2(001)$ (b) $2^{-11}\sqrt{T}$

57) $CO_2(020) + CO_2(000) \rightarrow CO_2(010) + CO_2(010)$ (b) $4^{-13}\sqrt{T}$

58) $H_2O(020) + H \rightarrow H_2O(010) + H$ (w) 2^{-11}

59) $H_2O(020) + O \rightarrow H_2O(010) + O$ (w) 2^{-11}

60) $H_2O(020) + H_2 \rightarrow H_2O(010) + H_2$ (w) 2^{-11}

61) $H_2O(020) + H_2O \rightarrow H_2O(010) + H_2O$ (w) 2^{-11}

62) $CO_2(020) + H \rightarrow CO_2(010) + H$ (w) $7.6^{-12}\exp(-7/T^{1/3})$

63) $CO_2(020) + O \rightarrow CO_2(010) + O$ (w) $4.6^{-9}\exp(-77/T^{1/3})$

64) $CO_2(020) + H_2 \rightarrow CO_2(010) + H_2$ (w) $1.5^{-11}\exp(-7/T^{1/3})$

65) $CO_2(020) + H_2O \rightarrow CO_2(010) + H_2O$ (w) 2^{-11}

66) $CO_2(020) + CO_2 \rightarrow CO_2(010) + CO_2$ (w) $9.2^{-10} \exp(-77/T^{1/3})$

67) $CO_2(030) + H \rightarrow CO_2(020) + H$ (w) $1.2^{-11} \exp(-7/T^{1/3})$

68) $CO_2(030) + O \rightarrow CO_2(020) + O$ (w) $6.9^{-9} \exp(-77/T^{1/3})$

69) $CO_2(030) + H_2 \rightarrow CO_2(020) + H_2$ (w) $2.3^{-11} \exp(-7/T^{1/3})$

70) $CO_2(030) + H_2O \rightarrow CO_2(020) + H_2O$ (w) 3^{-11}

71) $CO_2(030) + CO_2 \rightarrow CO_2(020) + CO_2$ (w) $1.4^{-9} \exp(-77/T^{1/3})$

72) $H_2O(100)$ and $H_2O(001)$ assumed in quasi-equilibrium at the local translational temeprature.

73) $CO_2(100) + M \rightarrow CO_2(020) + M$ (x) 1^{-10}

References (Vibrational Relaxation Model)

(a) R.F. Hiedner and V.V. Casper, Chem. Phys. letters 15, 179(1972).

(b) estimate

(c) J.H. Kieffer and R.W. Lutz, J. Chem. Phys. 44, 658 (1966); 45, 3888(1966).

(d) C. Joffrin, J. Ducuing and J.P. Coffinet, Opt, Commun. 2, 245(1970).

(e) past measurements involving water presumably measure both VV and VT processes.

(f) W.D. Breshears and P.F. Bird, J. Chem. Phys. 48, 4768 (1968).

(g) R.J. McNeal, M.E. Whitson Jr. and G.R. Cook, preprint of work submitted to Chem. Phys. Letters (1972). Aerospace Report SPL 3303, July(1972).

(h) D.J. Eckstrom, Stanford Research Institute, unpublished results.

(i) D.R. White, J. Chem. Phys. 46, 2016(1967).

(j) estimate based on Marriott's cross section values see E.R. Fisher, AFCRL Special Report, 72-0539, August (1972).

(k) estimate based on all available data

(l) estimate based on analogy to HF VT relaxation

(m) estimate based on the modified Rapp model, J. Chem. Phys. 40, 573(1964) Fisher unpublished results.

(n) estimate based on data of C.W. Von Rosenberg, K.N.C. Bray and N.H. Pratt, J. Chem. Phys. 56, 3230(1972) and 13th Symp. (Intern.) on combustion p. 89, (1971).

(o) C.N. Rosenberg, R. Taylor and D. Teare, J. Chem. Phys. 54, 1974(1971). Also assuming the $CO_2 + H_2$ activation energy, as shown in reaction 27).

(p) unpublished data from AVCO.

(q) W. J. Hocher and R. C. Millikan, J. Chem. Phys. 38, 214 (1963); and R. C. Millikan, J. Chem. Phys. 38, 2855 (1963).

(r) R. Taylor and S. Bitterman, Rev. Mod. Phys. 41, 26 (1969).

(s) M.I. Buckwald and S. H. Bauer, J. Phys. Chem. 76, 3108 (1972).

(t) since direct VT relaxation of $CO_2(\nu_3)$ to ground state has not been unambiguously determined withoug competing VV processes, $CO_2(\nu_3)$ was assumed to relax like CO(v=1).

(u) estimate based on analogy with reaction 35).

(v) estimate based on AVCO suggestion.

(w) scaled from the analogous rate constant for exciting the lowest bending mode.

(x) the Fermi resonance in CO_2 is assumed to couple the (100) and (020) modes with a gas kinetic efficiency independent of collision partner.

(y) estimated based on the rate for CO + H, under (o) above.

(5) RADIATIVE LIFETIMES

SPECIES	t(sec)
OH(v=1)	0.3
$H_2O(100)$	0.14
$H_2O(010)$	0.045
$H_2O(001)$	0.014
$H_2O(020)$	0.022
$CO_2(010)$	0.33
$CO_2(001)$	0.0025
$CO_2(101)$	0.091

the diatomic species due to a general lack of rate coefficient data. As well, this model is not interested in anharmonic vibration-vibration effects[4] which further justifies the inclusion of only one diatomic vibrational level. Due to the Fermi resonance between the 100 and 001 levels of H_2O, the relaxation model assumes a quasi-equilibrium between these levels at the local thermodynamic temperature. Lastly, radiation losses are included in the model although for the streamlines considered here these losses are small.

Results and Discussion

The results of relaxation calculations on the eight streamliners are shown in Figures 3 (centerline) through Figure 10(outermost streamline). The vibrational populations are given in terms of a vibrational temperature defined through

$$\frac{N_i}{N_o} = e^{-\varepsilon_i/kT_v}$$

where N_i and N_o are the density of the i^{th} level and lowest level density, respectively, ε_i is the energy of the $i^{\underline{N}}$ level and T_v is the vibrational temperature. As expected from the temperature and pressure profiles of Figures 1 and 2, the outermost streamline shows the most vibrational freezing. The expansion is sufficiently rapid along this streamline (Figure 10) that essentially all molecules freeze near the exit conditions. For streamlines that are progressively closer to centerline, the bending modes of CO_2 and H_2O begin to equilibrate with the rapidly decaying translational temperature but diatomic molecules continue to freeze at vibrational temperatures only slightly below exit temperatures.

The general features of the relaxation process are evident from the Figures. Except in the outermost streamlines where the expansion process is very rapid, the bending modes remain near local thermodynamic equilibrium (LTE). The stretching modes of CO_2 and H_2O generally remain slightly above LTE values while the diatomic modes remain frozen at the highest values. The extent of vibrational freezing is small along the centerline streamline where the density and temperature are relatively high.

The important energy transfer processes which control the relaxation processes are evident from a review of the rates. Table IV presents

Legion for Figures 3 through 10

Symbol	Species
	TE
	H_2^*
	N_{2*}
X	CO^*
	OH^*
	$H_2O(100)$
	$H_2O(010)$
Z	$H_2O(020)$
Y	$H_2O(001)$
	$CO_2(100)$
	$CO_2(010)$
	$CO_2(020)$
I	$CO_3(030)$
	$CO_2(001)$
"NS".	$CO_2(101)$
	$CO_2(021)$

Figure 3

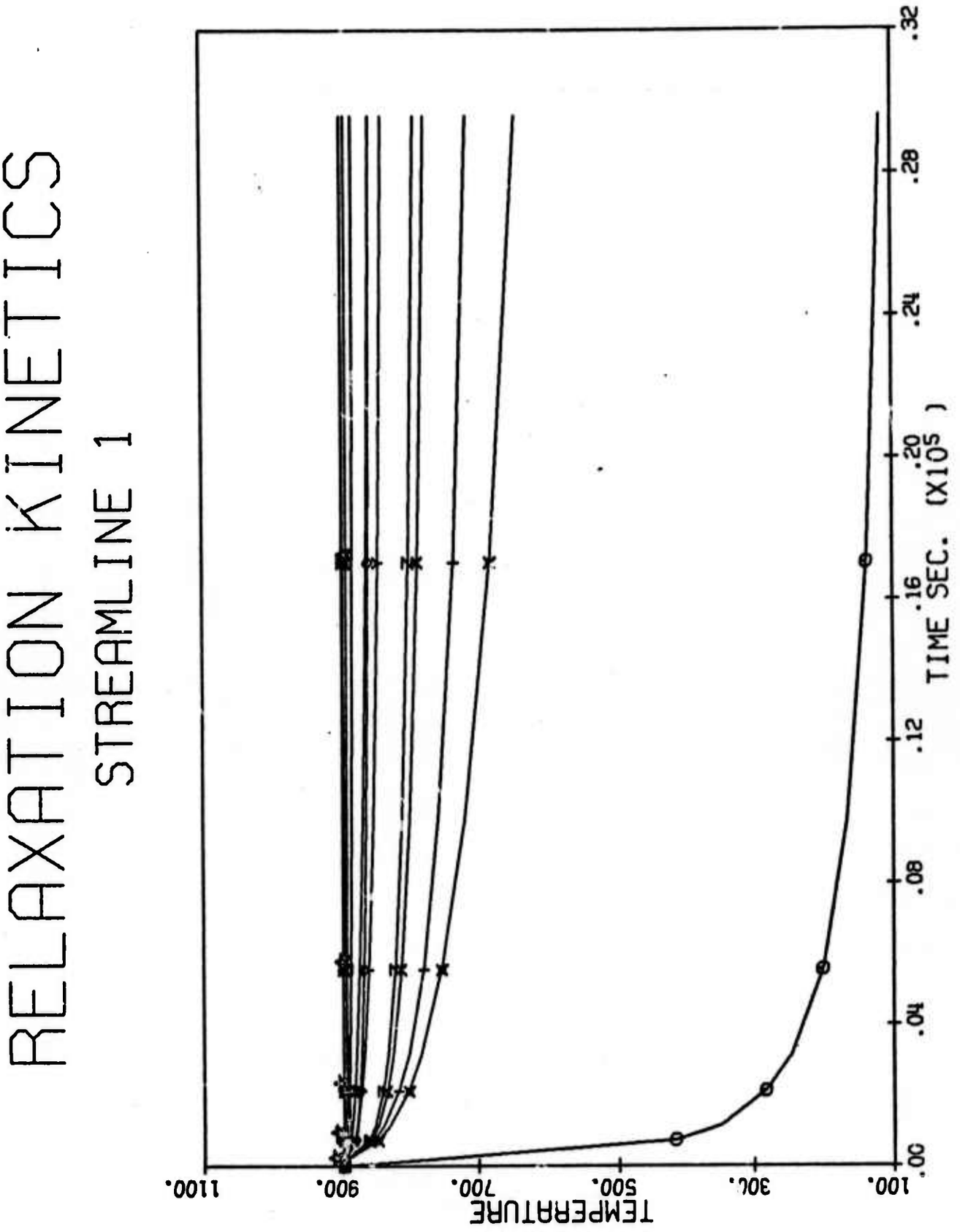
RELAXATION KINETICS
STREAMLINE 1
TEMPERATURE
100.
300.
500.
700.
900.
1100.
TIME SEC. (X10^5)
.00
.04
.08
.12
.16
.20
.24
.28
.32

Figure 4

RELAXATION KINETICS

STREAMLINE 2

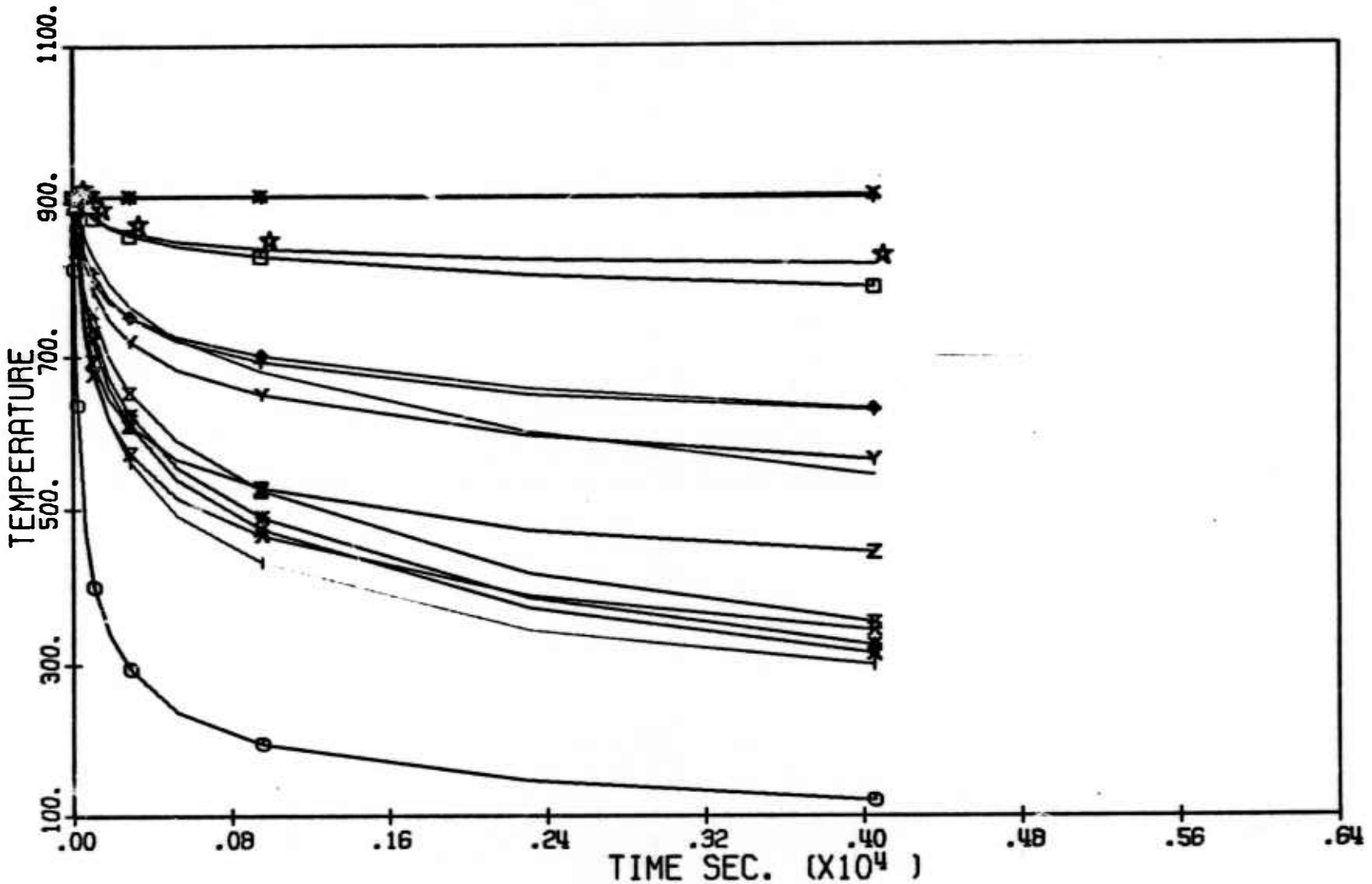

Figure 5

RELAXATION KINETICS

STREAMLINE 3

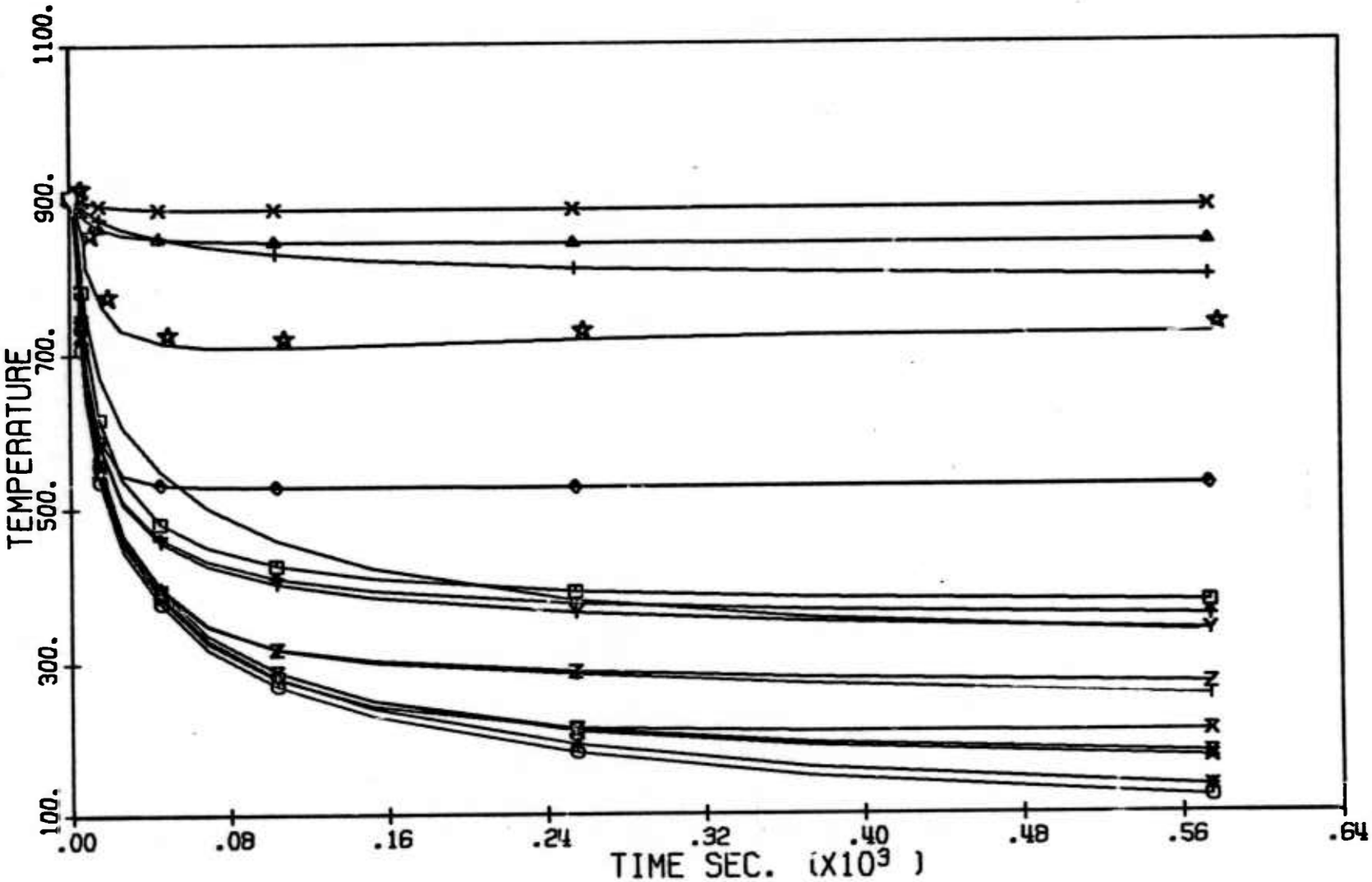

Figure 6

RELAXATION KINETICS

STREAMLINE 4

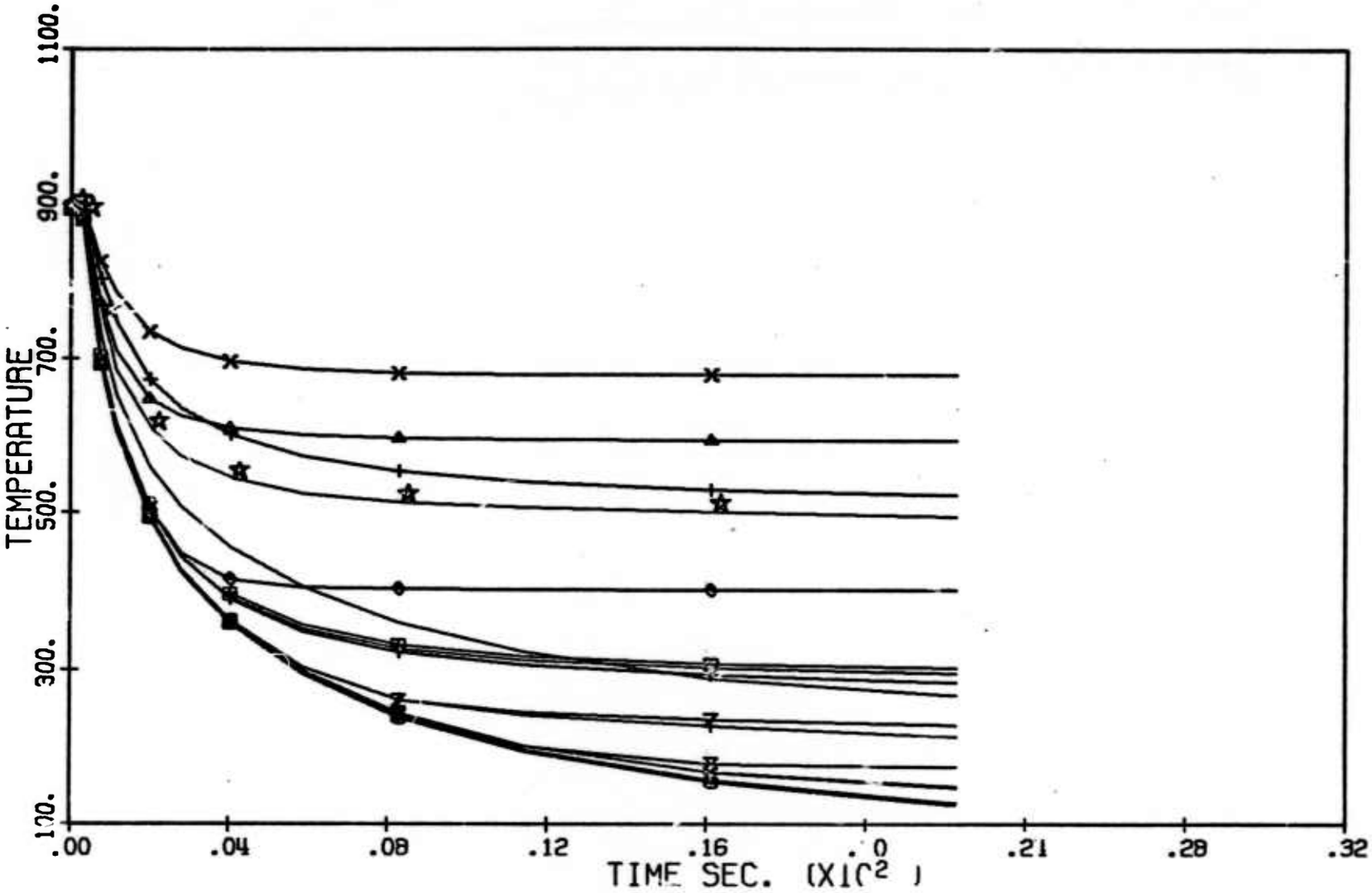

Figure 7

RELAXATION KINETICS

STREAMLINE 5

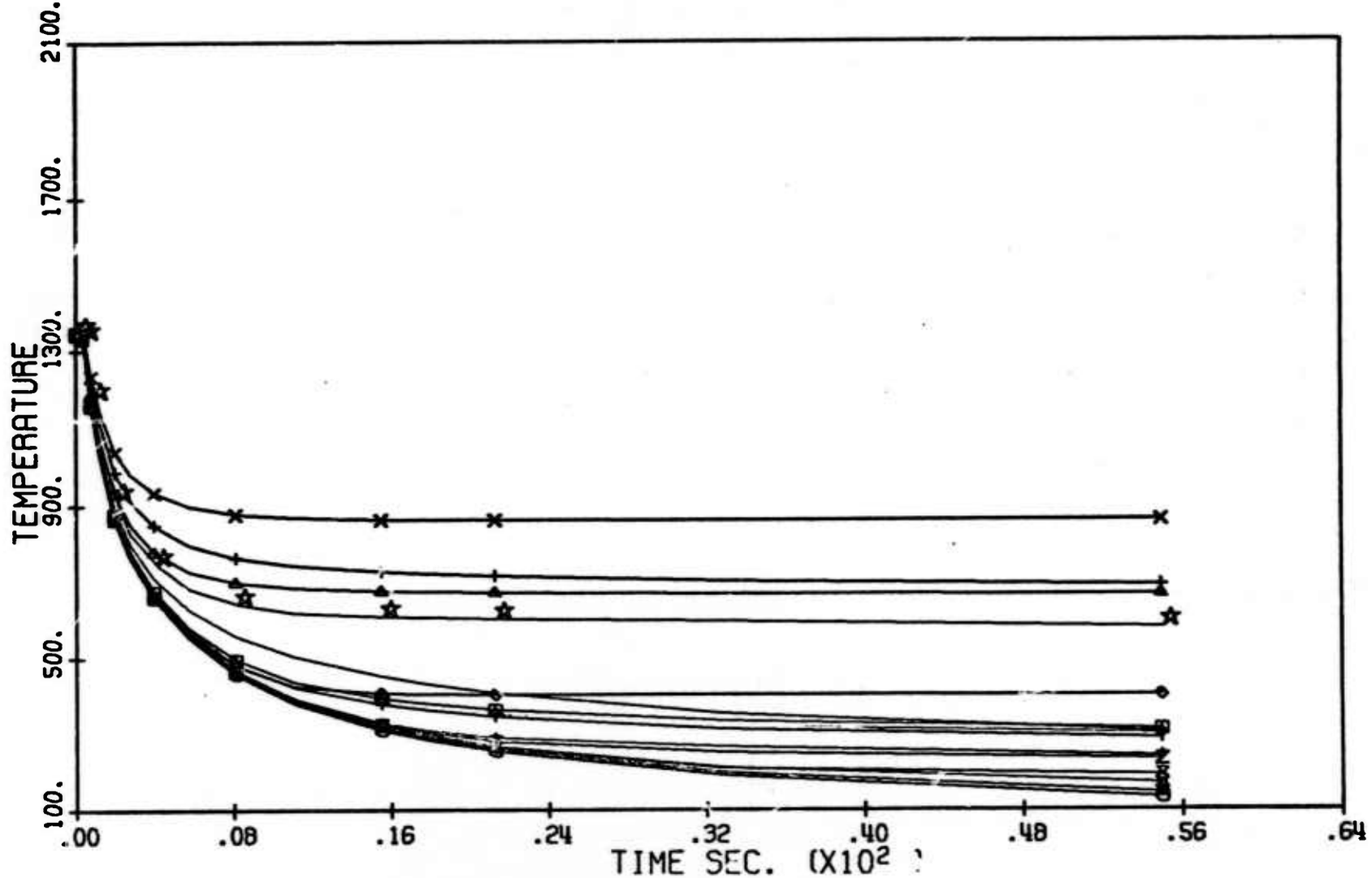

Figure 8

RELAXATION KINETICS

STREAMLINE 6

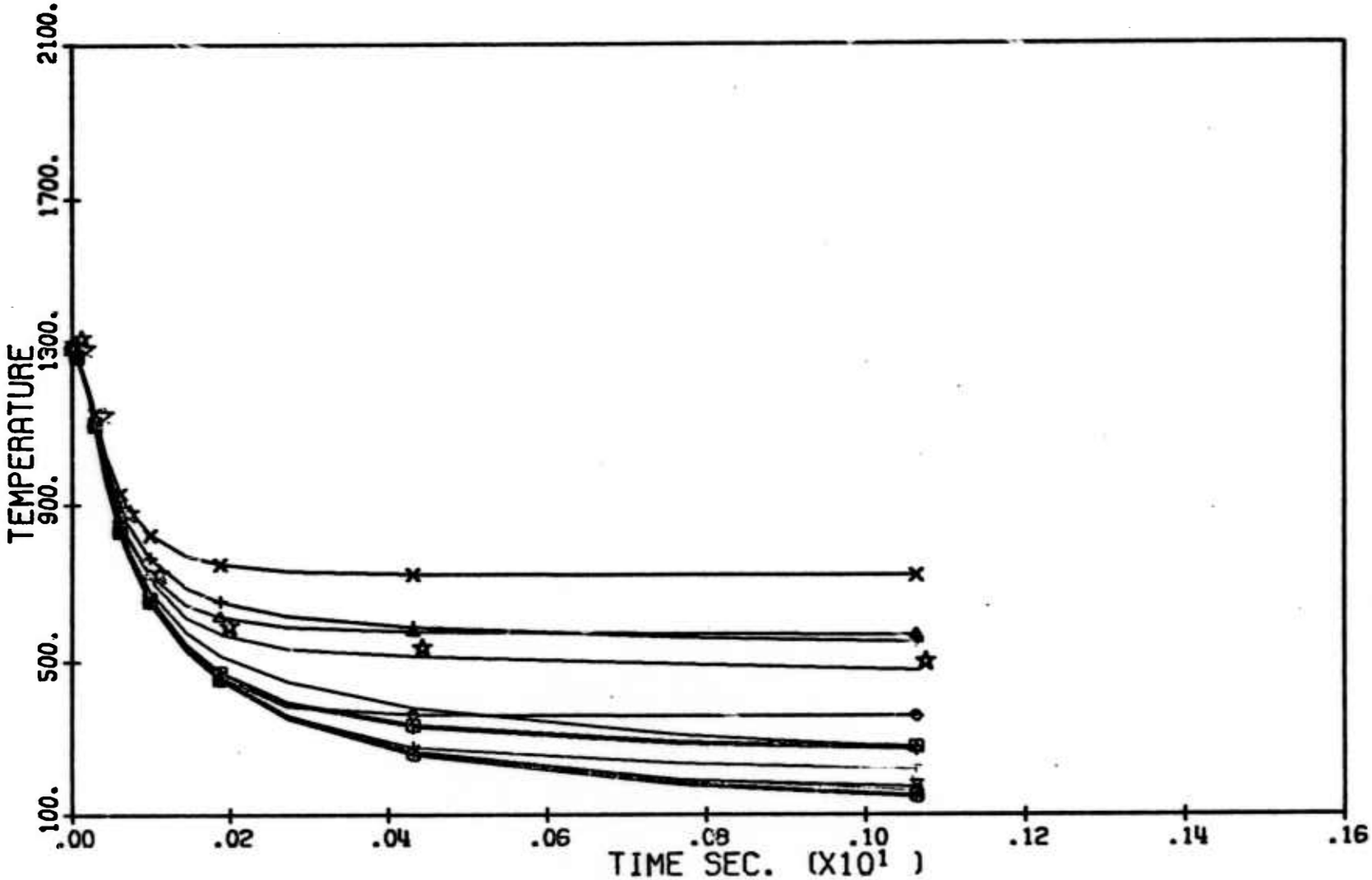

Figure 9

RELAXATION KINETICS

STREAMLINE 7

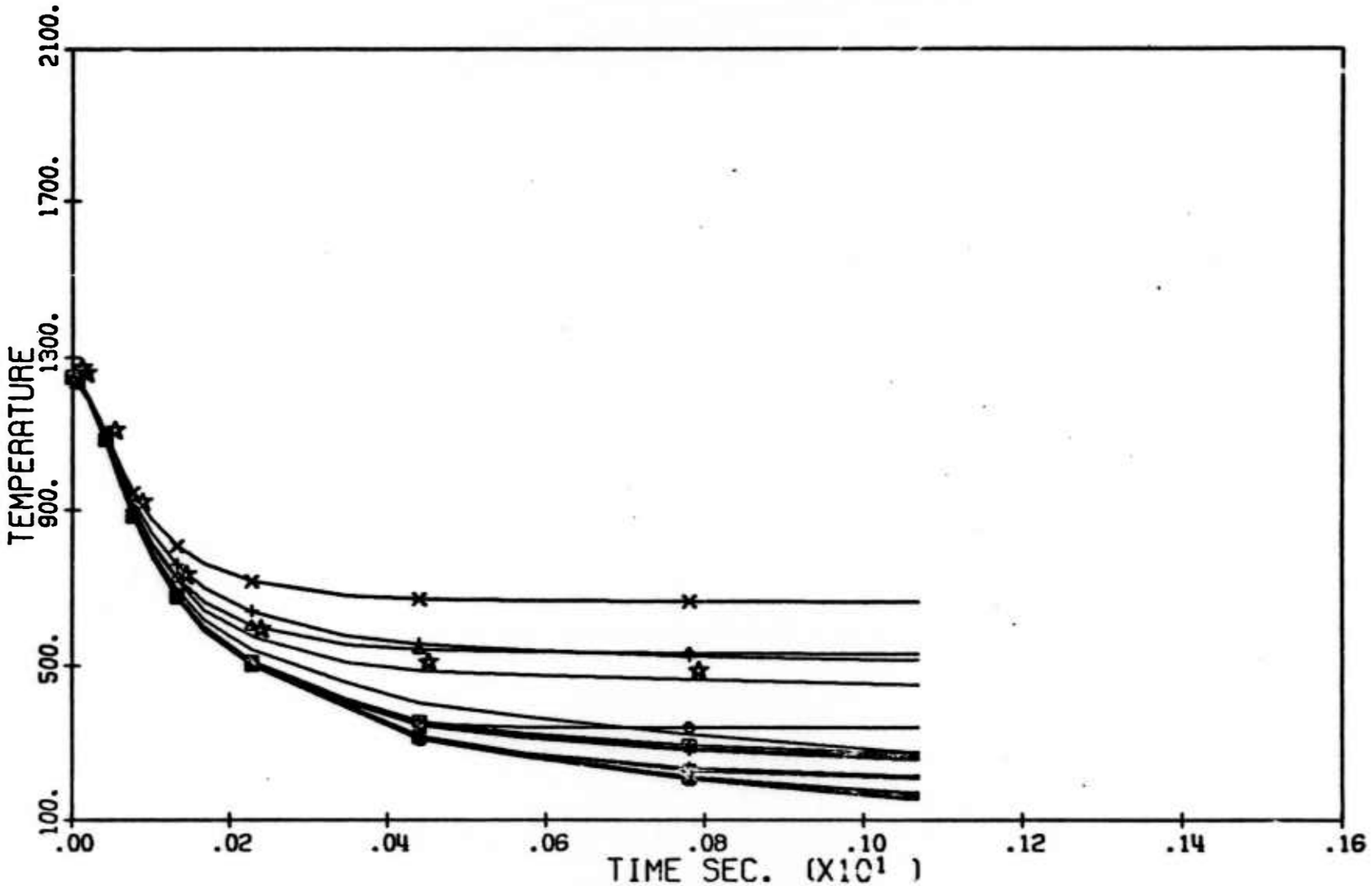

Figure 10

RELAXATION KINETICS

STREAMLINE 8

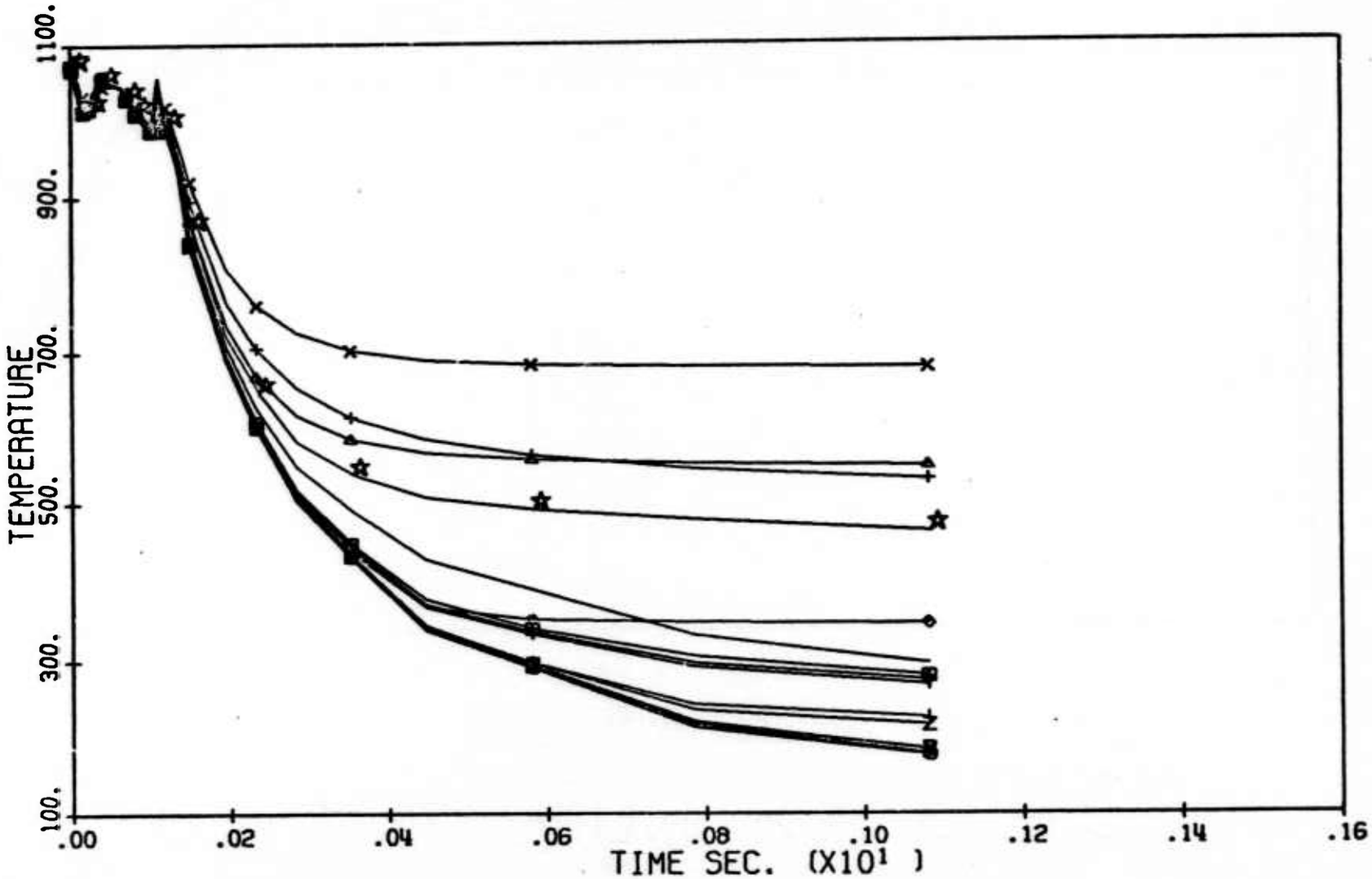

TABLE IV

History of the Kinetics for Streamline 7.

KINETICS OF THE REACTIONS

TIME = 4.472E-03 SEC PRES = 2.789E-04 ATM TEMP = 340.97 K

NO.	REACTIONS	CONSTANT	RATE
1.	H2* + H = H2 + H	5.272E-13	0.0
2.	H2 + H = H2* + H	1.165E-20	0.0
3.	H2* + O = H2 + O	5.540E-12	0.0
4.	H2 + O = H2* + O	1.225E-19	0.0
5.	H2* + H2 = H2 + H2	3.416E-16	4.737E+08
6.	H2 + H2 = H2* + H2	7.550E-24	4.139E+05
7.	H2* + H2O = H2 + H2O	3.416E-16	5.793E+09
8.	H2 + H2O = H2* + H2O	7.550E-24	5.061E+06
9.	N2* + H = N2 + H	7.820E-22	0.0
10.	N2 + H = N2* + H	4.011E-26	0.0
11.	N2* + O = N2 + O	4.458E-15	0.0
12.	N2 + O = N2* + O	2.286E-19	0.0
13.	N2* + H2 = N2 + H2	2.477E-18	3.948E+09
14.	N2 + H2 = N2* + H2	1.271E-22	6.235E+07
15.	N2* + H2O = N2 + H2O	2.477E-18	4.829E+10
16.	N2 + H2O = N2* + H2O	1.271E-22	7.624E+08
17.	OH* + H = OH + H	3.000E-11	0.0
18.	OH + H = OH* + H	8.069E-18	0.0
19.	OH* + O = OH + O	3.000E-11	0.0
20.	OH + O = OH* + O	8.069E-18	0.0
21.	OH* + H2 = OH + H2	1.000E-11	1.176E+11
22.	OH + H2 = OH* + H2	2.690E-18	3.319E+10
23.	OH* + H2O = OH + H2O	3.000E-12	4.315E+11
24.	OH + H2O = OH* + H2O	8.069E-19	1.218E+11
25.	H2O 010+ H = H2O 000+ H	2.000E-10	0.0
26.	H2O 000+ H = H2O 010+ H	2.319E-13	0.0
27.	H2O 010+ O = H2O 000+ O	1.000E-11	0.0
28.	H2O 000+ O = H2O 010+ O	1.159E-14	0.0
29.	H2O 010+ H2 = H2O 000+ H2	1.000E-11	8.300E+15
30.	H2O 000+ H2 = H2O 010+ H2	1.159E-14	7.762E+15
31.	H2O 010+ H2O = H2O 000+ H2O	1.000E-11	1.015E+17
32.	H2O 000+ H2O = H2O 010+ H2O	1.159E-14	9.493E+16
33.	H2O 001+ H = H2O 000+ H	1.000E-11	0.0
34.	H2O 000+ H = H2O 001+ H	1.222E-18	0.0
35.	H2O 001+ O = H2O 000+ O	1.000E-11	0.0
36.	H2O 000+ O = H2O 001+ O	1.222E-18	0.0

37.	H2O 001+ H2	=	H2O 000+ H2	2.000E-13	6.348E+10
38.	H2O 010+ H2	=	H2O 001+ H2	2.444E-20	1.636E+10
39.	H2O 001+ H2O	=	H2O 000+ H2O	1.000E-12	3.882E+12
40.	H2O 000+ H2O	=	H2O 001+ H2O	1.222E-19	1.000E+12
41.	H2O 001+ H	=	H2O 010+ H	1.000E-11	0.0
42.	H2O 010+ H	=	H2O 001+ H	7.718E-13	0.0
43.	H2O 001+ O	=	H2O 010+ O	1.000E-11	0.0
44.	H2O 010+ O	=	H2O 001+ O	7.718E-13	0.0
45.	H2O 001+ H2	=	H2O 010+ H2	1.000E-11	3.174E+12
46.	H2O 010+ H2	=	H2O 001+ H2	7.718E-13	9.824E+11
47.	H2O 001+ H2O	=	H2O 010+ H2O	1.000E-11	3.882E+13
48.	H2O 010+ H2O	=	H2O 001+ H2O	7.718E-13	1.201E+13
49.	CO* + H	=	CO + H	7.820E-21	0.0
50.	CO + H	=	CO* + H	8.876E-25	0.0
51.	CO* + O	=	CO + O	1.074E-14	0.0
52.	CO + O	=	CO* + O	1.219E-18	0.0
53.	CO* + H2	=	CO + H2	3.591E-16	1.652E+11
54.	CO + H2	=	CO* + H2	4.075E-20	1.650E+09
55.	CO* + H2O	=	CO + H2O	3.591E-16	2.021E+12
56.	CO + H2O	=	CO* + H2O	4.075E-20	2.018E+10
57.	CO2 010+ H	=	CO2 000+ H	1.395E-12	0.0
58.	CO2 000+ H	=	CO2 010+ H	8.247E-14	0.0
59.	CO2 010+ O	=	CO2 000+ O	3.750E-14	0.0
60.	CO2 000+ O	=	CO2 010+ O	2.217E-15	0.0
61.	CO2 010+ H2	=	CO2 000+ H2	2.790E-12	2.140E+16
62.	CO2 000+ H2	=	CO2 010+ H2	1.649E-13	2.070E+16
63.	CO2 010+ H2O	=	CO2 000+ H2O	1.000E-11	9.380E+17
64.	CO2 000+ H2O	=	CO2 010+ H2O	5.912E-13	9.072E+17
65.	CO2 010+ CO2	=	CO2 000+ CO2	7.501E-15	1.410E+14
66.	CO2 000+ CO2	=	CO2 010+ CO2	4.435E-16	1.363E+14
67.	CO2 001+ H	=	CO2 000+ H	7.820E-21	0.0
68.	CO2 000+ H	=	CO2 001+ H	3.707E-25	0.0
69.	CO2 001+ O	=	CO2 000+ O	1.074E-14	0.0
70.	CO2 000+ O	=	CO2 001+ O	5.091E-19	0.0
71.	CO2 001+ H2	=	CO2 000+ H2	3.591E-16	5.726E+10
72.	CO2 000+ H2	=	CO2 001+ H2	1.702E-20	2.136E+09
73.	CO2 001+ H2O	=	CO2 000+ H2O	3.591E-16	7.002E+11
74.	CO2 000+ H2O	=	CO2 001+ H2O	1.702E-20	2.612E+10

75.	CO2 001+ H	=	CO2 030+ H	3.103E-14	0.0
76.	CO2 030+ H	=	CO2 001+ H	5.303E-15	0.0
77.	CO2 001+ O	=	CO2 030+ O	2.649E-14	0.0
78.	CO2 030+ O	=	CO2 001+ O	4.528E-15	0.0
79.	CO2 001+ H2	=	CO2 030+ H2	6.220E-14	9.919E+12
80.	CO2 030+ H2	=	CO2 001+ H2	1.063E-14	4.366E+11
81.	CO2 001+ H2O	=	CO2 030+ H2O	4.564E-13	8.901E+14
82.	CO2 030+ H2O	=	CO2 001+ H2O	7.802E-14	3.918E+13
83.	CO2 001+ CO2	=	CO2 030+ CO2	5.275E-15	2.061E+12
84.	CO2 030+ CO2	=	CO2 001+ CO2	9.017E-16	9.074E+10
85.	CO2 001+ CO	=	CO2 030+ CO	3.957E-15	4.714E+11
86.	CO2 030+ CO	=	CO2 001+ CO	6.763E-16	2.075E+10
87.	CO2 001+ N2	=	CO2 030+ N2	3.957E-15	5.665E+12
88.	CO2 030+ N2	=	CO2 001+ N2	6.763E-16	2.494E+11
89.	H2* + H2O 000	=	H2 + H2O 001	4.334E-14	7.342E+11
90.	H2 + H2O 001	=	H2* + H2O 000	7.842E-15	2.489E+09
91.	H2* + OH	=	H2 + OH*	1.000E-12	3.122E+11
92.	H2 + OH*	=	H2* + OH	8.218E-14	9.666E+08
93.	N2* + H2O 010	=	N2 + H2O 001	3.000E-13	7.239E+12
94.	N2 + H2O 001	=	N2* + H2O 010	1.460E-13	4.148E+11
95.	N2* + H2O 000	=	N2 + H2O 010	9.858E-15	1.919E+14
96.	N2 + H2O 010	=	N2* + H2O 000	4.362E-16	3.240E+12
97.	H2O 010+ H2O 010	=	H2O 020+ H2O 000	1.847E-11	2.321E+14
98.	H2O 020+ H2O 000	=	H2O 010+ H2O 010	1.568E-11	2.437E+14
99.	CO2 001+ H2O 000	=	CO2 010+ H2O 010	1.000E-13	1.948E+14
100.	CO2 010+ H2O 010	=	CO2 001+ H2O 000	6.916E-14	8.032E+12
101.	N2* + CO2 000	=	N2 + CO2 001	5.426E-13	1.979E+15
102.	N2 + CO2 001	=	N2* + CO2 000	5.871E-13	8.380E+14
103.	N2* + CO	=	N2 + CO*	1.787E-14	2.104E+13
104.	N2 + CO*	=	N2* + CO	8.076E-15	3.326E+13
105.	CO2 001+ CO	=	CO2 000+ CO*	2.097E-13	2.471E+13
106.	CO2 000+ CO*	=	CO2 001+ CO	8.758E-14	9.226E+13
107.	CO2 101+ H2O 000	=	CO2 000+ H2O 001	3.693E-12	2.301E+13
108.	CO2 000+ H2O 001	=	CO2 101+ H2O 000	4.372E-12	3.176E+12
109.	CO2 021+ H2O 000	=	CO2 000+ H2O 001	3.693E-12	6.190E+12
110.	CO2 000+ H2O 001	=	CO2 021+ H2O 000	6.880E-12	4.998E+12
111.	CO2 101+ CO2 000	=	CO2 100+ CO2 001	3.693E-10	4.313E+14
112.	CO2 100+ CO2 001	=	CO2 101+ CO2 000	4.047E-10	4.474E+14
113.	CO2 020+ CO2 000	=	CO2 010+ CO2 010	7.386E-12	9.910E+15
114.	CO2 010+ CO2 010	=	CO2 020+ CO2 000	9.095E-12	9.760E+15

115.	H2O 020+ H	= H2O 010+ H	4.000E-10	0.0
116.	H2O 010+ H	= H2O 020+ H	5.462E-13	0.0
117.	H2O 020+ O	= H2O 010+ O	2.000E-11	0.0
118.	H2O 010+ O	= H2O 020+ O	2.731E-14	0.0
119.	H2O 020+ H2	= H2O 010+ H2	2.000E-11	2.546E+13
120.	H2O 010+ H2	= H2O 020+ H2	2.731E-14	2.267E+13
121.	H2O 020+ H2O	= H2O 010+ H2O	2.000E-11	3.113E+14
122.	H2O 010+ H2O	= H2O 020+ H2O	2.731E-14	2.772E+14
123.	CO2 020+ H	= CO2 010+ H	2.790E-12	0.0
124.	CO2 010+ H	= CO2 020+ H	2.031E-13	0.0
125.	CO2 020+ O	= CO2 010+ O	7.501E-14	0.0
126.	CO2 010+ O	= CO2 020+ O	5.461E-15	0.0
127.	CO2 020+ H2	= CO2 010+ H2	5.506E-12	3.228E+15
128.	CO2 010+ H2	= CO2 020+ H2	4.008E-13	3.074E+15
129.	CO2 020+ H2O	= CO2 010+ H2O	2.000E-11	1.434E+17
130.	CO2 010+ H2O	= CO2 020+ H2O	1.456E-12	1.366E+17
131.	CO2 020+ CO2	= CO2 010+ CO2	1.500E-14	2.155E+13
132.	CO2 010+ CO2	= CO2 020+ CO2	1.092E-15	2.052E+13
133.	CO2 030+ H	= CO2 020+ H	4.405E-12	0.0
134.	CO2 020+ H	= CO2 030+ H	2.838E-13	0.0
135.	CO2 030+ O	= CO2 020+ O	1.125E-13	0.0
136.	CO2 020+ O	= CO2 030+ O	7.250E-15	0.0
137.	CO2 030+ H2	= CO2 020+ H2	8.443E-12	3.467E+14
138.	CO2 020+ H2	= CO2 030+ H2	5.440E-13	3.189E+14
139.	CO2 030+ H2O	= CO2 020+ H2O	3.000E-11	1.507E+16
140.	CO2 020+ H2O	= CO2 030+ H2O	1.933E-12	1.386E+16
141.	CO2 030+ CO2	= CO2 020+ CO2	2.283E-14	2.297E+12
142.	CO2 020+ CO2	= CO2 030+ CO2	1.471E-15	2.113E+12
143.	H2O 100	= H2O 000+ HV	7.143E+00	1.502E+10
144.	H2O 010	= H2O 000+ HV	2.222E+01	7.878E+13
145.	H2O 001	= H2O 000+ HV	7.143E+01	9.683E+10
146.	H2O 020	= H2O 010+ HV	4.545E+01	2.471E+11
147.	CO2 010	= CO2 000+ HV	3.030E+00	9.927E+13
148.	CO2 001	= CO2 000+ HV	4.000E+02	2.724E+14
149.	CO2 101	= CO2 000+ HV	1.099E+01	2.395E+10
150.	OH*	= OH + HV	3.333E+00	1.675E+08
151.	CO2 100+ M	= CO2 020+ M	1.000E-10	9.740E+17
152.	CO2 020+ M	= CO2 100+ M	6.468E-11	9.718E+17

a representative history of the rates and rate coefficients for streamline 7 during the latter phases of the relaxation process. For each of the diatomic species, CO, H_2 and N_2 the major loss process is a VV process generally involving a polyatomic species. CO tends to freeze at the highest temperature with the major loss process being the VV pumping of CO_2 to $CO_2(001)$. N_2^* relaxes somewhat more rapidly than CO due primarily to the more rapid coupling of N_2^* to $CO_2(001)$. H_2^* freezes close to the N_2 value with the major loss process being the VV pumping of $H_2O(001)$. None of these diatomic molecules have VT loss processes which compete with the VV processes in magnitude at least for the species mole fractions encountered in these streamlines.

Both CO^* and N_2^* pump $CO_2(001)$ so this polyatomic mode tends to freeze out substantially above the bending modes. $CO_2(101)$ tends as well to freeze out above the bending modes since this combination mode is formed with nearly gas kinetic collision figuring from $CO_2(001)$ and $CO_2(100)$. These excited CO_2 modes give rise to $4.3\mu[CO_2(001)]$ and 2.7μ $[CO_2(101)]$ in amounts above that expected from LTE values.

Lastly, these calculations suggest that H_2^* enters the mixing layer region of the plume flow field as a result of vibrational freezing in the vacuum core. The effect this H_2^* has on chemiluminescent processes in the mixing layer is being currently investigated particularly through reactions such as

$$O + H_2^* \rightarrow OH + H \ .$$

Theoretical and experimental studies on the role of vibrational energy in simple combustion reactions such as this will clarify the importance of vibrational freezing in the core flow field on plume radiance.

Bibliography

(1) E.R. Fisher and R.H. Kummler, "Baseline Chemistry Model for Plume Radiation Predictions," Physical Dynamics Report PD-73-052, AFCRL-TR-74-0175, December (1973).

(2) F.P. Boynton, private communication.

(3) F.P. Boynton, "Numerical Calculations of Visions High Altitude Exhaust Plume Flow Fields," Research Institute for Engineering Sciences Report 70-18, December (1970).

(4) E.R. Fisher and R.H. Kummler, J.Chem.Phys. 49, 1075, 1085 (1968).

PART IV: Determination of the Intermolecular Potentials between Oxygen Atoms and Plume Species

P. B. Foreman, A. B. Lees and P. K. Rol

Introduction

Many reactions of interest in the upper atmosphere involve collisions between molecules and atomic oxygen. Theoretical cross sections for vibrational relaxation processes involving H_2O, CO_2, CO, N_2, H_2 and O atoms have been determined by Marriott.[1] Many of these theoretical estimates are the only available results to use in model non-equilibrium calculations involving these molecules. The calculation of cross sections for vibrational excitation of these molecules by heavy body collisions are carried out by using a numerical close coupling solution of the wave equation for the colliding system. This system is characterized by a breathing sphere model of Schwartz, Slawsky and Herzfeld[2] to represent the target molecular vibrator and by an empirical spherically symmetric scattering potential. Reliable central potentials required for the calculation of the excitation cross sections were not always available. We have, therefore, calculated these potentials from scattering cross sections, analogous to potentials determined for He-He interaction.[3] Objections to the approximation of anisotropic interactions by spherically symmetric potentials will be considered in the discussion of the results. Sinanoğlu has suggested an alternative method for calculating potential parameters in the additive force approximation.[4] We have applied this model, assuming exponential interatomic potentials, to the collisions of O atoms with homonuclear diatomics; the results are compared with those of Leonas.[5] We also present the raw cross section data and scattering configuration so that other methods can be applied to the data when they become available.

Experimental Method

Details of the apparatus have been given[3] elsewhere so that here we discuss only the scattering geometry and problems specific to this work.

Ions of atomic oxygen are produced by electron impact on O_2, proceeding via dissociative attachment, dissociative ionization or ion pair formation.[6] Either positive or negative ions are extracted from the source and momentum selected in a transverse magnetic field. O ions are unambiguously distinguished from the neighboring OH ions by calibration with a Hall probe. Neutral O atoms are obtained by charge transfer with O_2 in the case of O^-, and with Kr, Xe, N_2 or H_2O in the case of O^+. Belyaev, Kamyshov and Leonas (BKL) have used this technique to measure the O-Ne potential and report significantly smaller cross sections when the O atoms are produced from O^+ and Xe.[7] Based on the favorable energy defect, this was attributed to the formation of metastable $O(^1D)$ in the charge transfer reaction.

The scattering configuration has cylindrical symmetry in which the entrance hole to the target gas cell has diam. $d_B = 0.0203$ in. while the effective diam. of the Channeltron detector is $d_D = 0.0362$ in. The beam is almost parallel giving a rectangular intensity distribution of width d_B. The exit hole of the scattering cell has a diameter of 0.025 in. so that an optical path exists between the detector perimeter and all points in the scattering path. The distances from the detector to the entrance and exit holes of the scattering cell are respectively 1.431 in. and 0.985 in. Unless otherwise stated, the experimental incomplete integral cross section $\bar{Q}^{exp}$ shall be understood to include an end correction, typically 2%, to take account of the nonuniform target gas density. Thus in calculating cross sections for comparison with experiment we may assume a uniform density inside the cell, and zero density outside.

I Noble Gases

Results and analysis

$\bar{Q}^{exp}$ was measured as a function of lab. energy in the range 100-2500eV. The interaction potential is assumed to have the exponential form $V(r) = A \exp(-\alpha r)$. By introducing reduced variables we have simplified the problem of finding A and α to a one-parameter search for A, α being determined by a least squares condition; details of the analysis are given in Appendix A. The results are given in Table I. With the exception of the O-Ne and O-He potentials (Table 1, Figs. 1,2) which are averages of all our data, Xe was used as the charge transfer gas in order to observe the effects, if any, of excited states of oxygen.

The attenuation of a beam by a scattering gas is given in the usual notation[3] by

$$I = I_0 \exp(-n\bar{Q}l) \tag{1}$$

When the *gas* contains several species with mole fraction x_i we have instead

$$I = I_0 \exp\left[-nl \sum_i x_i \bar{Q}_i\right] \tag{2}$$

which is experimentally indistinguishable from the case of a pure gas. However, Turner et al[8] have noted that when the *beam* is mixed

$$I = I_0 \sum_i x_i \exp[-n\bar{Q}_i l]. \tag{3}$$

Here a plot of $\ln(I/I_0)$ versus n is nonlinear, and in principle one may obtain the individual $\bar{Q}_i$ by curve fitting. In a study of charge transfer[8] the authors were able to obtain cross sections for a mixed beam of energetic $O^+(^4S^o)$ and $O^+(^2D^o)$. However, such an experiment is not sensitive to multiple collisions so that 90% or even 95% attenuation could be achieved. In the present work, due to the effect of multiple collisions, we are restricted to attenuation <70% in which range nonlinearity is manifested

only for a very large ratio of cross sections. It is thus not surprising that nonlinearity was not observed in the present experiments. However, provided the cross sections differ for different states of the beam, the measured cross section, being a weighted average over states, will change as a function of relative concentration. Careful measurements on the scattering with Ne revealed no significant changes in cross section irrespective of the method of production of the O atoms, contrary to the findings of BKL.

Discussion

BKL assumed that electron transfer from O^- results exclusively in $O(^3D)$, the energy defect being $\Delta E = -1.03eV$[9] for the case

$$O^-(^2P) + O_2(X^3\Sigma) \rightarrow O(^3P) + O_2^-(X^2\Pi). \quad (4)$$

But we cannot dismiss the possibility of forming $O(^1D)$ although since $\Delta E = -2.99eV$ it is less probable. In the case of O^+, charge transfer with Xe was assumed to proceed via

$$O^+(^4S) + Xe(^1S) \rightarrow O(^3P) + Xe^+(^2P), \Delta E = -1.49eV \quad (5)$$

and

$$O^+(^4S) + Xe(^1S) \rightarrow O(^1D) + Xe^+(^2P), \Delta E=0.47eV. \quad (6)$$

Charge transfer with Kr represents an intermediate case since the energy defects for (5) and (6) are respectively 0.38 and 2.34eV. We note that reaction (6) violates Wigner's spin rule. If one invokes interatomic LS coupling then the observations of BKL are not necessarily inconsistent with an increased concentration of $O(^1D)$ as one changes from Kr to Xe, due to the increasing mass. However, this mechanism does not explain the

independence of cross sections as a function of charge transfer reaction in this work. From the stated range of the potential, determined by the distance of closest approach r_0, and the relation $\bar{Q} \simeq \pi r_0^2$, we deduce that the O-Ne cross sections of BKL changed by as much as 11% at the lowest energy which is well beyond experimental error, but only 1.4% at 4000 eV, whereas in the present work the maximum difference was only 3.6% throughout the range. The O-Ne cross sections with Kr and Xe charge transfer were here an average of 1.6% and 1.3% respectively lower than for O^- with O_2, but this is within experimental error estimated as $\pm$ 1%. Indeed scattering with a He target gas produced an opposite but equally insignificant trend. As a further check a number of measurements were made with N_2 and also H_2O as charge exchange gas yielding the same cross sections. The energy defects for production of $O(^3P)$ and $O(^1D)$ are respectively 1.97 and 3.93eV for N_2, and -1.00 and + 0.97eV in the case of H_2O. Again the reactions

$$O^+ (^4S) + N_2 (X^1\Sigma) \rightarrow O(^1D) + N_2^+ (X^2\Sigma) \qquad (7)$$

and

$$O^+ (^4S) + H_2O (\tilde{X}^1A_1) \rightarrow O(^1D) + H_2O^+ (\tilde{X}^2B_1). \qquad (8)$$

are spin forbidden. Charge transfer reactions are in general highly velocity dependent, but five different reactions yielded the same O-Ne cross sections over the entire energy range. Theoretical calculations[10] give a much higher potential for the triplet state. We thus conclude that our beam contained a negligible fraction of the metastable state.

The results provide strong evidence that spin is conserved in these experiments, and also then in those of BKL since their lab. energy extending from 290-4000eV* largely overlaps this work. We must therefore seek an alternative explanation of their results. One possibility is that

---

* It appears that the stated lowest energy of 290eV may refer to another system. From the relation $\ln\bar{Q}/\ln E = -2/s$ where $V=Kr^{-s}$, we obtain a lower limit of 600eV for the O-Ne systems of BKL. The range 600-4000 eV was normally used in previous work (Ref.11).

their electron multiplier[11] is more sensitive to metastables than the Channeltron used here, which would explain the increasing effect with lower energy. However, the excitation energy of $O(^1D)$ is only 1.96eV which seems insufficient for the production of Auger electrons. The major difference in the cross sections of BKL is between O^+ and O^- rather than the different charge transfer reactions of O^+. Such differences may arise if the ion extraction field penetrates the source plasma to the cathode region resulting in a higher energy for O^- and a lower energy for O^+. This is more significant at lower energies, but can be dismissed since the predicted deviations are the opposite of those observed. A more probable cause also lies in the different design and operation of the ion source.[11] We have already remarked that Turner et al found up to 30% $O^+(^2D)$ as the electron energy was increased from threshold up to 100eV. Due to the different extraction efficiencies for the ^4S and ^2D states, resulting from formation on different repulsive states of O_2^+, the relative concentrations may be a sensitive function of the source construction.[8] Charge transfer of O^+ (^2D) with Kr, Xe, N_2 or H_2O may yield either $O(^3P)$ or $O(^1D)$ with conservation of spin. The energy defects are respectively -2.92, -4.79, -1.34 and 4.30eV to form $O(^3P)$, and -0.96, -2.83, +0.62 and -2.34eV to give $O(^1D)$. Thus excited O^+ ions may preferentially form $O(^1D)$, although in the case of N_2 we might also expect to form the excited N_2^+ $(A^2\Pi_u)$ or vibrationally excited N_2^+ $(X^2\Sigma)$ which favor $O(^3P)$. Similarly, H_2O^+ $(\tilde{A}^2A_1)$ may participate.† In this work we were unable to detect any changes

† We may discount excited states of Kr^+ or Xe^+ since they lie c.a. 9eV above the ground state.

in cross section when source operating conditions were altered. The variable parameters were source pressure, electron energy, extraction potential, and the use of CO instead of O_2 in the source. This may simply imply that excited O^+ ions were present in this work, but that despite the unfavorable energy defect the dominant channel is formation of $O(^3P)$, making them indistinguishable from the ground state ions. The explanation of BKLs' observations is thus not definitely established, but may be due to the presence of O^+ (^2D) in their ion beam.

Although we have assumed that the *relative* differences in the O-Ne cross sections of BKL are beyond experimental error, such differences in *absolute* determinations by independent workers are not uncommon. This is evident from the difference between BKL and this work in the O-Ne potential obtained from O^- (Fig.2) where there can be no difference in the relative proportions of singlet and triplet atoms at a given lab. energy.* Leonas, in a recent review,[5] has corrected the earlier measurements of all the oxygen-noble gas systems[7,12,13] for errors in the size of the aperture, which changes the magnitude of the potential but leaves the range unchanged. Agreement with this work, however, is not improved (Figs. 1,2).

---

* Assuming that the relative concentrations of $O(^3P)$ and $O(^1D)$ change as a function of lab. energy, a difference between the potentials of BKL and this work may result since, due to differences in angular resolution, the *same* lab. energy gives information about *different* regions of the potential curve in the two experiments. However, the reported differences in potential seem too large to be accounted for in this way.

Leonas notes[5,7] that calculations of the molecular singlet state by Allen et al.[10] lie substantially above the measurements of BKL. Since the triplet lies at still higher energies, this is not consistent with the view that the measurements represent some mixture of states. He thus concludes that the calculations are in error. The present work suggests that the theory is more likely to be correct. The authors[10] also estimated that the molecular triplets lie even higher than the doublets of the corresponding fluorides. The comparison with this work for Ne and He (Figs. 1,2) shows that they are nearly equal which is reasonable agreement.* A further estimate of the triplet states is provided by Thomas-Fermi-Dirac (TFD) model calculations.[14,15] The heteronuclear diatomics are obtained from the corresponding homonuclear potentials by the empirical combination rule $V_{12} = (V_{11}V_{22})^{1/2}$. We see (Figs. 1,2) that the results of Gaydaenko and Nikulin are in excellent agreement with this work, whereas the calculations of Abrahamson are known to be too high.[16,17]

---

* The unpublished calculations of the triplet states must be regarded with caution since they were at the limit of technical capabilities then available, but in this range they certainly lie above the singlet state calculations, which are considered to be reliable. L.C. Allen (private communication).

The O-Kr and O-Xe potentials of Belyaev and Leonas[13] are also corrected for errors in pressure calibration, which does alter the range.* Comparing these revised potentials (Fig.3) we see that they all lie substantially below those obtained in this work, but the difference is probably too large to be explained on the basis of excited O atoms. Furthermore, instead of the expected increase in potential with size of the target atom, they show reverse ordering for Ar, Kr and Xe, and predict the same potential for O-Ne and O-Ar at a separation of 1.8Å. Possibly, at least in the case of Xe, there is typographical error; increasing the O-Xe potential by a factor of 10 brings it into moderate agreement with this work. The TFD calculations of Gaydaenko and Nikulin are in fair agreement with this work.

---

*
Ref. (5) does not quote the range of validity. We must therefore assume that the cross section and thus the range, which varies as $\bar{Q}^{1/2}$, is not greatly altered.

Summary

We find that the oxygen beam used in this work consists only of ground state atoms, irrespective of the charge transfer reaction used to generate that beam. This is still consistent with the observations by BKL of a mixture of ground and excited states from the same reactions. However, the formation of excited $O(^1D)$ atoms from ground state ions is spin-forbidden and does not occur to any significant extent. We postulate that the ion beam of BKL contained excited $O^+(^2D)$ ions. In future experiments a pure $O(^3P)$ beam might best be obtained by photodetachment from O^-. It has been suggested[41] that this method might also be used to obtain fast neutral beams with a high concentration of ^1D and ^1S states for which the threshold energies are 3.433eV (3611Å) and 5.656eV(2192Å) compared with 1.465eV(8463Å) for the ground state. By calibration against a reliable theoretical potential for say $O(^1D)$-He[10] one could then obtain the interactions with $O(^1D)$ for any other system.

The resulting oxygen-noble gas potentials are much larger than those of BKL and still higher than the revised estimates of Leonas. The absolute difference seems too great to be attributed solely to excited states, but theoretical estimates are in better agreement with the present work.

II Atmospheric Molecules

Analysis and results

The interactions of molecules are characterized by an anisotropic potential, which may, however, in the simplest approximation be treated as a spherically symmetric potential. The analysis which then proceeds exactly as for atoms will be referred to here as the potential averaging (PA) procedure. Until the recent work of Leonas[5] nearly all scattering experiments were so treated.[18] Theoretical calculations on the $He-H_2$[19] and $H-H_2$[20] systems have used a one-center expansion in Legendre polynomials to describe the anisotropic potential:

$$V(R,d,\psi) = \sum_{\ell} V_{\ell}(R,d)\, P_{\ell}(\cos\psi) \qquad (9)$$

where R is the distance between centers of mass of the atom and molecule, d is the molecular bond length and ψ is the angle between R and d. Due to the difficulty of uniquely determining more than two parameters, experimental work has utilized the additive potential model in which the intermolecular potential is simply the sum of the individual interatomic interactions. Thus for the system A + BC we have

$$V(R,\psi) = V_{AB}(r_{AB}) + V_{AC}(r_{AC}) \qquad (10)$$

for a particular orientation, and the spherically symmetric potential $\overline{V(R)}$ is the average of all orientations of $V(R,\psi)$. Amdur, Mason and Jordan[21,22] have successfully used this model to extract effective atom-atom interactions of the form $V = Kr^{-s}$ (where K and s are constants) from experimental PA interactions of atoms with homonuclear diatomics. With the aid of combination rules they then construct molecule-molecule potentials in good agreement with other data. The extension to heteronuclear diatomics and more

complicated systems requires, in general, the determination of more than two potential parameters from the experimental data. Leonas overcomes this difficulty by assuming that all atoms within a molecule are identical. Amdur et al[23] have introduced the peripheral force approximation to treat CH_4, in which the interaction of the central carbon atom is ignored.

Sinanoğlu has noted[4] that in the time scale of a collision, the target molecule undergoes negligible rotation under these experimental conditions. Given a trial potential, one should therefore calculate the cross section for each orientation and *then* average to compare with experiment. This procedure is termed cross section averaging[18](CSA) to distinguish it from the straightforward PA method. The latter would be valid in the limit of rapid rotation of the target. Expressing the potential as an expansion in Gegenbauer (ultra-spherical) polynomials*, Sinanoğlu estimates[4] that the Ar-N_2 potential of Amdur[21] is increased by about 5% in this way, which is within experimental error. The present work extends to shorter range where the difference may become larger as the molecular structure becomes increasingly important. Furthermore, Leonas states that the two methods differ by a factor of two in some cases[5] which is certainly well beyond experimental error.

We shall treat only the interactions of O atoms with H_2, N_2 and O_2 by the CSA procedure. In order that other methods in addition to PA may be applied to these and the remaining data, the cross sections $\bar{Q}^{exp}(E)$, including an end correction, are given in Table II. The scattering geometry is given above. PA parameters A and α are given in Table III and the results compared with other data in Figs. 4-9. The only other direct experimental

---

*This is equivalent to the assumption of additive inverse power interatomic potentials.[24]

data are those of Leonas and coworkers.[5,25-29] Their PA curves lie both above and below this work, the largest disagreement being 50-100% in the cases of N_2 and O_2 (Figs.5,6). Jordan, et al[22] indirectly predict potentials for O-N_2, O_2 and NO by applying an additive potential model together with the geometric mean combination rule to their PA results for Ar-Ar, N_2 and O_2. These are slightly higher than this work but in reasonable agreement,* whereas the semi-empirical calculations of Yun and Mason,[30] and of Vanderslice et al[31] are probably too high (Figs.5-7).

Considering now the CSA method, we assume that the interatomic potential for say O-H in the O-H_2 system is given by $V(r) = A \exp(-\alpha r)$. In addition to averaging over the scattering path at each energy, as in the central field or PA case, we must now integrate over all orientations of the target to obtain the calculated cross section $\overline{Q}^{calc}(E)$. A two parameter search for A and α would be a costly computation. However, a simple iterative procedure converges rapidly to the one-parameter search for A independent of α as in the case of the noble gases (see Appendix B). The spherically averaged atom-molecule potential is then given by[32]

$$\overline{V(R)} = 2Ae^{-\alpha R}(\alpha^2 Rd)^{-1} [2(\alpha R+1) \sinh(\alpha d/2) - \alpha d \cosh(\alpha d/2)]. \qquad (11)$$

In practice this function may be approximated by the form

$$\overline{V(R)} = \bar{A} \exp(-\bar{\alpha} R) \qquad (12)$$

---

* From experimental considerations, the Ar-N_2 potential in Ref. 22, and hence those derived from it, are known to be somewhat too high. J.E. Jordan (private communication).

with negligible error. We take the range of validity to be the same as that given by potential averaging. The range of the "interatomic" potentials $V(r) = A \exp(-\alpha r)$ is not obvious. However, we follow Vanderslice et al and substitute the limits of R in

$$R = r \left[1 + \frac{1}{12} \left(\frac{d}{r}\right)^2\right] \qquad (13)$$

to obtain the limits of r. The results are given in Tables IV & V.

Discussion

The CSA potentials for H_2, N_2 and O_2 (Figs. 4-6) are slightly higher than the PA results and in excellent agreement with the predictions of Sinanoğlu. We find that the differences increase with increasing bond length and decreasing R as expected. However, even for O_2 the maximum difference is only 18%. The foregoing comments apply equally well to the "interatomic" potentials (Figs. 10-12) which comprise the final intermolecular potentials. Here the PA potentials were obtained by a method analagous to that employed by Amdur et al for an inverse power representation.[21] The parameters are listed in Table VI. Clearly these potentials cannot be expected to apply to free atoms, but we nevertheless present them for comparison with similar data. As required for internal consistency, the results of Jordan are again slightly higher, and the semi-empirical calculations still larger, with the exception of the O-N result of Meador.[32] Leonas' potentials are much lower than the rest.

We are unable to explain the large differences found by Leonas between the PA and CSA procedures. In particular, his finding of lower CSA than PA potentials (for CO they intersect and for CO_2 the earlier CSA results of Kalinin, et al.[28,29] are higher) is contrary to the

predictions of Sinanoğlu and results of this work. Since the CSA results appeared in a later review[5] it is possible that changes in calibration altered the previous experimental cross sections.* Comparison is also hindered by a failure to state the range of validity. It is implied that the potentials are valid in the range 0.1 - 10eV,[5,29,33] but assuming that the CSA results are a reanalysis of the earlier PA data,** then this must overstate the range. We conclude from a comparison of this and other work, that at least in the case of $O\text{-}O_2$ and $O\text{-}N_2$, the CSA potentials of Leonas are incorrect.

The usefulness of the additive force model is demonstrated by the O-NO potential. Combining our CSA results for O-O and O-N obtained from $O\text{-}O_2$ and $O\text{-}N_2$, we predict a potential for O-NO which is in very close agreement with our direct PA result (Fig.7). This method is more accurate than the alternative assumption that the molecules have spherical symmetry. This is demonstrated in Fig.8 where we show an indirect prediction of the O-CO potential ($V(R) = 539 \exp(-2.932R)$eV, $1.31 \leq R \leq 2.44$Å) obtained by applying the geometrical mean combination rule directly to the potential averaged Ar-CO, Ar-Ar and O-Ar interactions.***

---

*
Changes in calibration of geometry and pressure were applied to the O-noble gas data.

**
Such an assumption is made on the grounds that these and all the other data (with the apparent exception of $O\text{-}H_2$ which we have not found in the literature) have been previously published in PA form.

***
The Ar-Ar potential and the potential averaged Ar-CO interaction obtained in this laboratory are respectively $V(r) = 5061 \exp(-3.598r)$eV, $1.70 \leq r \leq 2.65$Å and $V(R) = 3450 \exp(-3.313R)$eV, $1.79 \leq R \leq 2.76$Å.

We have not thought it worthwhile to make the more drastic assumptions required for a direct CSA treatment of the heteronuclear diatomics and triatomics. Clearly as the molecule becomes larger and more complex the differences between PA and CSA potentials become more severe. However, with the caution that they are probably at least 10% too low, the PA potentials obtained here for O atoms interacting with NO, CO, CO_2 and H_2O will be adequate for many purposes. We note that the difference between the PA potentials is small for the isoelectronic O-N_2 and O-CO interactions.

One must also remember that chemical interaction may be involved in all the oxygen atom-molecule collisions so that the potentials are also an average over states. The higher angular resolution employed by Leonas has permitted the observation of such curve crossings.[5,25]

APPENDIX A

Analysis of atom-atom scattering

For systems involving a projectile of mass m_1 and target of mass m_2, where $m_1 < m_2$, the traditional analysis in terms of the first order momentum approximation[3,34] is entirely adequate. However, when $m_1 > m_2$ (e.g. O-He or the potential averaged O-H_2) it becomes necessary to include higher order terms in the momentum expansion. These terms have been evaluated by Lehmann and Leibfried[35] and by Smith et al[36] for several forms of the potential V(r). In an exact analysis the classical center of mass (c.m.) scattering angle χ is related to the impact parameter b by

$$\chi = \pi - 2b\int_{r_o}^{\infty} \left[1 - \frac{V(r)}{E_T} - \frac{b^2}{r^2}\right]^{-\frac{1}{2}} \frac{dr}{r^2} \qquad (A1)$$

where r_o is the largest zero of

$$\frac{V(r)}{E_T} + \frac{b^2}{r^2} = 1 \qquad (A2)$$

and E_T is the total energy of the system. Here we substitute for E_T the initial kinetic energy E_r in the absence of interaction given by

$$E_r = m_2 E/(m_1 + m_2) \qquad (A3)$$

where E is the projectile lab energy. In these experiments the target thermal energy is negligible.

The momentum approximation sets $b = r_o$ (valid when $V \ll E_r$) and one evaluates Eq. A1 as an expansion in powers of V/E_r:

$$\chi = \sum_i \chi_i \tag{A4}$$

For the exponential form $V(r) = A \exp(-\alpha r)$ the first few terms are[35]

$$\chi_1 = \frac{A}{E_r} \alpha b \, K_0(\alpha b) \tag{A5}$$

$$\chi_2 = -\frac{A^2}{E_r^2} K_1(2\alpha b) \tag{A6}$$

$$\chi_3 = \frac{A^3}{E_r^3} \left\{ \frac{9}{8} (\alpha b)^3 K_0(3\alpha b) - 3\alpha b K_1(3\alpha b) + \frac{15}{8} (\alpha b)^2 K_0(3\alpha b) \right\} \tag{A7}$$

where K_i is the ith order modified Bessel function. In the usual analysis[3,34] θ_m, the minimum lab angle required for the projectile to miss the detector after scattering from a given point in the cell, is related to χ_m via the small angle approximation

$$\chi \simeq \frac{m_1 + m_2}{m_2} \theta \tag{A8}$$

The corresponding impact parameter b_m is then obtained from Eq.A5 by Newton-Raphson iteration to give the single ray cross section (ignoring back scattering)

$$Q^{calc}(E) = \pi[b_m(E,\chi_m)]^2 \tag{A9}$$

for that point. The final calculated cross section $\bar{Q}^{calc}(E)$ is then the volume average of $Q^{calc}(E)$ over the scattering path. This is evaluated by a 3-fold Gauss-Legendre quadrature, each of 8 points for a total of 512. The parameters A and α must be adjusted to give the closest fit to the experimental energy dependence of the cross section. Clearly as one

includes higher order terms in the expansion of χ, the computation becomes very long. Furthermore the asymptotic expression

$$Q^{\frac{1}{2}} = \left(\frac{\pi}{\alpha}\right)^{\frac{1}{2}} \ln\left[\pi^{\frac{1}{4}} \frac{\alpha}{2}^{\frac{1}{2}} \frac{A}{\theta_m}\right] + \frac{\pi^{\frac{1}{2}}}{\alpha} \ln\left(\frac{Q^{\frac{1}{4}}}{E_r}\right) \qquad \text{(A10)}$$

is no longer useful to predict the value of α when $m_2 >> m_1$.

One must then also use the exact c.m.-lab transformation

$$\tan\theta = \frac{m_2 \sin\chi}{m_2 \cos\chi + m_1} \qquad \text{(A11)}$$

For the present geometry the maximum lab angle detected is 0.0285 rad. Xe - He at 100 eV, to consider an extreme case, then gives the corresponding forward c.m. angle χ = 1.24 rads. which is no longer small. Use of Eq.A8 gives 22% error in χ. This could be reduced to 1.6% by using the second order expression for forward scattering

$$\chi \simeq \arcsin\left\{-\cot\theta + \cot\theta\left[1 + 2\left(\frac{m_1 + m_2}{m_2}\right)\tan^2\theta\right]^{\frac{1}{2}}\right\} \qquad \text{(A12)}$$

However, in this work Eq. A11 was solved iteratively for χ starting from (A12).

Analysis for an inverse power potential is much more direct giving to first order

$$\bar{Q}^{calc}(E) = \pi\left(\frac{KC_1}{E}\right)^{2/s} \langle\theta_m^{-2/s}\rangle \qquad \text{(A13)}$$

where $C_1 = \pi^{\frac{1}{2}}\,\Gamma(s/2 + 1/2)/\,\Gamma(s/2)$ and to 2nd order

$$\bar{Q}^{calc}(E) = \pi\left(\frac{KC_1}{E}\right)^{2/s}\left\{\langle\theta_m^{-2/s}\rangle - \frac{2(m_1 + m_2)}{sm_2C_1^2} C_2 \langle\theta_m^{1-2/s}\rangle\right\} \qquad \text{(A14)}$$

where $C_2 = \pi^{\frac{1}{2}} \Gamma(s + \frac{1}{2})/2\Gamma(s - 1)$.[3] However, (A14) assumes the validity of (A8) which is inconsistent with the need to include χ_2 in the momentum expansion. It would be preferable to use $\chi(\theta_m)$ from (A12) in the expression

$$\bar{Q}^{calc}(E) = \left[\frac{(m_1 + m_2)KC_1}{m_2 E}\right]^{2/s} \left\{ \langle [\chi(\theta_m)]^{-2/s} \rangle - \frac{2C_2}{sC_1^2} \langle [\chi(\theta_m)]^{1-2/s} \rangle \right\} \quad (A15)$$

The convergence of Eq. A4 has been considered in detail by Leibfried and Plesser.[37] We see from Fig. 13 that with this apparatus the series diverged at all energies for Xe - He ($m_2/m_1 \simeq 32$). Even the Ar - He system ($m_2/m_1 \simeq 10$) diverges here at the lowest energies; this case has formerly been analyzed in terms of Eq. A13.[38] Thus caution must be exercised in using the momentum approximation particularly since the leading term gives results which may appear reasonable in the absence of data for comparison (see Fig. 14). Furthermore, for $\alpha b > 3^{3/2}$ the series only converges in alternating groups so that examination of the first few terms is not a sufficient test of convergence.

When the series (A4) diverges it is necessary to evaluate Eq. A1 exactly. In the case of potential averaged O-H_2 ($m_2/m_1 \simeq 8$) it is desirable since convergence is slow. This is conveniently achieved by setting $y = r/r$ which transforms (A1) to the interval [0,1] in y, and using an 8-point Gauss-Tchebyshev quadrature[39] or alternatively Gauss-Mehler quadrature[40] to remove the square root singularity. In some cases we have used the more rapidly convergent form of Eq. A1[3]

$$\chi = -b \int_{r_o}^{\infty} \frac{r}{(E_T - V)} \frac{dV}{dr} \left[1 - \frac{V}{E_T} - \frac{b^2}{r^2}\right]^{-\frac{1}{2}} \frac{dr}{r^2} \quad (A16)$$

We require the value of b given χ, but the Newton-Raphson method is no longer useful. Instead we set up a table of log χ versus b for a given ratio A/E_r and obtain b by inverse interpolation, 20 or perhaps 40 points being adequate in most cases.

We may reduce the two parameter search to one by introducing reduced variables. For the exponential form we have

$$\begin{aligned} \rho &= \alpha r \\ \beta &= \alpha b \\ \sigma &= \alpha^2 Q \end{aligned} \tag{A17}$$

and $V(\rho) = Ae^{-\rho}$.* The dependence on α of Eqs. A1 and A15 is thus eliminated giving

$$\chi = \pi - 2\beta \int_{\rho_o}^{\infty} \left[1 - \frac{A}{E_r} e^{-\rho} - \frac{\beta^2}{\rho^2}\right]^{-\frac{1}{2}} \frac{d\rho}{\rho^2} \tag{A18}$$

$$\text{or} \quad \chi = \beta \int_{\rho_o}^{\infty} \frac{A}{E_r} e^{-\rho} \left(1 - \frac{A}{E_r} e^{-\rho}\right)^{-1} \left[1 - \frac{A}{E_r} e^{-\rho} - \frac{\beta^2}{\rho^2}\right]^{-\frac{1}{2}} \frac{d\rho}{\rho}$$

In practice we therefore choose a value of A and for each energy calculate the scattering path volume average $\bar{\sigma}^{calc}(E_r)$ of the single ray reduced cross sections $\sigma^{calc}(E_r) = \pi[\beta(\chi_m)]^2$. The reduced impact parameter is evaluated by inverse interpolation of log χ versus β from (A18). α is then given by the least-squares condition

---

* The exponential potential may be unrealistic for small molecules at very short range (e.g. H-He) so we have followed Jordan and Amdur in matching the exponential to a screened Coulomb potential at small ρ (< 0.6).

$$\alpha(A) = \left\{ \frac{\sum_{\ell} \bar{\sigma}_{\ell}^{\text{calc}} \bar{\sigma}_{\ell}^{\text{calc}}}{\sum_{\ell} \bar{Q}_{\ell}^{\text{exp}} \bar{\sigma}_{\ell}^{\text{calc}}} \right\}^{\frac{1}{2}} \tag{A19}$$

where the suffix ℓ denotes summation over all energies. A is adjusted to minimize the sum of squares of deviations χ^2 (not to be confused with the c.m. scattering angle) between experimental and calculated cross sections. Once three trials of A have been executed, a rapid convergence is obtained by assuming (A_i, χ_i^2) satisfy a quadratic in A, the minimum giving a new prediction of A.

This technique is equally applicable to the momentum approximation, but due to the increased efficiency the latter offers no advantages over an exact evaluation of Eq. A1 even when $m_1 \leq m_2$ and the convergence of Eq. A4 is good. A program written in Fortran IV performs the exact calculation in 0.080 pq secs. of IBM 370/65 central processor time, where p and q are respectively the number of energies and interpolation points. Thus the complete determination of a potential requires typically 30 seconds of computation.

Applying this method to He-Xe gives indistinguishable results from the 1st order momentum approximation (Fig. 14). However, for Xe-He there is a marked improvement in the exact result. The agreement with the He-Xe result of Amdur and Engler[43] and the TFD calculation of Abrahmson[14] is also good. In the cases of O-H_2 and O-He, the changes are significant but less dramatic.

APPENDIX B

Cross Section Averaging

We assume that the intermolecular potential may be represented by the sum of the interatomic teams given in exponential form $V = A\exp(-\rho_i)$ (see Fig. 15), thus

$$V(\rho,\psi) = A(e^{-\rho_1} + e^{-\rho_2}) \tag{B1}$$

where

$$\left.\begin{aligned} \rho_1 &= (\rho^2 + \delta^2 - 2\rho\delta\cos\psi)^{1/2} \\ \rho_2 &= (\rho^2 + \delta^2 + 2\rho\delta\cos\psi)^{1/2} \end{aligned}\right\} \tag{B2}$$

For a given energy and orientation of ψ we may substitute $V(\rho,\psi)$ into Eq. A17 and proceed as before to calculate the volume average $\bar{\sigma}^{calc}(\psi)$. Averaging over orientations we then obtain

$$\bar{\bar{\sigma}}^{calc} = \int_0^1 \bar{\sigma}^{calc}(\psi)\,d(\cos\psi). \tag{B3}$$

Here we use Gauss-Legendre quadrature giving an 8-fold increase in computation time over the atom-atom case. Since Eqs. B2 require the reduced rather than the actual known bond length we cannot eliminate the interatomic potential parameter α as before. However, given a trial value α_i we may obtain a new estimate using the condition (A19), namely

$$\alpha_{i+1} = \left\{ \frac{\sum_{\ell} \bar{\bar{\sigma}}^{calc}_{\ell}(\alpha_i)\,\bar{\bar{\sigma}}^{calc}_{\ell}(\alpha_i)}{\sum_{\ell} \bar{Q}_{\ell}\,\bar{\bar{\sigma}}^{exp\,calc}_{\ell}(\alpha_i)} \right\}^{1/2} \tag{B4}$$

One or occasionally two iterations are usually sufficient to give 4 sig. figs. in α, so that the problem is effectively reduced to a one-parameter search for A. Preliminary guesses at A and α may, if desired, be obtained from the PA method (see main text). Typically 4 mins. are required for an IBM 370/65 computer to calculate the optimum A and α in these experiments. The atom-molecule potential is given by a spherical average of the summed interatomic contributions:

$$\overline{V(R)} = 2Ae^{-\alpha R}(\alpha^2 Rd)^{-1}[2(\alpha R+1)\sinh(\alpha d/2)-\alpha d\cosh(\alpha d/2)]. \qquad (B5)$$

For the systems studied here, $\overline{V(R)}$ may be closely represented by an exponential form $\overline{V(R)} = \bar{A}\exp(-\bar{\alpha}R)$. The range of validity is taken to be the same as that given in the straightforward potential averaging analysis.

References

(1) R. Marriott, Proc. Phys. Soc. 83, 159 (1964)
" " " " 84, 877 (1964)
" " " " 86, 1041 (1965)
" " " " 88, 83 (1966)
" " " " 88, 617 (1966)
R. Marriott and E.S. Gianturco, J. Phys. B2, 1332 (1969).

(2) R.N. Schwartz, Z.I. Slawsky and K.F. Herzfeld, J. Chem Phys. 20, 10 (1951).

(3) P.B. Foreman, P.K. Rol and K.P. Coffin, J. Chem. Phys., 61, 1653 (1974).

(4) O. Sinanoğlu, J. Chem Phys. 30, 858 (1959).

(5) V.B. Leonas, Usp. Fiz. Nauk 107, 29 (1972) [Sov. Phys. - Uspekhi 15, 266 (1973)].

(6) H.S.W. Massey, E.H.S. Burhop and H.B. Gilbody, Electronic and Ionic Impact Phenomena (Clarendon, Oxford, 1969) 2nd ed., Vol. II, pp. 993-1002.

(7) Yu. N. Belyaev, N.V. Kamyshov and V.B. Leonas, *Abstracts of Papers, VIth Interml. Conf. on the Physics of Electronic and Atomic Collisions* (M.I.T., Cambridge, 1969), p. 525. This work was also described in Ref. (6), Vol. IV, pp. 2360-2362.

(8) B.R. Turner, J.A. Rutherford and D.M.J. Compton, J. Chem. Phys. 48, 1602 (1968).

(9) Ionization potentials and electron affinities taken from *Handbook of Chemistry and Physics*, edited by R.C. Weast, (Chemical Rubber Co., Cleveland, 1974-75) 54th ed.

(10) L.C. Allen, A.M. Lesk and R.M. Erdahl, J. Am. Chem. Soc. 88, 615 (1966).

(11) A.B. Kamnev, V.B. Leonas and V.G. Popov, Prib. Tekh. Éksp. 2, 182 (1966) [Instrum. Exp. Tech. (USSR) 2, 454 (1966)].

(12) Yu. N. Belyaev, Vestn. Mosk. Univ. Ser. II, Khim. 2. 44 (1967) [Moscow Univ. Chem. Bull. 22, 30 (1967)].

(13) Yu. N. Belyaev and V.B. Leonas, Chem. Phys. Lett. 1, 375 (1967).

(14) A.A. Abrahamson, Phys. Rev. 178, 76 (1969).

(15) V.I. Gaydaenko and V.K. Nikulin, Chem. Phys. Lett. 7, 360 (1970).

(16) K. Günther, Ann. Phys. 14 296 (1964); Kernenergie 7, 443 (1964).

(17) V.K. Nikulin, Zh. Tekhn. Fiz. 41, 41 (1971) [Sov. Phys. - Tech. Phys. 16, 28 (1971)].

(18) Unpublished cross section average potentials, assuming additive (inverse power) interatomic interactions, have been calculated from scattering data by
(a) A.B. Marcus, Ph.D. thesis (M.I.T., Cambridge, 1965),
(b) D.E. Paulsen, Ph.D. thesis (M.I.T., Cambridge, 1965),
(c) M.J. Engler, Ph.D. thesis (M.I.T., Cambridge, 1969).

(19) M. Krauss and F.N. Mies, J. Chem. Phys. 42, 2703 (1965); M.D. Gordon and D. Secrest, J. Chem. Phys. 52, 120 (1970).

(20) K.T. Tang and M. Karplus, J. Chem. Phys. 49, 1676 (1968).

(21) I. Amdur, E.A. Mason and J.E. Jordan, J. Chem.Phys. 27, 527 (1957).

(22) J.E. Jordan, S.O. Colgate, I. Amdur and E.A. Mason, J. Chem. Phys. 52, 1143 (1970).

(23) I. Amdur, M.S. Longmire and E.A. Mason, J. Chem. Phys. 35, 895 (1961); E.A. Mason and I. Amdur, J. Chem. Phys. 41, 2695 (1964).

(24) I. Prigogine, A. Bellemans and V. Mathot, *Molecular Theory of Solutions* (North-Holland, Amsterdam, 1957) p. 265 ff.

(25) Yu. N. Belyaev and V.B. Leonas, Zh. Éksp. Teor. Fiz., Pis'ma Red. 4, 134 (1966) [JETP Lett. 4, 92(1966)].

(26) Yu. N. Belyaev , N.V. Kamyshov and V.B. Leonas, Dokl. Akad. Nauk SSSR 180, 1312 (1968) [Sov. Phys. - Dokl. 13, 551 (1968)].

(27) Yu. N. Belyaev , N.V. Kamyshov, V.B. Leonas and A.V. Sermyagin, Entropie 30, 173 (1969).

(28) A.P. Kalinin and V.B. Leonas, Dokl. Akad. Nauk SSSR 197, 393 (1971) [Dokl. - Phys. Chem. 197, 262 (1971)].

(29) A.P. Kalinin, V.B. Leonas and A.V. Sermyagin, Teplofiz. Vys. Temp. 9, 1066 (1971) [High. Temp. 9, 971 (1971)].

(30) K.S. Yun and E.A. Mason, Phys. Fluids 5, 380 (1962).

(31) J.T. Vanderslice, E.A. Mason and W.G. Maisch, J. Chem. Phys. 31, 738 (1959).

(32) W.E. Meador, Jr., NASA Tech. Rep. R-68 (1960).

(33) A.P. Kalinin and V.B. Leonas, Dokl. Akad. Nauk SSSR 201, 53 (1971) [Sov. Phys. - Dokl. 16, 959 (1972)].

(34) J.E. Jordan and I. Amdur, J. Chem. Phys. 46, 165 (1967).

(35) C. Lehmann and G. Leibfried, Z. Phys. 172, 465 (1963).

(36) F.T. Smith, R.P. Marchi and K.G. Dedrick, Phys. Rev. 150, 79 (1966).

(37) G. Leibfried and T. Plesser, Z. Phys. 187, 421 (1965).

(38) I. Amdur, E.A. Mason and A.L. Harkness, J. Chem. Phys. 22, 1071 (1954); S.O. Colgate, J.E. Jordan, I. Amdur and E.A. Mason, J. Chem. Phys. 51, 968 (1969),

(39) F.B. Hildebrand, *Introduction to Numerical Analysis* (McGraw Hill, New York, 1974) 2nd ed., p. 398.

(40) F.J. Smith, Physica 30, 497 (1964).

(41) R.S. Berry, Chem Rev. 69, 533 (1969), and references cited therein

(42) A.B. Kamnev and V.B. Leonas, Teplofiz. Vys. Temp. 4, 288 (1966) [High Temp. 4, 283 (1966)].

(43) I. Amdur and M.J. Engler, unpublished preprint (1970).

Table I. Potential parameters for interaction of $O(^3P)$ with noble gases. $V(r) = A \exp(-\alpha r)$

Target	A(eV)	($Å^{-1}$)	Range (Å)
He	378	3.744	0.85 - 1.81
Ne	1222	3.917	1.16 - 2.05
Ar	791	3.217	1.25 - 2.36
Kr	1063	3.249	1.35 - 2.43
Xe	1432	3.287	1.43 - 2.50

Table II. Dependence of incomplete integral cross sections (including end correction) on lab. energy for collisions of $O(^3P)$ with atmospheric molecules.

Energy(eV)	Cross section (Å2)						
	H_2	N_2	O_2	NO	CO	CO_2	H_2O
2500	2.25	4.76	5.54	5.34	4.98	7.49	5.01
2000	2.56	5.28	6.23	5.89	5.48	8.31	5.50
1500	2.99	5.98	7.06	6.62	6.12	9.26	6.14
1000	3.65	7.20	8.38	7.94	7.46	11.05	7.40
700	4.56	8.51	9.68	9.37	8.76	12.85	8.74
500	4.97	9.92	10.87	10.43	9.96	14.47	9.67
400	5.49	10.94	11.54	11.31	10.89	15.43	10.41
300	6.21	12.35	12.70	12.52	12.13	16.74	11.28
200	7.22	14.29	14.13	14.41	13.58	18.32	12.71
150	8.11	15.74	15.04	15.50	14.94	19.43	13.78
100	9.60	17.62	16.25	16.98	16.77	20.97	15.02

Table III. Potential averaged (PA) parameters for interaction of $O(^3P)$ with atmospheric molecules. (The latter assumed to have spherical symmetry). $V(R) = A \exp(-\alpha R)$

Target	A(ev)	$\alpha(Å^{-1})$	Range (Å)
H_2	422	3.912	0.84 - 1.76
N_2	541	3.012	1.20 - 2.38
O_2	1870	3.670	1.36 - 2.31
NO	1048	3.350	1.30 - 2.35
CO	825	3.286	1.24 - 2.32
CO_2	2347	3.317	1.59 - 2.63
H_2O	1484	3.724	1.28 - 2.21

Table IV. Cross section averaged (CSA) parameters for *interatomic* potentials $V(r) = A \exp(-\alpha r)$ in collisions of $O(^3P)$ with homonuclear diatomics. Additive forces assumed.

Target	Interaction	A(eV)	$\alpha(Å^{-1})$	Range (Å)
H_2	O....H	209	4.030	0.90 - 1.78
N_2	O....N	316	3.221	1.28 - 2.42
O_2	O....O	905	3.856	1.45 - 2.37

Table V. CSA parameters for interaction $\overline{V(R)} = \bar{A}\exp(-\bar{\alpha}R)$ of $O(^3P)$ with diatomic molecules. Parameters obtained by averaging over all orientations the interatomic potentials in Table IV. Additive forces assumed.

Target	$\bar{A}$ (eV)	$\bar{\alpha}$ (Å^{-1})	Range (Å)
H_2	444	3.916	0.84 - 1.76
N_2	698	3.109	1.20 - 2.38
O_2	2438	3.715	1.36 - 2.31
NO(a)	972	3.326	1.45 - 2.44

(a) Note that this potential is not derived from O-NO experimental data, but rather from O-O_2 and O-N_2.

Table VI. *Interatomic* PA parameters for $V(r) = A\exp(-\alpha r)$, derived from $O(^3P)$ - homonuclear diatomic potentials in Table III. Additive forces assumed.

Target	Interaction	A(eV)	α(Å^{-1})	Range (Å)
H_2	O....H	202	4.037	0.90 - 1.78
N_2	O....N	249	3.121	1.28 - 2.42
O_2	O....O	703	3.810	1.45 - 2.37

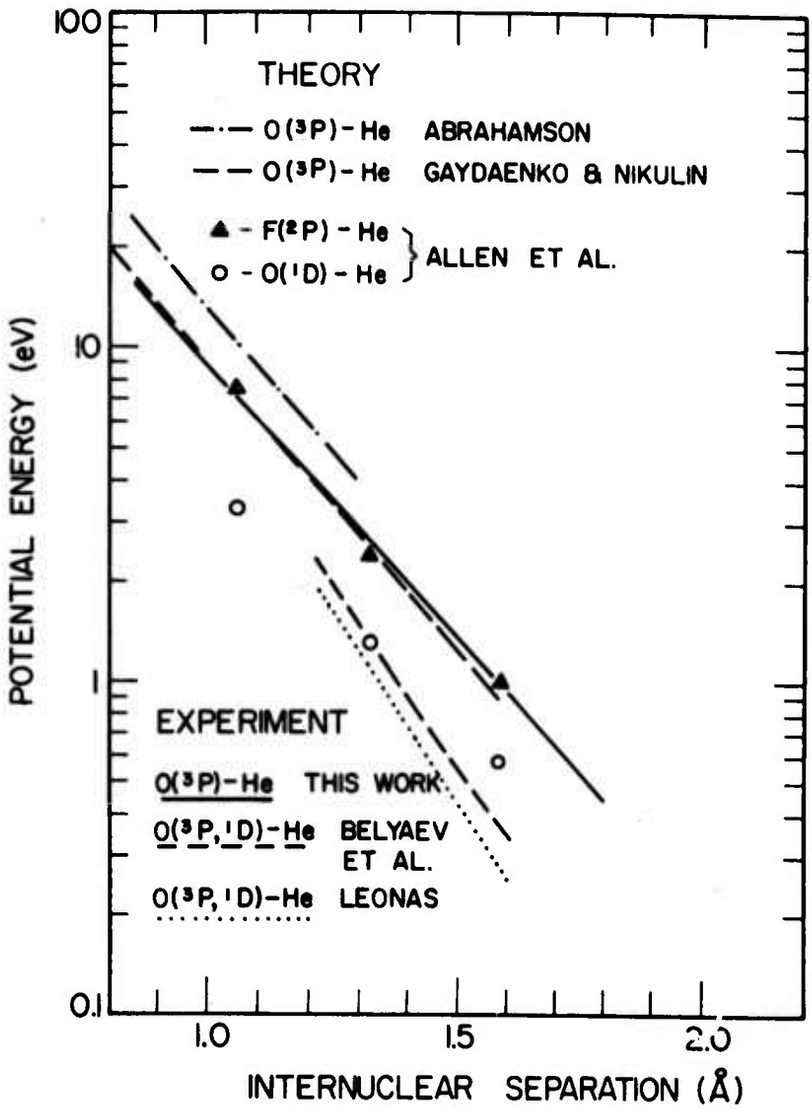

1. Comparison of theoretical[10,14,15] and experimental[5,7] potentials for O-He. The charge transfer reactants were $O^+ + Kr$ in the case of Belyaev et al. and also Leonas. This work is an average of $O^+ + Xe$ and $O^- + O_2$.

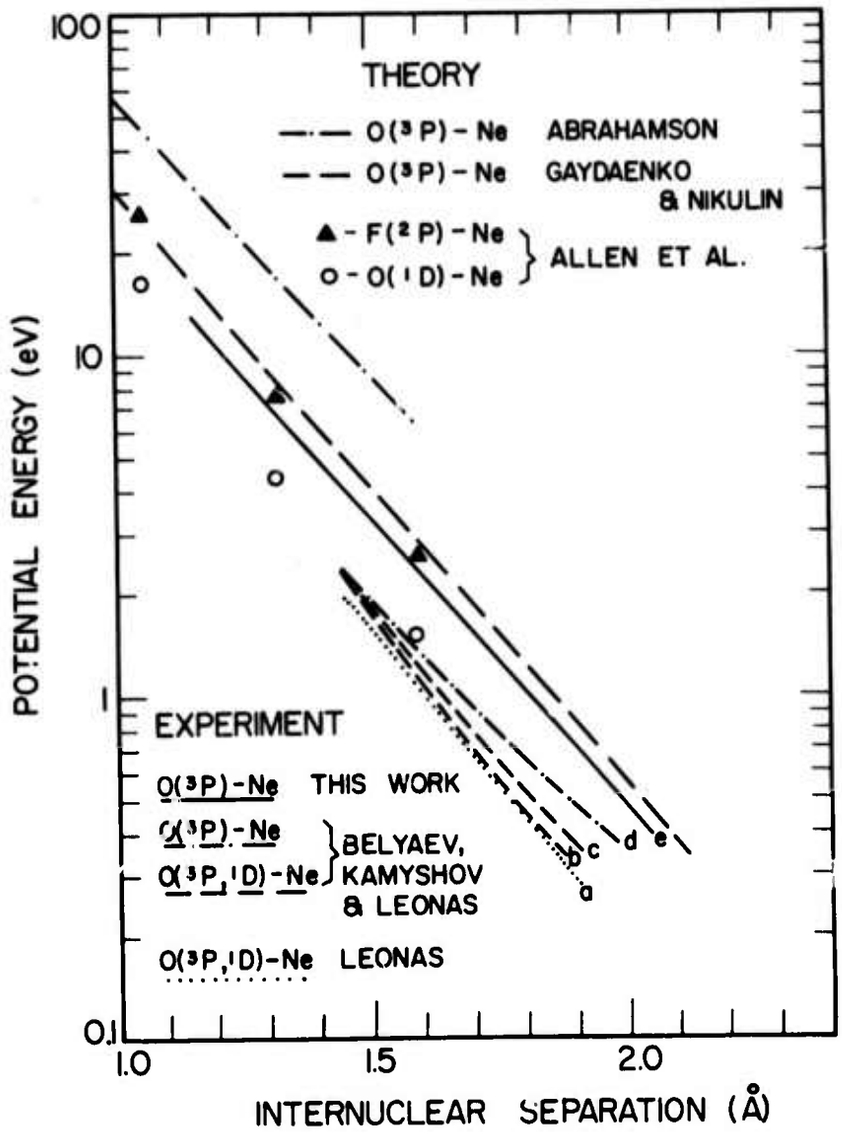

2. Comparison of theoretical[10,14,15] and experimental[5,7] potentials for O-Ne. Charge transfer reactants used: (a) $O^+ + Kr$, (b) $O^+ + Xe$, (C) $O^+ + Kr$, (d) $O^- + O_2$, CO_2, (e) average of $O^- + O_2$, $O^+ + Kr$ and $O^+ + Xe$.

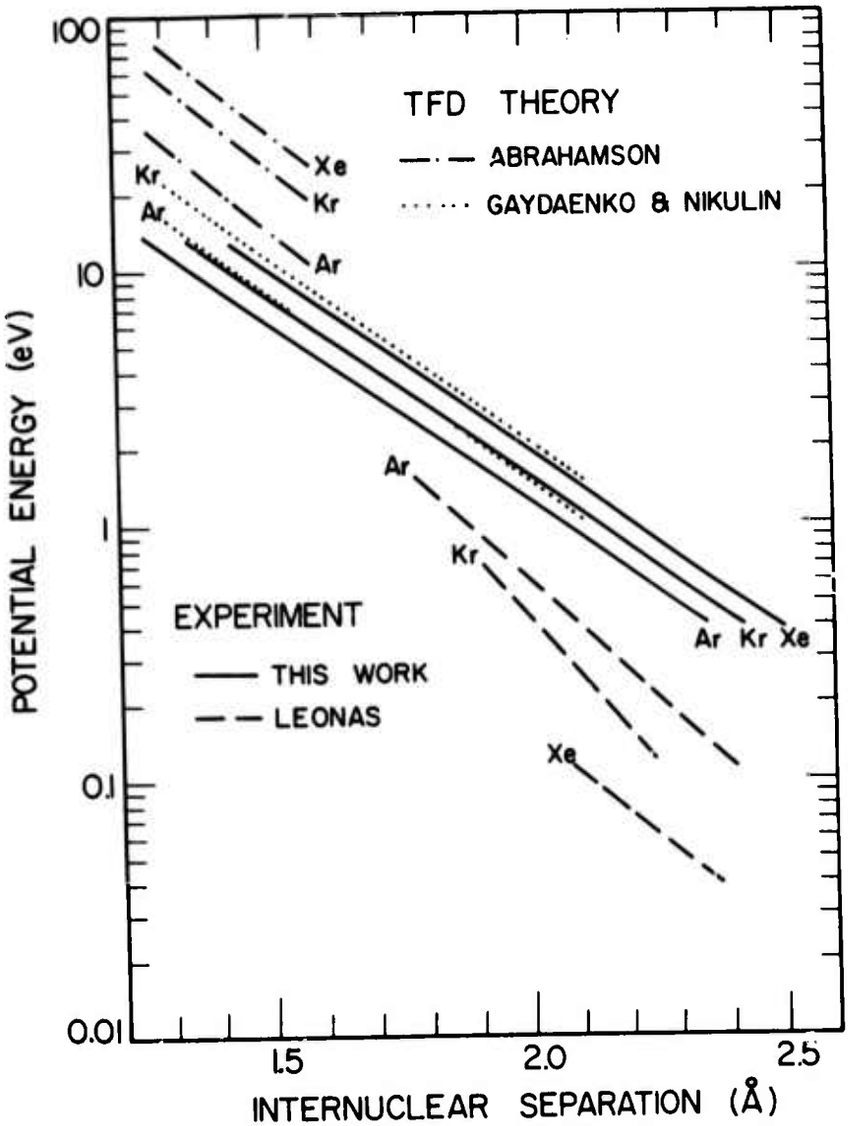

3. Comparison of experimental[5] potentials for O-Ar, Kr, Xe with calculations in the Thomas-Fermi-Dirac approx.[14,15] The earlier results of Belyaev et al.[12,13] are omitted to avoid confusion; they lie between this work and the results of Leonas.

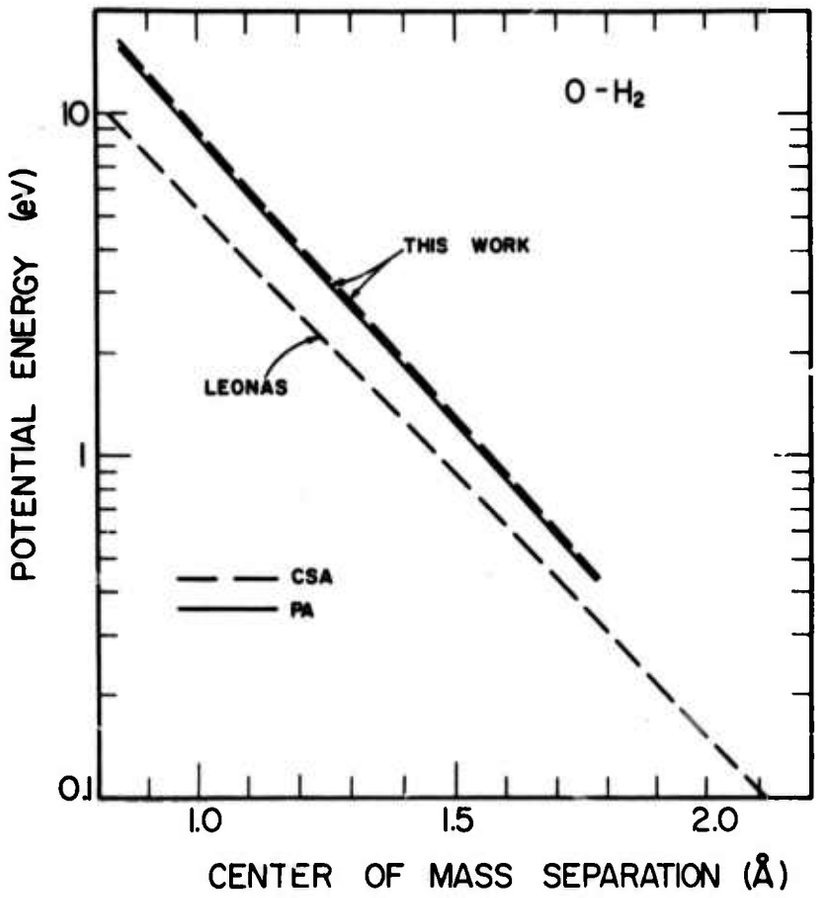

4. Comparison of experimental potentials for O-H_2 treated in the potential average (PA) and cross section average (CSA) approx.

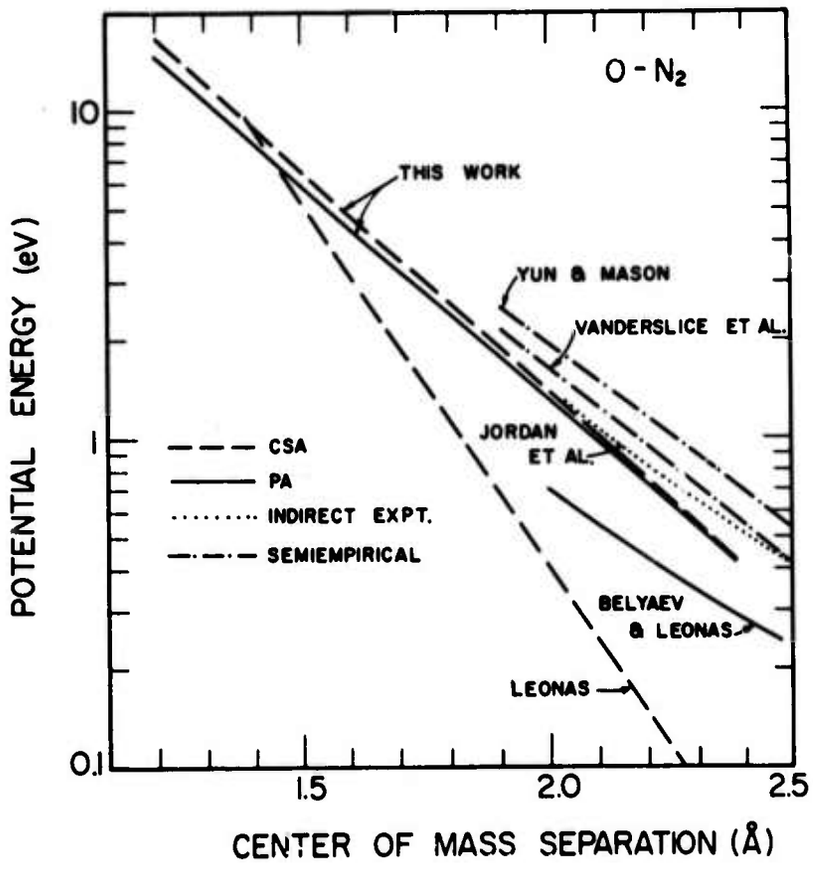

5. Exptl. PA and CSA potentials for $O\text{-}N_2$[5,25] compared with semiempirical calculations[30,31] and an indirect result[22] derived from $Ar\text{-}O_2$, $Ar\text{-}N_2$ and Ar-Ar assuming additive interatomic forces and the geometric mean (GM) combination rule.

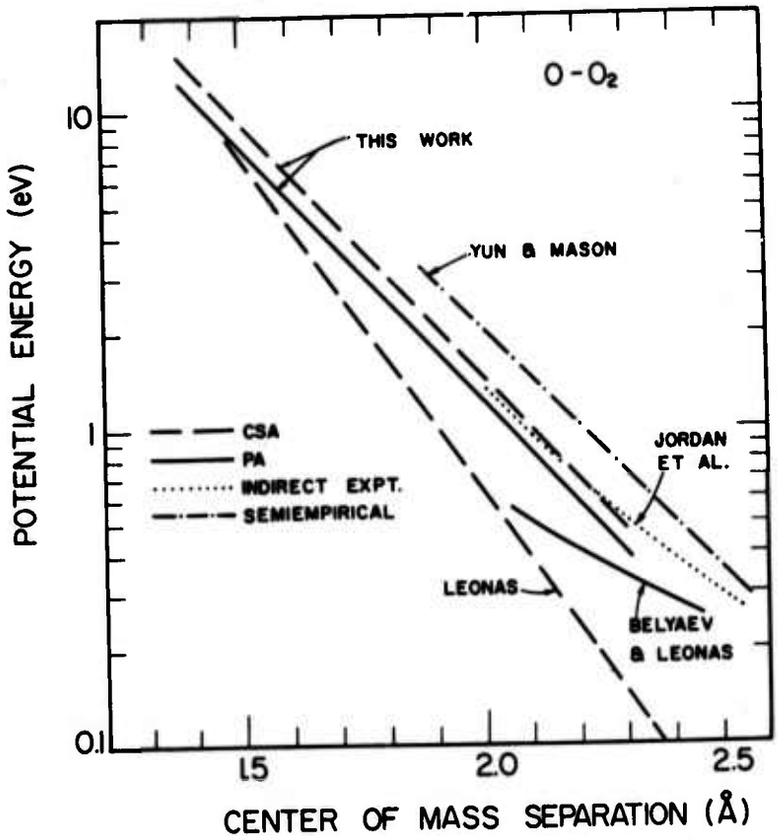

6. Exptl. PA and CSA potentials for $O\text{-}O_2$[5,25] compared with semiempirical calcns.[30] and an indirect result derived from $Ar\text{-}O_2$ and Ar-Ar.[22]

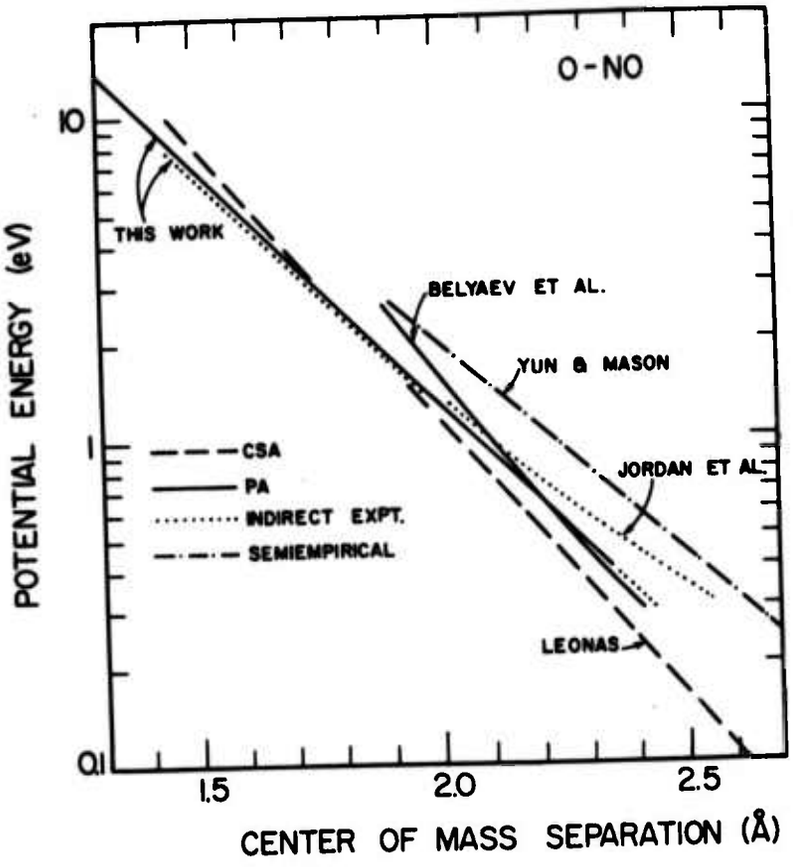

7. O-NO potentials from PA and CSA treatments[5,26] compared with semiempirical theory.[30] The indirect potential in this work was obtained from the CSA $O-O_2$ and $O-N_2$ interactions assuming additive interatomic forces. The derived potential of Jordan et al.[22] additionally assumes the GM rule.

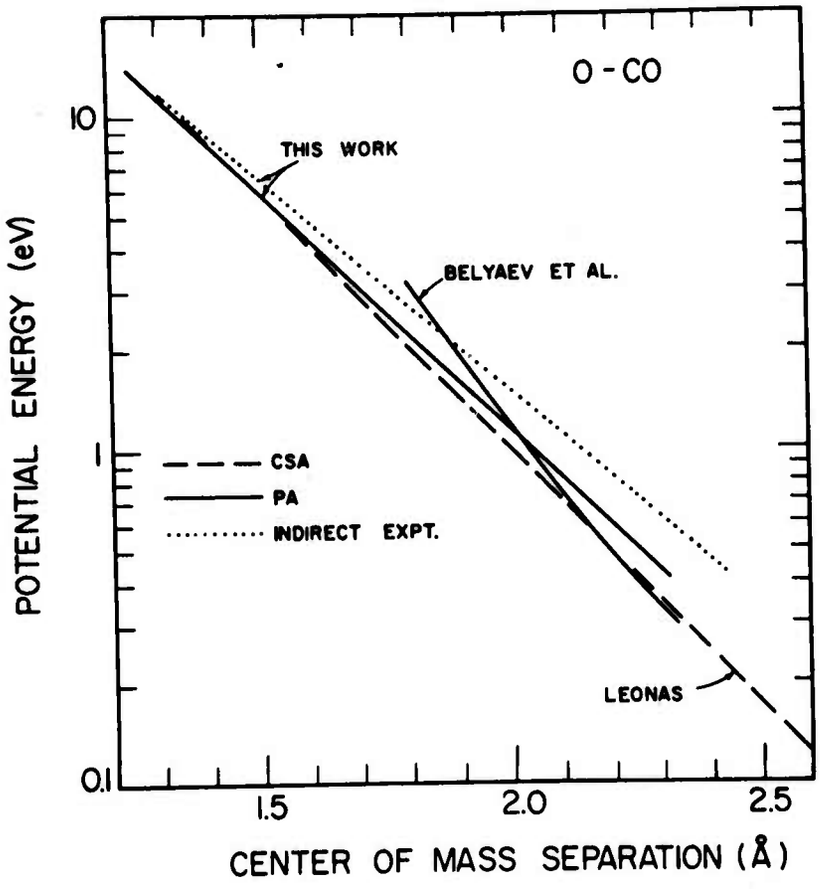

8. Comparison of direct PA and CSA exptl. results[5,26] for O-CO together with an indirect result from combination of Ar-CO, Ar-Ar and O-Ar assuming that CO is spherically symmetric.

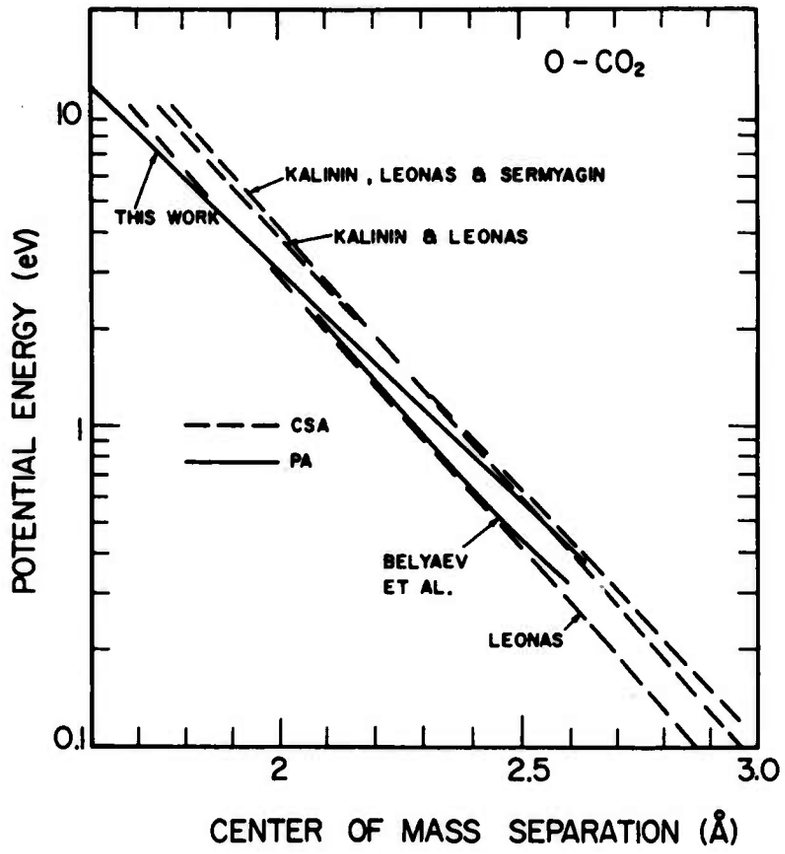

9. Exptl. PA and CSA results for $O\text{-}CO_2$.[5,27-29]

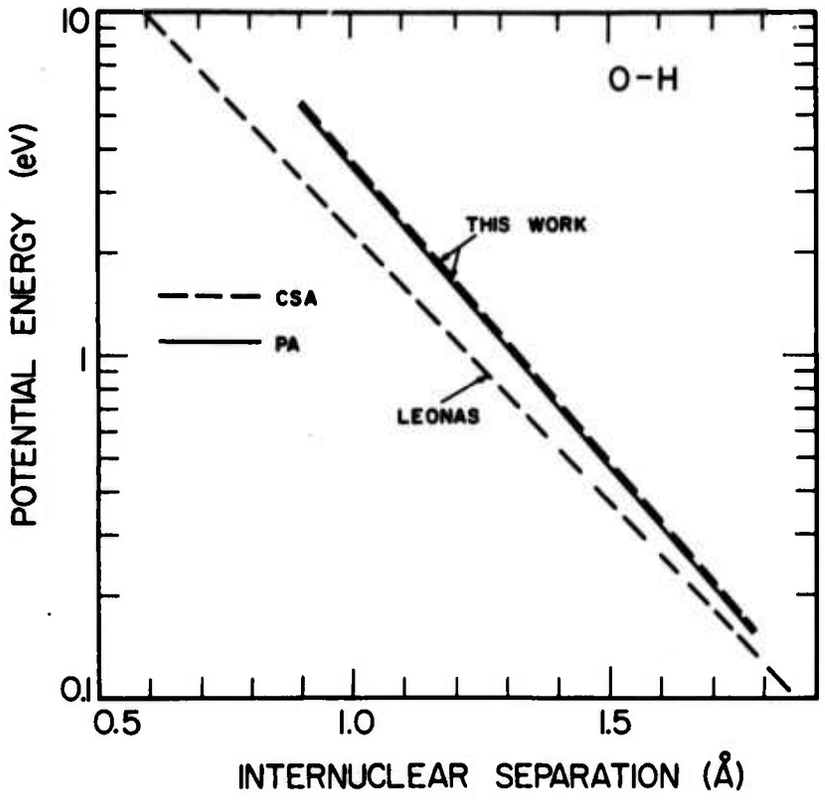

10. "Interatomic" O-H potential obtained by PA and CSA methods.[5]

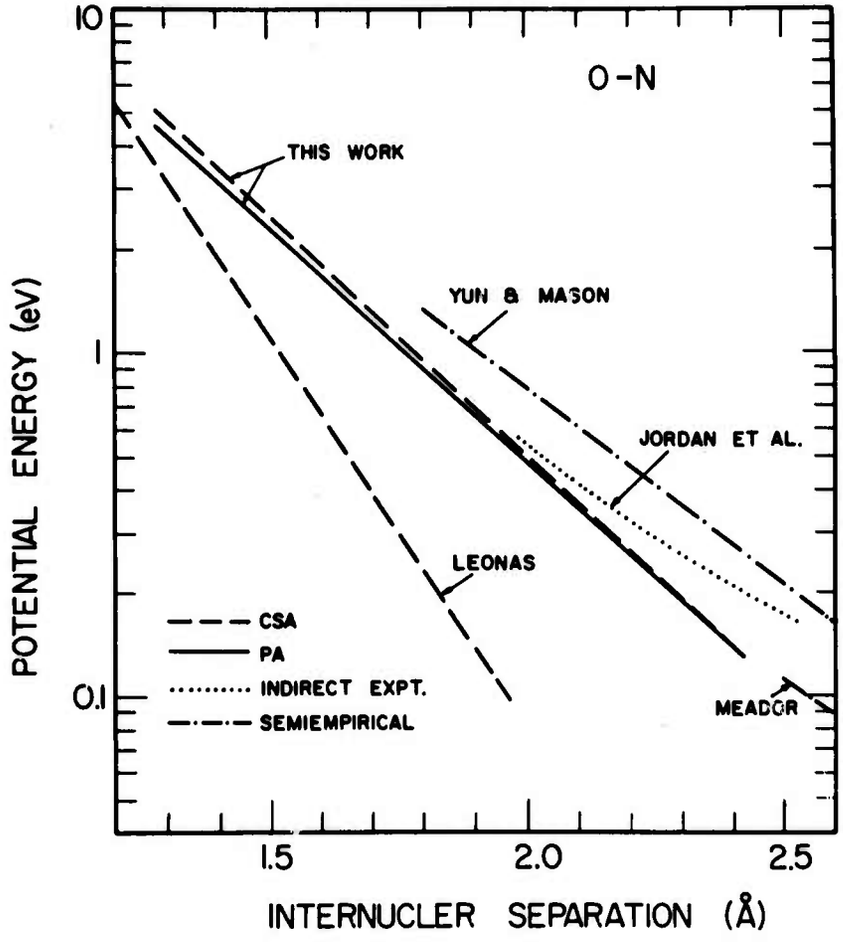

11. Exptl. "interatomic" O-N potentials[5] compared with semiempirical calcns.[30,32] The indirect expt.[22] assumes the GM rule.

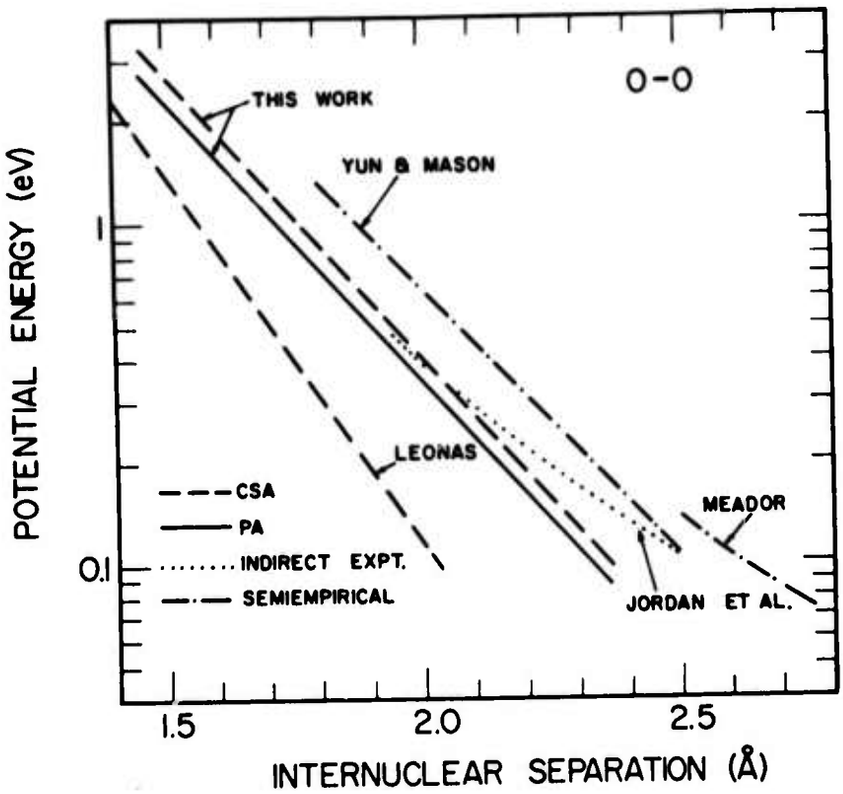

12. Exptl. "interatomic" O-O potentials[5] and semiempirical calcns.[30,32] The indirect expt. assumes the GM rule.

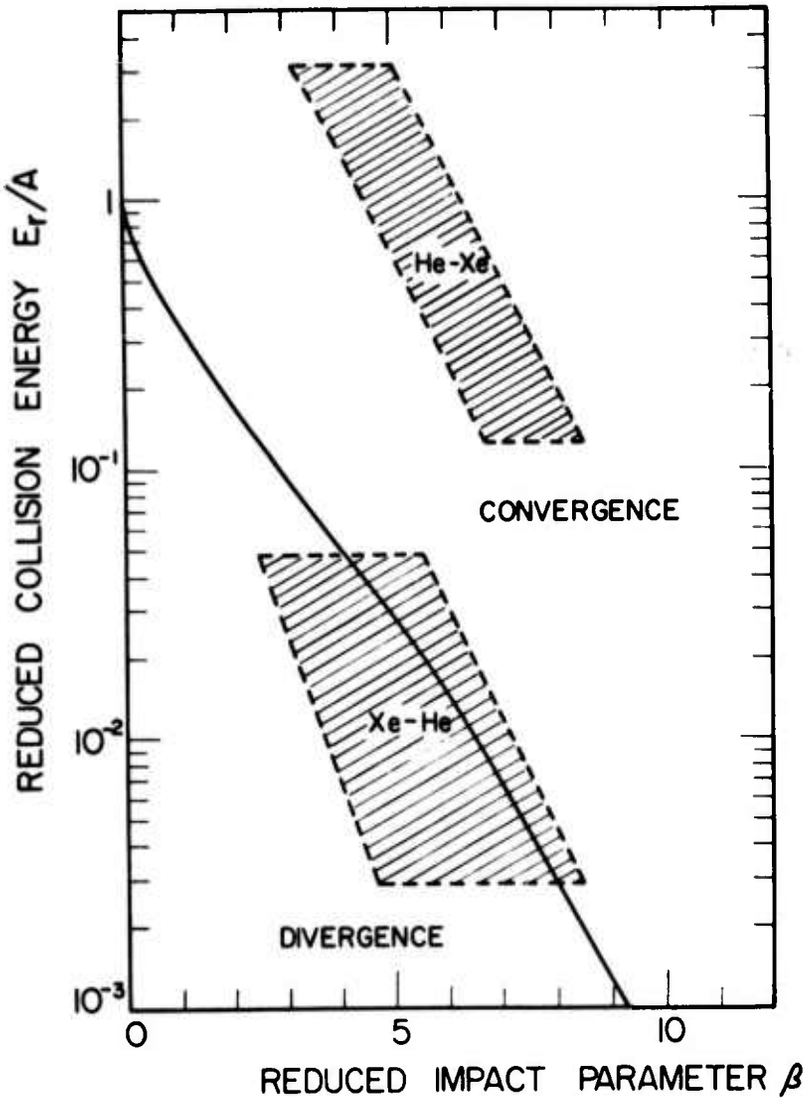

13. Area of convergence of the momentum approx. for $V(r) = A \exp(-\alpha r)$. The hatched areas are the regions sampled by the present exptl. geometry ($\Theta = 5.55 \times 10^{-3} - 2.87 \times 10^{-2}$ rad.). The potential parameters, determined from Eq.A17, are A = 777eV, $\alpha = 3.137 \text{Å}^{-1}$, E = 100-2500eV for He-Xe, and A = 1546eV, $\alpha = 3.506 \text{Å}^{-1}$, E = 150-2500eV for Xe-He.

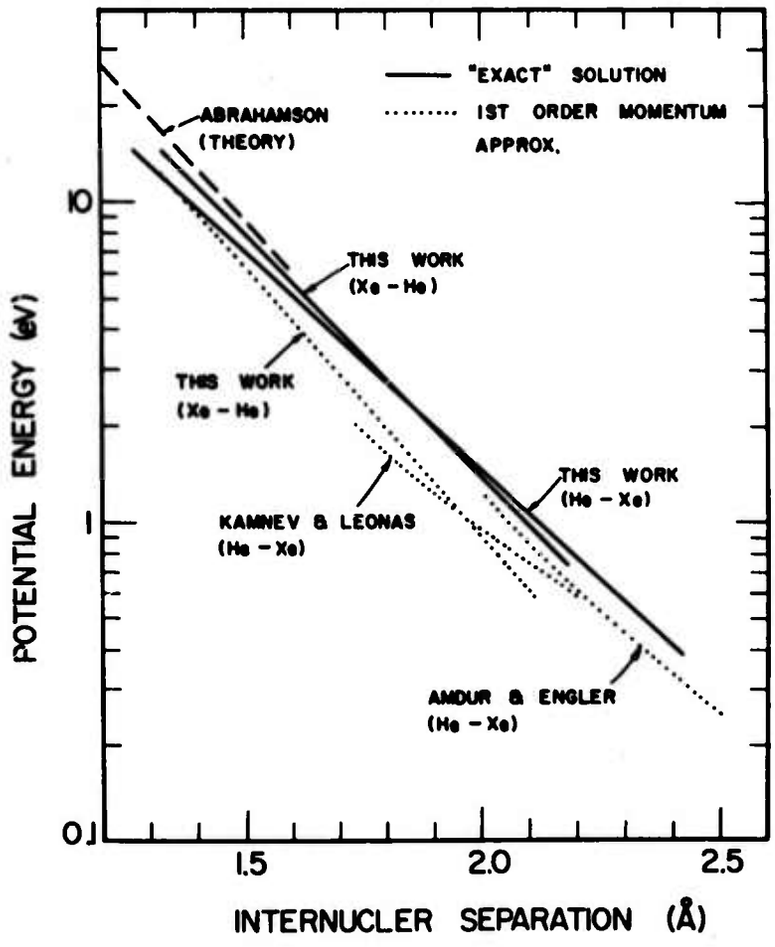

14. Exptl.[42,43] and theoretical[14] results for the He-Xe, Xe-He potential.

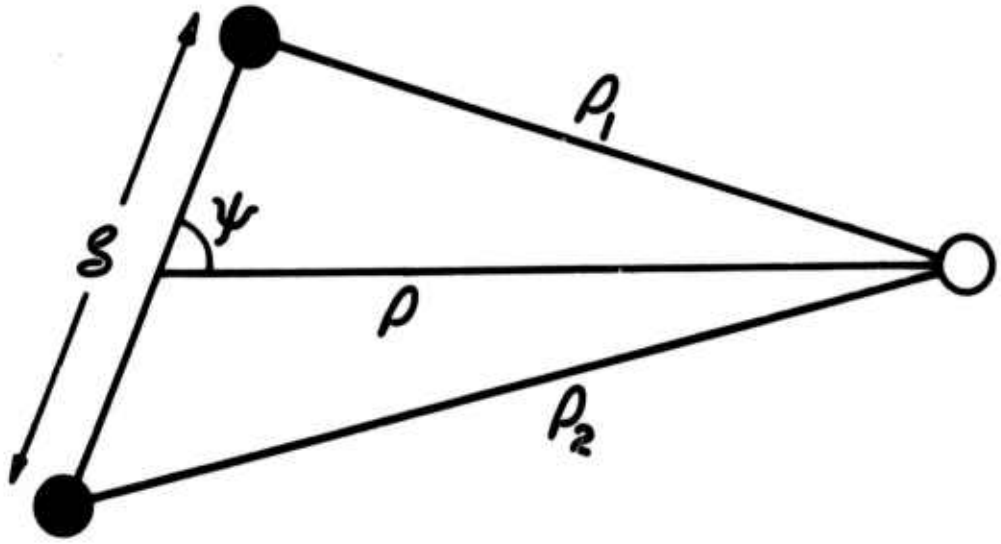

15. Reduced coordinates defining the interaction of an atom with a homonuclear diatomic molecule whose equilibrium bond length is δ/α. The center of mass and internuclear separations are respectively $R = \rho/\alpha$ and $r_i = \rho_i / \alpha$.